

PROBING ELECTRONIC AND THERMOELECTRIC PROPERTIES OF SINGLE MOLECULE JUNCTIONS

JONATHAN R. WIDAWSKY

Submitted in partial fulfillment of the
requirements for the degree of
Doctor of Philosophy
in the Graduate School of Arts and Sciences

COLUMBIA UNIVERSITY

2013

© 2013
Jonathan Widawsky
All rights reserved

ABSTRACT

Probing Electronic and Thermoelectric Properties of Single Molecule Junctions

Jonathan R. Widawsky

In an effort to further understand electronic and thermoelectric phenomenon at the nanometer scale, we have studied the transport properties of single molecule junctions. To carry out these transport measurements, we use the scanning tunneling microscope-break junction (STM-BJ) technique, which involves the repeated formation and breakage of a metal point contact in an environment of the target molecule. Using this technique, we are able to create gaps that can trap the molecules, allowing us to sequentially and reproducibly create a large number of junctions. By applying a small bias across the junction, we can measure its conductance and learn about the transport mechanisms at the nanoscale. The experimental work presented here directly probes the transmission properties of single molecules through the systematic measurement of junction conductance (at low and high bias) and thermopower.

We present measurements on a variety of molecular families and study how conductance depends on the character of the linkage (metal-molecule bond) and the nature of the molecular backbone. We start by describing a novel way to construct single molecule junctions by covalently connecting the molecular backbone to the electrodes. This eliminates the use of linking substituents, and as a result, the junction conductance increases substantially. Then, we compare transport across silicon chains (silanes) and saturated carbon chains (alkanes) while keeping the linkers the same and find a stark difference in their electronic transport properties.

We extend our studies of molecular junctions by looking at two additional aspects of quantum transport – molecular thermopower and molecular current-voltage characteristics. Each

of these additional parameters gives us further insight into transport properties at the nanoscale. Evaluating the junction thermopower allows us to determine the nature of charge carriers in the system and we demonstrate this by contrasting the measurement of amine-terminated and pyridine-terminated molecules (which exhibit hole transport and electron transport, respectively). We also report the thermopower of the highly conducting, covalently bound molecular junctions that we have recently been able to form, and learn that, because of their unique transport properties, the junction power factors, GS^2 , are extremely high. Finally, we discuss the measurement of molecular current-voltage curves and consider the electronic and physical effects of applying a large bias to the system. We conclude with a summary of the work discussed and an outlook on related scientific studies.

Table of Contents

Table of Contents.....	i
List of Figures	iii
List of Tables	xvii
Acknowledgement	xviii
Dedication	xx
Chapter 1: Introduction	1
Section 1.1: Motivation – Single Molecule Junctions	2
Section 1.2: Outline	5
Section 1.3: References.....	8
Chapter 2: Experimental Framework.....	11
Section 2.1: Scanning Tunneling Microscope Setup	12
2.1A: Description of the Home-Built System and Measurement	13
2.1B: Modifications for Thermal Setup	16
Section 2.2: Conductance Traces, Conductance Histograms, and Statistical Analysis	18
2.2A: Collection of Conductance Traces	18
2.2B: Construction of Conductance Histograms	19
Section 2.3: Understanding Molecular Conductance with a Single Level Model	21
Section 2.4: References.....	26
Chapter 3: The Development of Highly Conducting Junctions.....	28
Section 3.1: <i>In situ</i> Formation of Highly Conducting Covalent Au–C Contacts for Single-Molecule Junctions	30
Section 3.2: Highly Conducting π -Conjugated Molecular Junctions Covalently Bonded to Gold Electrodes.....	42

Section 3.3: Conductive Molecular Silicon	53
Section 3.4: References.....	62
Chapter 4: Concurrent Conductance and Thermopower Measurements	70
Section 4.1: Simultaneous Determination of Conductance and Thermopower of Single Molecule Junctions	72
Section 4.2: Length-Dependent Thermopower of Highly Conducting Au-C Bonded Single Molecule Junctions	85
Section 4.3: References.....	99
Chapter 5: Measurement of Molecular I-V Characteristics.....	104
Section 5.1: Measurement of Voltage Dependent Electronic Transport Across Amine-Linked Single Molecular Wire Junctions	106
Section 5.2: References.....	119
Chapter 6: Conclusions	121
Section 6.1: Summary and Scientific Impact.....	122
Section 6.2: Outlook	124
Section 6.3: Complete List of Published Work	126
Appendix.....	127
Section A.1: Supplementary Information for Section 3.1.....	128
Section A.2: Supplementary Information for Section 3.2.....	132
Section A.3: Supplementary Information for Section 3.3.....	134
Section A.4: Supplementary Information for Section 4.1.....	139
Section A.5: Supplementary Information for Section 4.2.....	144
Section A.6: References.....	153

List of Figures

Figure 1.1 3

Illustration of a single molecule junction. The linker groups have separated from the molecule and as a result, the molecular backbone is directly attached to the gold electrodes.

Figure 2.1 13

(a) Picture of the basic home-built modified scanning tunneling microscope (STM). The commercially acquired piezo actuator gives the system z-axis mobility with sub-angstrom position resolution. Zoom in: Picture of a gold tip cut on an angle to taper above a gold-on-mica substrate. The reflection of the tip is observable in the substrate as well. (b) Schematic of the STM-BJ setup circuit, which includes a series resistor, R_s .

Figure 2.2 15

Example I-V trace measured during a voltage sweep for a typical molecular junction. The piezo displacement (gray line), shown in the upper panel, includes a momentary hold section to freeze the junction during elongation event. The measured current (red, left axis) and voltage (blue, right axis) are shown in the bottom panel. Note that the voltage is very low when the junction conductance is low due to the series resistor.

Figure 2.3 16

(a) Top: Schematic of the STM-BJ setup modified to perform thermal measurements. Bottom: Simplified diagram illustrating measurement of thermoelectric current (I_T) when a temperature gradient is imposed. (b) Top: Piezo ramp used, including a “hold” portion between 150 and 200 ms. Middle: External applied voltage across the leads which drops to zero during the center of the “hold” portion. Bottom: Sample trace for an example

molecular junction. The measured current is shown in red and the voltage measured across the junction is shown in blue. Note: The voltage is applied across the junction in series with a $10\text{ k}\Omega$ resistor.

Figure 2.4 19

(a) Sample conductance traces for clean gold (yellow) and in the presence of 1,4-Diaminobutane (blue) measured at 25 mV. The conductance traces exhibit steps at integer multiples of G_0 . The blue traces also show a molecule-dependent plateau below $1 G_0$ due to the formation of a molecular junction. (b) Conductance histograms for clean gold (solid yellow) and for 1,4-Diaminobutane (blue). The blue histogram exhibits a peak (arrow) above the tunneling background that can be fit to determine the most frequently measured conductance.

Figure 2.5 20

(a) Histogram for C4A constructed using a logarithmic binning of 100/decade. (b) Two-dimensional conductance histogram for C4A composed of 10,000 conductance traces measured at 25 mV. Bin sizes of 0.008 nm along the displacement axis and 100/decade along the conductance axis are used. The molecular step at $10^{-3} G_0$ extends to a length 0.3 nm from the rupture of the gold point contact. Clear steps at integer multiple values of G_0 are also evident, as well as the experimental background at $10^{-5} G_0$.

Figure 2.6 22

(a) Energy level diagram describing the formation of molecular hydrogen. The two original 1s atomic orbitals hybridize to form an occupied bonding state and unoccupied antibonding state. (b) Energy level diagram of a ‘single-level’ molecule bound to metallic electrodes with coupling Γ . A picture of a junction with C4A is given as well.

Figure 2.7 23

(a) Example of a single Lorentzian transmission function. The conductance of the junction is equal to the value of the transmission function at the Fermi energy in units of G_0 , the quantum of conductance. (b) Example of a double Lorentzian transmission function, with the Fermi energy shown between the highest occupied and lowest unoccupied molecular orbitals.

Figure 3.1 32

(a) Junction formation and conductance measurements with 1,4-bis(trimethylstannylyl)butane molecules between gold electrodes. (H atoms, white; C atoms, grey; Sn, green). (b) Sample traces showing conductance (on a logarithmic scale) versus relative displacement for SnMe₃-terminated alkanes with four (**C4**: red), six (**C6**: blue), eight (**C8**: green) and ten (**C10**: yellow) methylene groups in the backbone. (c) Conductance histograms for **C4**, **C6**, **C8**, **C10** and **C12**. Each histogram is constructed from 10,000 traces and is generated without any data selection. Bin size is $10^{-4} G_0$ for **C4**, $10^{-5} G_0$ for **C6** and **C8**, $10^{-6} G_0$ for **C10** and $10^{-7} G_0$ for **C12**. Upward arrows indicate primary conductance peaks; downward arrows indicate lower conducting shoulders; asterisks indicate conductance peaks due to the dimer molecule formed *in situ*. (d) Conductance at the peak (as determined by fitting a Lorentzian to the histograms) on a logarithmic scale versus number of methylene groups in the backbone for SnMe₃-terminated alkanes (red) and analogous diamine-terminated alkanes (blue).

Figure 3.2 36

(a) Conductance histograms for two SnMe₃-terminated alkanes (**C6** and **C8**) and two Au-PPh₃-terminated alkanes (**C6Au** and **C8Au**). Bin size is $10^{-5} G_0$. Inset: structures for

SnMe₃-terminated alkanes (bottom) and Au-PPh₃-terminated alkanes (top) with $n = 6$ or 8. (b) Conductance histograms for SnMe₃-terminated benzene (**Ph**) and Au-PPh₃-terminated benzene (**PhAu**). Bin size is $10^{-4}G_0$. Inset: structures for **Ph** (top) and **PhAu** (bottom).

Figure 3.3 38

(a) Sample geometry used to determine the energy required to first cleave a C–SnMe₃ bond and then bond the SnMe₃ to the Au(111) surface and the C₂H₅ to a model electrode structure. (b) Sample geometry used to determine the energy required to first cleave the Sn–CH₃ bond and then bond the CH₃ to the Au(111) surface and the SnMe₂C₂H₅ to a model electrode structure. (c) Sample geometry used in transmission calculations for **C6**. (d) Transmission (on a logarithmic scale) versus energy (relative to the Fermi energy) for **C1** (dashed black line), **C4** (red), **C6** (blue) and **C8** (green) junctions. Inset: molecular scattering state at the Fermi energy showing σ character.

Figure 3.4 44

In situ formation of direct Au–electrode–C bonds starting from SnMe₃ precursors.

Figure 3.5 45

(a) Individual conductance traces measured in solutions of the SnMe₃-terminated polyphenyl compounds **P1–P4**. Measurements in solvent alone are also shown for comparison (Au). The applied bias is 250 mV. (b) Conductance histograms of over 10,000 traces generated with linear bin size of 0.0001 G₀, shown on a log–log scale. Inset: the same data on a linear scale. (c) Conductance versus number of phenylene units in the chain for **P1–P4**, and analogous measurements with the related amine-terminated

series. Dotted lines represent linear least-squares fit to **P2–P4** series. Note the point for **P1** above the line.

Figure 3.6 47

(a) Structures of additional compounds studied. (b) Individual conductance traces measured in solutions of the SnMe₃-terminated compounds **P1** (red) and **2MeP1** (black) at 25 mV applied bias. (c) Conductance histograms of over 10□000 individual measurements, generated with linear bin size of 0.0001 G₀, shown on a log–log scale. Inset: same histograms on a linear scale.

Figure 3.7 50

(a) Calculated transmission spectrum for **P1** bonded to Au electrodes. Inset: isosurface plots of the real part of the transmitted scattering states for energies at the vertical bars (−1.15 and −0.4 eV), showing the even and odd combinations of the Au–C bonds coupled through the π backbone. (b) Transmission spectra for **P1–P4**. Bars indicate the approximate position Au–C MO energies.

Figure 3.8 55

(a) Molecular structures of methyl sulfide-capped oligosilanes **Si1–5** and alkanes **C2–4**. (b) ORTEP of a single molecule of silane **Si2**. Ellipsoids are shown at the 50% probability level. (c) B3LYP/6-31G**-calculated lowest-energy structures of oligosilanes **Si1–5**. (d) Perspective drawing of the lowest-energy conformation of pentasilane **Si5**, demonstrating the flexible silicon backbone. In (b–d), H atoms have been omitted for clarity; S is shown in yellow, Si in blue, and C in green.

Figure 3.9 56

Synthetic scheme for α,ω -Bis(4-methylthio)phenyloligosolanes **Si1-5**: (a) Arylsilylation Reaction; (b) Synthesis of α,ω -Dichlorooligosilanes **5c-e**

Figure 3.10 57

(a) 2D conductance histogram for **Si1** showing a clear conductance peak that extends over a distance of 0.5 nm relative to the break of the G_0 contact. The histogram binning is 100 per decade of conductance for the y -axis and 0.0079 nm for the x -axis. The scale bar shows points per trace. The inset shows individual conductance traces. (b) Logarithm-binned conductance histograms generated using a bin size of 100/decade for compounds **Si1-5**. (c) Conductance peak values of the single-molecule junctions for the **Si n** (black) and **C n** (red) series as functions of the effective molecular length (L , in Å), defined as the distance between the carbons para to the methylthio substituent. L was determined from crystal structures Chem3D and DFT calculations. The values thus obtained varied insignificantly (<3%). The measured decay constants β were $0.27 \pm 0.01 \text{ \AA}^{-1}$ for **Si n** and $0.68 \pm 0.05 \text{ \AA}^{-1}$ for **C n** .

Figure 3.11 59

B3LYP/6-31G**-calculated HOMOs of (a) tetrasilane **Si4**, (b) butane **C4**, and (c) 1,4-bis(4-(methylthio)phenyl)buta-1,3-diene (**6**).

Figure 4.1 75

(a) Top panel: Schematic of the STM-BJ setup modified to perform thermal measurements. Bottom panel: Simplified diagram illustrating measurement of thermoelectric current (I_T) when a temperature gradient is imposed. (b) Top panel: Piezo ramp used, including a “hold” portion between 150 and 200 ms. Middle panel: External

applied voltage across the leads which drops to zero during the center of the “hold” portion. Bottom panel: Sample trace for an example molecular junction. The measured current is shown in red and the voltage measured across the junction is shown in blue.

Note: The voltage is applied across the junction in series with a $10\text{ k}\Omega$ resistor.

Figure 4.2 77

(a) Average measured conductance histograms for molecules **1** (top) and **4** (bottom) for the three ΔT s ($\Delta T = 0\text{ K}$, green; $\Delta T = 14\text{ K}$, blue; and $\Delta T = 27\text{ K}$, red). (b) Average thermoelectric current histograms for molecules **1** (top) and **4** (bottom) for the three ΔT s ($\Delta T = 0\text{ K}$, green; $\Delta T = 14\text{ K}$, blue; and $\Delta T = 27\text{ K}$, red). For **1**, the thermoelectric current shifts left with increasing ΔT , while for **4**, the thermoelectric current shifts right.

Figure 4.3 78

Histograms of Seebeck coefficient for all molecules **1–5**. Histograms are fit with Gaussians (red). **1** and **2** exhibit positive S while **4** and **5** exhibit negative S . The Seebeck coefficient for **3** is close to zero.

Figure 4.4 81

Upper panel: The optimized geometries for junctions with molecules (a) **1** and (b) **4**. Lower panel: Transmission curves shown on a log scale for both molecules calculated using DFT+ Σ . Arrow indicates the position of the Au-d states. Insets: Transmission curves around E_F on a linear scale.

Figure 4.5 87

(a) Schematic of the STM-BJ set-up representing thermoelectric measurement of **P1–P4**.
(b) Conductance histograms of **P2–P4** obtained during the thermoelectric measurement.

The bin size is $10^{-4} G_0$. Inset: Conductance plotted as a function of number of phenyls in the molecular backbone.

Figure 4.6 88

Two-dimensional conductance histograms of **P2-P4**. Representative conductance traces for each molecule is shown as superimposed dotted lines. The bins have a width of 0.008 nm along the displacement axis and 100/decade along the conductance axis. The molecular plateau between 10^{-5} and $10^{-4} G_0$ in the 2D histogram for **P2** is due to the dimer molecule formed *in situ*.

Figure 4.7 90

(a) Average thermoelectric current histograms for **P2** for $\Delta T=0$ K (black, 386 traces) and $\Delta T=14$ K (red, 129 traces). The histogram at $\Delta T=14$ K is multiplied by a factor of 10 and fit with a Gaussian (dotted line). (b) Histograms of thermopower for **P1/Au** (582 traces) and **P2** (530 traces), **P3** (629 traces), and **P4** (2,942 traces). Gaussians fits to the histograms are also shown. Inset: Molecular thermopower plotted as a function of number of phenyls in the molecular backbone.

Figure 4.8 94

(a) Top: The optimized geometry of a **P4** junction with an isosurface plot of the scattering state at the Fermi energy. Bottom: Schematic diagram of the tight-binding model for **P4**. Transmission curves shown on a log scale for **P1-P4** (b) calculated using DFT and (c) as determined by the tight binding model using the best-fit parameters.

Figure 4.9 96

(a) Conductance values and (b) thermopower determined form the experiment, tight-binding model, and DFT as a function of the number of phenyl units in the chain.

Figure 5.1 107

(a) Schematic of experimental set-up: V_A is the applied bias voltage, I is the measured current and V_M is the voltage measured across the junction. The $\sim 100 \text{ k}\Omega$ series resistor is also shown. Structures of all three molecules are also shown. The N-N lengths of these molecules are about 1.2 nm, 1.3 nm and 0.9 nm for 1, 2, and 3 respectively. The molecules bind to the gold leads through the lone pair of the amines, represented here by arrows. (b) Normalized conductance histograms for all three molecules measured with a bias $V_M = 45 \text{ mV}$ and a 1mM solution of the molecules in 1,2,4-Trichlorobenzene. A linear bin size of $10^{-5} G_0$ is used for 1 and 2 (showing molecular peak and conductance quantum peaks), and a bin size of $10^{-6} G_0$ is used for 3. The peaks, determined using Lorentzian fits (or Lorentzian fit with background subtraction for 2), are marked with arrows. Inset: Sample measured traces for each of the three molecules showing the molecular conductance steps. All traces except for the extreme left trace have been offset horizontally to the right for clarity.

Figure 5.2 110

Linearly-binned normalized conductance histograms constructed from over 5000 traces without data selection for (a) 1, (b) 2, and (c) 3 measured at four different bias voltages, V_M . The peak locations are tracked by the arrows. Note: The histograms have been offset vertically for clarity.

Figure 5.3 111

(a) Sample trace measured during a voltage sweep for molecule 1. The piezo displacement (grey line) is shown in the upper panel. The measured current (red, left axis) and voltage (blue, right axis) are shown in the bottom panel. Note that the voltage is

very low when the junction conductance is low due to the series resistor. (b) Multiple sample current-voltage traces for molecules **1** (upper panel) and **2** (lower panel). These traces are obtained from the middle section of the voltage sweep, with V_M starting at +450 mV and ending at -350mV and are chosen to illustrate the variety in measured traces. (c) Schematic level alignment diagram for two different biases showing the change in charge transfer (extent of grey shaded region within the bias window) between the molecule and metal at a large applied bias.

Figure 5.4 112

(a) and (b) Two-dimensional current-voltage histogram for **1** and **2** made from about 4500 and 6000 individual $I-V_M$ traces, respectively. The current bin size is 0.5nA and the voltage bin size is 5 mV. A vertically cross-section (black line) is displayed in the inset. The upper part is fitted with a Gaussian (red curve) in order to extract the peak location.

(c) I-V curves for **1** (red), **2** (blue) and **3** (green) determined from the peak locations of the cross-sections at all voltage bins, like those shown in the insets of (a) and (a). The curves represent the most frequently measured current as a function of bias voltage.

Inset: Relative differential conductance (dI/dV) for **1**, **2**, and **3** normalized to the respective differential conductance values at $V_M = 45$ mV. These are obtained from the slopes of the linear fits to the IV curves in a small voltage interval about each voltage.

Figure 5.5 115

Average IV curves determined from 2D $I-V_M$ histograms using a small ramp (± 450 mV) or large ramp (± 900 mV) for all three molecules. Each averaged IV curve is determined from one tip/sample pair and two or three such data sets are superposed for each

molecule and ramp value. Variations in the IV curves from the small and large bias ramps are larger for **1** and **2** than the variations.

Figure A.1 129

Conductance histograms for **C6SnPh₃**, **C6** and **C9**, generated from over 15000 conductance traces, without any data selection. Histogram bin size is $10^{-5}G_0$. Inset: Conductance histogram peak position versus number of methylene groups for all data in Figure 3.1(d) and for **C9** (green circle).

Figure A.2 131

(a) Conductance histogram for **C6** showing the peak region highlight the conductance window used to determine traces with conductance plateaus. Inset: Conductance window shown for sample traces. (b) Histogram of the length of continuous plateau segments for **C6**. A total of 2682 plateau segments were determined from the selected 700 traces. Inset: Sample conductance traces showing individual segments.

Figure A.3 133

(a) Conductance histograms from measurements of **P1** and **P1d** at a 25 mV bias. (b) Conductance histograms from measurements of **P1** and **4FP1** at a 25 mV bias. (c) Conductance histograms from measurements of **P2** and **P2a** at a 250 mV bias.

Figure A.4 135

Conductance histograms for several control molecules shown with logarithmic binning. None show a significant conductance peak in the measurable range of conductance. The molecules include the synthetic precursors as well as possible linkerless/oxidized products.

Figure A.5 136

Linearly binned histograms for **Si1-5** constructed with a bin size of 10^{-6} G₀. The histograms have been offset vertically for clarity.

Figure A.6 137

Logarithmically binned histograms for **C2-4**. The histograms are constructed with a bin size of 100/decade. The peak of each histograms is marked with a downward arrow.

Figure A.7 138

Two-dimensional conductance histograms for **Si2-5**. The each show a molecule dependent conductance plateau which increases in length with increasing length of the molecule.

Figure A.8 140

Conductance histograms of the five molecules under study. The histograms were each formed from 1000 traces without any sort of data selection using a bin size of 10^{-5} G₀ and are plotted on a log-log scale. The white regions denote the windows used for selection of thermal current measurements. For **4**, the dark grey region represents the region of the low-conducting configuration.

Figure A.9 142

Histograms for average conductance (left) and thermal current (right) for (a) **(2)**, (b) **(3)**, and (c) **(5)** for each of the three ΔT 's.

Figure A.10 143

Histograms of thermal current (left) at each of the three ΔT 's and histogram of molecular Seebeck coefficient (right) for the low-conducting state of 4,4'-bipyridine.

Figure A.11 145

Structures of the molecules used in the STM-BJ experiment. The trimethyltin end groups cleave off both sides in situ allowing the terminal carbons to covalently bind to the gold electrodes.

Figure A.12 145

Two-dimensional conductance histograms of **C6**, **C8**, and **C10**. Thousands of conductance traces are aligned at the rupture of the gold point contact to generate the 2D histograms. The bins have a width of 0.008 nm along the displacement axis and 100/decade along the conductance axis. The feature between 10^{-5} and 10^{-4} G_0 in the 2D histogram for **C6** is due to the in situ formation of the dimer molecule, **C12**.

Figure A.13 146

Top: Piezo ramp used, including a “hold” portion between 150 and 200 ms. Middle: External applied voltage across the leads which drops to zero during the center of the “hold” portion. Bottom: Sample trace for molecular junction. The measured current is shown in red and the voltage measured across the junction is shown in blue.

Figure A.14 147

Average thermoelectric current histograms for **P1/Au** (582 traces), **P3** (629 traces), and **P4** (2,942 traces) for $\Delta T \sim 14$ K. The thermoelectric current histograms for each at $\Delta T = 0$ K (not shown) are narrow and centered at 0 nA and are represented here by dotted lines.

Figure A.15 148

Histograms of thermopower for **C6** (250 traces), **C8** (506 traces), and **C10** (1,815 traces). The histograms are fit with Gaussians to determine the most frequently measured

molecular junction thermopower. The peak thermopower for all three alkanes is 5.0-5.6 $\mu\text{V/K}$. The width of the **C10** distribution is attributed to signal to noise limitations.

Figure A.16 149

Lorentzian transmission functions determined individually for each of the oligophenyls measured using the measured values of conductance and thermopower following the equations given above.

Figure A.17 150

Cond Transmission functions determined by solving the Hamiltonian that treats each individual phenyl as a separate state, but does not include the gateway state. The parameters used are: $E_0 = -3.87$, $\Gamma = 2.74$, $\delta = -1.6$. A comparison of the model with experiment is also shown.

Figure A.18 151

Transmission functions determined for all oligophenyls following the equations given above using the parameters: $\epsilon = -0.21$, $\Gamma = 0.97$, $\delta_0 = -0.45$ and $\beta = 2.4$. A comparison of the model with experiment is shown in the bottom right panel.

Figure A.19 152

(a) The optimized geometry of a **C6** junction with an isosurface plot of the scattering state at the Fermi energy. (b) Transmission curves calculated using DFT shown on a log scale for **C1**, **C4**, **C6**, and **C8**. (c) Conductance and (d) thermopower given as a function of molecular length for both experiment and DFT.

List of Tables

Table 4.1	79
Experimental and DFT+ Σ calculated values for conductance (G) and thermopower (S). Also given are the experimental values for the molecular power factor (GS^2).	
Table 4.2	91
Experimental conductance (G), thermopower (S), and power factor (GS^2) for directly bonded junctions. The power factor for P2 is exceptionally high.	
Table A.1	141
Number of traces selected for each molecule at each ΔT .	

Acknowledgments

For any graduate student, traveling down the road to completion of a Ph.D. dissertation involves dedicating an immense amount time and energy to learning, and to this, I am no exception. Most obviously, I had to learn the ins and outs of what it meant to do scientific research. I had to study the background and the basics to formulate a question, develop and practice the experimental skills and techniques to test it, learn how to interpret the data and determine its relevance, and communicate the results both in print and verbally. Though, gaining knowledge of the scientific nature only constitutes a small percentage of the learning I did during my time in graduate school. More broadly, I learned – for lack of a better phrase – how the world works and there are many, many people who have helped me get to this point. To each and every one them I am forever grateful and indebted.

First and foremost, my advisor, Dr. Latha Venkataraman, deserves an enormous amount of credit. Your steadfast support and guidance kept me motivated throughout all of the ups and downs of graduate life. You always seemed to ask the pertinent questions – a mark of any successful scientist – and strived to fully understand the answers, and then in turn, took time to fully explain them to me as I sat there confused. I remember how the question segment of my first APS March meeting presentation made you nervous enough to lose sleep the night before and you shared this with me in an attempt to help me calm my own nerves. You also allowed me to learn from, work with, and get to know an unusually high number of collaborators and stepped in to help when my time management skills were challenged because of this. Thank you for all

of the lab lunches, dinners, and celebrations, and most of all, thanks for all you have done for me over the last six years.

Equally deserving of credit for my work are my parents, Janet and Michael, and my younger sister, Lauren. To you, graduate school must seem like a black box which a student ventures into, then isn't heard from for years, and yet, somehow, eventually emerges with a piece of paper that calls him a doctor. Looking back on it, I must have been "starting my thesis" for a year or two, and to borrow a quote from Dean Goldfarb, had it "written in my head" for even longer. I thank you and the rest of the Houses Widawsky and Wong (sorry... Game of Thrones is big right now) for all your patience, love, support, and more patience.

Then there are those who tried their best to make graduate school more fun for me, namely my friends, labmates, colleagues, and fellow graduate students. Thanks for letting me drag you to all those Mets games, to karaoke and bowling, and on outings for strange food and various excursions. Who would have thought I could find other people to debate physics, sports, and other random stuff with for hours on end? Needless to say, living in New York is truly a unique experience.

And lastly, I want to thank those of you who have offered me your support during my toughest times, whether you are someone I know personally or have never had the opportunity to meet. As I close this chapter of my life and look forward into the future, I am truly excited about the things to come.

Sincerely,
Jonathan Widawsky

To Annie

Chapter 1

Introduction

1.1 Motivation – Single Molecule Junctions

When asked to motivate the study of single molecule junctions, we respond by saying that it can help answer many of the technological questions and challenges posed in today's society. But what exactly is a single molecule junction, what can we learn from it, and how can what we learn be useful? The idea behind a single molecule junction is simple – attach a single molecule to metallic electrodes and pass a current through it (see Figure 1.1 for illustration). Yet in practice, creating molecular junctions reliably and reproducibly, so that pertinent transport studies can be performed, has proven to be a tough experimental challenge. The primary question that arises usually addresses the confidence that a junction with one – and only one – molecule has been successfully constructed and characterized. Second, concerns are raised about whether a target molecule can be designed and synthetized with useful intrinsic properties. Lastly, mainly in order to achieve this, discovery of what we need to know in terms of fundamental physics to be able to engineer and control functionality at this scale still remains. These are precisely the critical issues that surround the field of molecular electronics.

Since the birth of the solid state transistor[1] more than sixty years ago, extensive effort has been invested into miniaturizing circuit components. This was due to the growing demand for fast, energy efficient, and cheap methods to compute and store immense amount of data information. The most telling gauge for this was proposed by Intel co-founder Gordon E. Moore, thereby inspiring his eponymous law[2], which tracked the exponentially shrinking size of the silicon transistor with time. As the transistor gate length approaches the 10s of nanometers, silicon technology has reached a physical limit[3, 4]. Bulk solid state properties are no longer applicable at lengths of this scale, making the impact of impurities, heating, or leakage current significant. Studying single molecule junctions allows us to probe charge transport at the

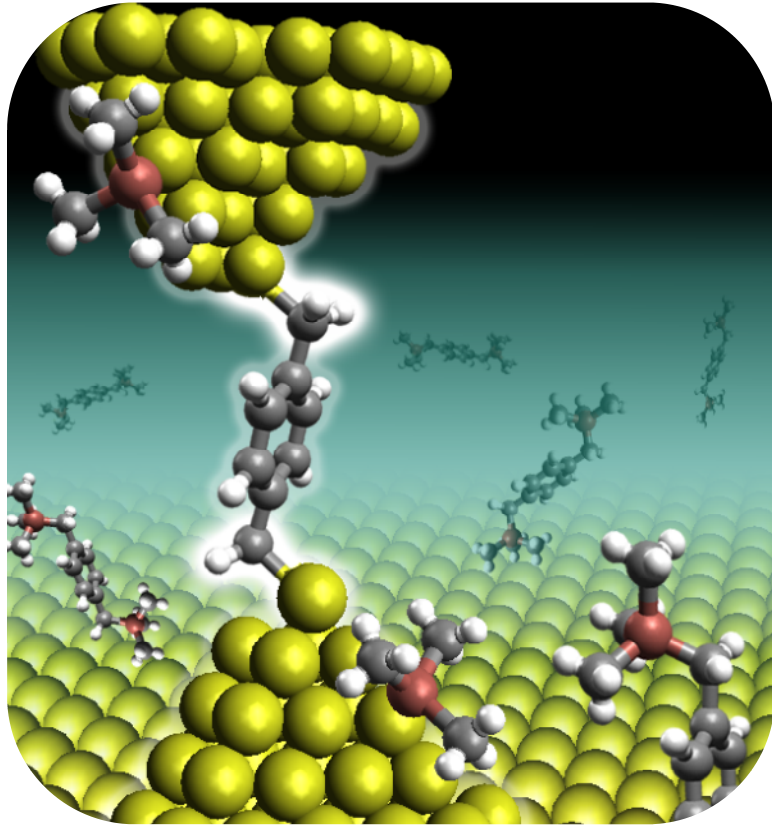


Figure 1.1: Illustration of a single molecule junction. The linker groups have separated from the molecule and as a result, the molecular backbone is directly attached to the gold electrodes.

nanoscale, where systems are governed by the laws of quantum mechanics. At the nanometer level, classical Drude-type diffusive transport[5], where the magnitude of current flow obeys Ohm's Law ($V=IR$; $R=\rho L/A$), ceases to be directly applicable. Transmission of charge carriers through the junction now becomes ballistic[6, 7]; the charge carrier can traverse the entire length of the junction devoid of interaction with a scattering site. Understanding how this works, while keeping the hope of developing viable molecular electronics in mind, is essential.

The first molecular device was proposed in a paper by Aviram and Ratner[8] in 1974, in which the authors suggest that a molecule with two, effectively-separated electron systems – where, through the use of chemical substituents, one is electron donating (“n-doped”) and the other is electron withdrawing (“p-doped”) – can act as a molecular rectifier[9]. Since then, many

new ideas have been proposed towards the development of a broad list of molecular sensors[10, 11], switches[12-17], transistors[18, 19], and potentiometers[20, 21], etc., controlled by mechanics light, electrochemistry, or through chemical reactions under a multitude of different environmental conditions. Unfortunately, until the last decade, being able to capture a single molecule and hold it in a junction long enough to do apposite electronic transport measurements had largely eluded the scientific community. Lithographic fabrication techniques served as the basis for first attempts to construct SAM or single molecule junctions[22-24] beginning in the late 1990s, and while good results were reported, agreement and reproducibility across the studies were questioned. The problem was that the gap between the electrodes was often too wide for a single molecule to span or that contact to a few molecules was being made. Steps have been taken to create smaller gaps with the more recent development of electromigration-based fabrication[25-29], but state of the art methods have also involved the implementation of break junctions. Because these methods involved the repeated, quick formation and rupture of metal point contacts, they allowed for the measurement and statistical analysis of many individual single molecule junctions[30-32]. Today, the two most commonly used techniques are the mechanically controlled break junction (MCBJ)[33-35] and scanning tunneling microscope break junction (STM-BJ)[36, 37]. STM-BJ is the main tool employed in the studies herein.

1.2 Outline

The focus of this Thesis is the development of highly conducting single molecule junctions and study of their electronic and thermoelectric conduction properties. This opens the door for the investigation of fundamental quantum transport physics. More specifically, it allows us to better understand charge transport across organic/inorganic interfaces and across specific media. The following is an outline of the work carried out in this Thesis:

Chapter 2: Here, I describe the experimental setup and the steps taken to determine the electrical conductance of single molecules attached to gold leads using the STM-BJ technique. This involves the acquisition of thousands of conductance traces that are analyzed statistically through the use of both one-dimensional and two-dimensional conductance histograms. Also, I describe how the experimental procedure is modified to make thermoelectric and large bias transport measurements. Finally, using a single level model for transmission, I will explain how the molecular orbitals, and their alignment to the Fermi level of the electrodes, play a key role in determining the low-bias properties of the junction.

Chapter 3: In this chapter, I will break down transport across a molecular junction by focusing on two aspects of the junction – 1) the nature of the bond between the organic backbone of the molecule and the inorganic electrode and 2) the conductive nature of the backbone itself. We have developed a method to bypass the use of traditional linker groups and directly attach the molecular backbone to the electrode with a covalent bond

(Figure 1.1). This allows us to form strongly bound junctions while minimizing the effect of contact resistance. In addition, we demonstrate that using a silicon chain as the molecular backbone instead of a saturated organic alkane can dramatically affect the conduction properties we observe.

Chapter 4: Single molecule conductance measurements have also been extended to the study of thermoelectrics. The development of viable organic thermoelectric devices has centered on finding materials that maximize the thermoelectric figure of merit, ZT. One strategy to increase the figure of merit is to focus on improving the power factor, GS^2 , the numerator of ZT. Measuring material performance at the single-molecule level can provide a better understanding of structure-function relations in these systems. In this chapter, we investigate the thermoelectric properties of a few systems of molecular junctions, including those with amine and pyridine linkers, as well as the highly conducting junctions discussed in Chapter 3. Several models are introduced to explain the trends observed in experiment. Additionally, since we can simultaneously determine conductance and thermopower, we are able to evaluate and compare the power factors of the molecule junctions.

Chapter 5: Chapter 5 is centered on the measurement of molecular current-voltage (I-V) curves. In this work, we explore the electronic and physical effects of applying a large bias to the system. We observe an inherent difference in the response of electron/LUMO-conducting junctions and hole/HOMO-conducting junctions and investigate the mechanism behind this. Also, we see that the degree of non-linearity of

the I-V curves depends on the proximity of the conducting orbital to the Fermi energy of the electrodes. Consequently, I-V measurements tell us about properties of the transmission functions complimentary to zero-bias conductance and thermopower measurements.

Chapter 6: Conclusions and outlook.

1.3 References

1. Bardeen, J. and W.H. Brattain, *The Transistor, A Semi-Conductor Triode*. Physical Review, 1948. **74**(2): p. 230-231.
2. Moore, G., *Cramming more components onto integrated circuits*. Electronics, 1965. **38**: p. 114–117.
3. Schulz, M., *The end of the road for silicon?* Nature, 1999. **399**(6738): p. 729-730.
4. Muller, D.A., T. Sorsch, S. Moccio, F.H. Baumann, K. Evans-Lutterodt, and G. Timp, *The electronic structure at the atomic scale of ultrathin gate oxides*. Nature, 1999. **399**(6738): p. 758-761.
5. Ashcroft, N.W. and N.D. Mermin, *Solid State Physics*.
6. Datta, S., *Electronic Transport in Mesoscopic Systems*. 1995: Cambridge University Press.
7. Paulsson, M. and S. Datta, *Thermoelectric effect in molecular electronics*. Physical Review B, 2003. **67**(24): p. 241403.
8. Aviram, A. and M.A. Ratner, *Molecular Rectifiers*. Chemical Physics Letters, 1974. **29**(2): p. 277-283.
9. Díez-Pérez, I., J. Hihath, Y. Lee, L. Yu, L. Adamska, M.A. Kozhushner, I.I. Oleynik, and N. Tao, *Rectification and stability of a single molecular diode with controlled orientation*. Nat Chem, 2009. **1**(8): p. 635-641.
10. Leary, E., H. Hobenreich, S.J. Higgins, H. van Zalinge, W. Haiss, R.J. Nichols, C.M. Finch, I. Grace, C.J. Lambert, R. McGrath, and J. Smerdon, *Single-Molecule Solvation-Shell Sensing*. Physical Review Letters, 2009. **102**(8): p. 086801.
11. Choi, Y., I.S. Moody, P.C. Sims, S.R. Hunt, B.L. Corso, I. Perez, G.A. Weiss, and P.G. Collins, *Single-Molecule Lysozyme Dynamics Monitored by an Electronic Circuit*. Science, 2012. **335**(6066): p. 319-324.
12. Whalley, A.C., M.L. Steigerwald, X. Guo, and C. Nuckolls, *Reversible switching in molecular electronic devices*. Journal of the American Chemical Society, 2007. **129**(42): p. 12590-+.
13. Sense Jan van der, M. and L. Peter, *Charge transport through molecular switches*. Journal of Physics: Condensed Matter, 2010. **22**(13): p. 133001.

14. Martin, S., W. Haiss, S.J. Higgins, and R.J. Nichols, *The Impact of E-Z Photo-Isomerization on Single Molecular Conductance*. Nano Letters, 2010. **10**(6): p. 2019-2023.
15. He, J., F. Chen, P.A. Liddell, J. Andreasson, S.D. Straight, D. Gust, T.A. Moore, A.L. Moore, J. Li, O.F. Sankey, and S.M. Lindsay, *Switching of a photochromic molecule on gold electrodes: single-molecule measurements*. Nanotechnology, 2005. **16**(6): p. 695-702.
16. Markussen, T., J. Schiotz, and K.S. Thygesen, *Electrochemical control of quantum interference in anthraquinone-based molecular switches*. The Journal of Chemical Physics, 2010. **132**(22): p. 224104-6.
17. Quek, S.Y., M. Kamenetska, M.L. Steigerwald, H.J. Choi, S.G. Louie, M.S. Hybertsen, J.B. Neaton, and L. Venkataraman, *Mechanically controlled binary conductance switching of a single-molecule junction*. Nature Nanotechnology, 2009. **4**(4): p. 230-234.
18. Song, H., Y. Kim, Y.H. Jang, H. Jeong, M.A. Reed, and T. Lee, *Observation of molecular orbital gating*. Nature, 2009. **462**(7276): p. 1039-1043.
19. Osorio, E.A., K. O'Neill, M. Wegewijs, N. Stuhr-Hansen, J. Paaske, T. Bjørnholm, and H.S.J. van der Zant, *Electronic Excitations of a Single Molecule Contacted in a Three-Terminal Configuration*. Nano Letters, 2007. **7**(11): p. 3336-3342.
20. Meisner, J.S., M. Kamenetska, M. Krikorian, M.L. Steigerwald, L. Venkataraman, and C. Nuckolls, *A Single-Molecule Potentiometer*. Nano Letters, 2011. **11**(4): p. 1575-1579.
21. Battacharyya, S., A. Kibel, G. Kodis, P.A. Liddell, M. Gervaldo, D. Gust, and S. Lindsay, *Optical Modulation of Molecular Conductance*. Nano Letters, 2011. **11**(7): p. 2709-2714.
22. Chen, J., M.A. Reed, A.M. Rawlett, and J.M. Tour, *Large On-Off Ratios and Negative Differential Resistance in a Molecular Electronic Device*. Science, 1999. **286**(5444): p. 1550-1552.
23. Collier, C.P., E.W. Wong, M. Belohradský, F.M. Raymo, J.F. Stoddart, P.J. Kuekes, R.S. Williams, and J.R. Heath, *Electronically Configurable Molecular-Based Logic Gates*. Science, 1999. **285**(5426): p. 391-394.
24. Cui, X.D., A. Primak, X. Zarate, J. Tomfohr, O.F. Sankey, A.L. Moore, T.A. Moore, D. Gust, G. Harris, and S.M. Lindsay, *Reproducible measurement of single-molecule conductivity*. Science, 2001. **294**(5542): p. 571-574.
25. Liang, W.J., M.P. Shores, M. Bockrath, J.R. Long, and H. Park, *Kondo resonance in a single-molecule transistor*. Nature, 2002. **417**(6890): p. 725-729.

26. Ward, D.R., G.D. Scott, Z.K. Keane, N.J. Halas, and D. Natelson, *Electronic and optical properties of electromigrated molecular junctions*. Journal of Physics: Condensed Matter, 2008(37): p. 374118.
27. Park, H., A.K.L. Lim, A.P. Alivisatos, J. Park, and P.L. McEuen, *Fabrication of metallic electrodes with nanometer separation by electromigration*. Applied Physics Letters, 1999. **75**(2): p. 301-303.
28. Prins, F., T. Hayashi, B.J.A.d.V. van Steenwijk, B. Gao, E.A. Osorio, K. Muraki, and H.S.J. van der Zant, *Room-temperature stability of Pt nanogaps formed by self-breaking*. Applied Physics Letters, 2009. **94**(12): p. 123108-3.
29. Park, J., A.N. Pasupathy, J.I. Goldsmith, C. Chang, Y. Yaish, J.R. Petta, M. Rinkoski, J.P. Sethna, H.D. Abruna, P.L. McEuen, and D.C. Ralph, *Coulomb blockade and the Kondo effect in single-atom transistors*. Nature, 2002. **417**(6890): p. 722-725.
30. Mayor, M. and H.B. Weber, *Statistical Analysis of Single-Molecule Junctions*. Angewandte Chemie International Edition, 2004. **43**(22): p. 2882-2884.
31. Lörtscher, E., H.B. Weber, and H. Riel, *Statistical Approach to Investigating Transport through Single Molecules*. Physical Review Letters, 2007. **98**(17): p. 176807.
32. Williams, P.D. and M.G. Reuter, *Level Alignments and Coupling Strengths in Conductance Histograms: The Information Content of a Single Channel Peak*. The Journal of Physical Chemistry C, 2013. **117**(11): p. 5937-5942.
33. van Ruitenbeek, J.M., A. Alvarez, I. Pineyro, C. Grahmann, P. Joyez, M.H. Devoret, D. Esteve, and C. Urbina, *Adjustable nanofabricated atomic size contacts*. Review of Scientific Instruments, 1996. **67**(1): p. 108-111.
34. Reed, M.A., C. Zhou, C.J. Muller, T.P. Burgin, and J.M. Tour, *Conductance of a molecular junction*. Science, 1997. **278**(5336): p. 252-254.
35. Reichert, J., R. Ochs, D. Beckmann, H.B. Weber, M. Mayor, and H. von Lohneysen, *Driving current through single organic molecules*. Physical Review Letters, 2002. **88**(17): p. 176804.
36. Tao, N.J.J., *Measurement of Single-Molecule Resistance by Repeated Formation of Molecular Junctions*. Science (New York, N.Y.), 2003. **301**(5637): p. 1221-1223.
37. Venkataraman, L., J.E. Klare, I.W. Tam, C. Nuckolls, M.S. Hybertsen, and M.L. Steigerwald, *Single-Molecule Circuits with Well-Defined Molecular Conductance*. Nano Letters, 2006. **6**(3): p. 458 - 462.

Chapter 2

Experimental Framework

2.1 Scanning Tunneling Microscope Setup

According to Newton's laws, an object moving in a potential landscape experiences an exchange of energy between its kinetic motion and stored potential energy. In the absence of outside forces that do work on the system, the total energy ($TE = KE + PE$) must remain constant, and at no point can the object be found at a location where its potential energy is greater in magnitude than its total energy (called the classically forbidden region). This fundamental notion was challenged by realization of quantum mechanics, where quantum particles have the ability to move through potential barriers that exceeds its total energy. This phenomenon is called quantum tunneling and it is the primary mechanism behind the Scanning Tunneling Microscope (STM). The STM was invented by Binnig and Rohrer[1] in 1983 as a means to map the topography of gold and silicon surfaces with sub-angstrom to nanometer resolution. The authors did so by raster-scanning a sharp, metallic tip across the biased substrate while measuring the tunneling current. Displaying the magnitude of the current as a function of location allowed them to generate an image of the surface with atomic resolution[2].

This is the basic principle behind the experimental technique employed in this Thesis. Here, a traditional STM geometry was modified so that the tip could only travel perpendicular to (as opposed to across) the surface. This addition allows us to use the STM to perform the break junction technique[3, 4]. In this method, a gold tip is repeatedly driven into and out of contact with the gold substrate. Upon breakage of the gold point contact, a small gap (~ 0.6 nm) between the tip and substrate opens up. If there are molecules with specific binding groups in the vicinity of the gap between the electrodes, they can bridge the gap and their conductance ($G=I/V$) can be measured. When this is repeated thousands of times, the conductance of a molecular junction can be determined from a statistical analysis.

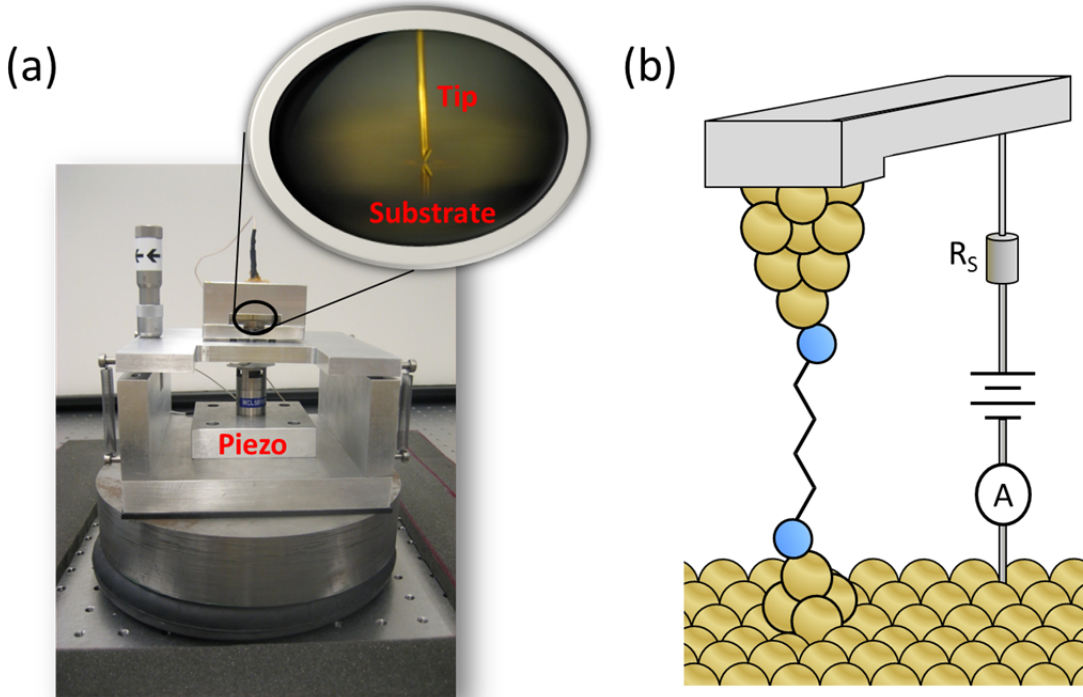


Figure 2.1: (a) Picture of the basic home-built modified scanning tunneling microscope (STM). The commercially acquired piezo actuator gives the system z-axis mobility with sub-angstrom position resolution. Zoom in: Picture of a gold tip cut on an angle to taper above a gold-on-mica substrate. The reflection of the tip is observable in the substrate as well. (b) Schematic of the STM-BJ setup circuit, which includes a series resistor, R_s .

2.1A Description of the Home-Built System and Measurement

The scanning tunneling microscope (STM) used was a home-built system, pictured in Figure 2.1(a), designed only with z-axis mobility and the capability of performing thermal measurements. The conductance of each molecule was measured using an Au tip (Alfa Aesar, 99.999%) cut at an angle to be sharp and a substrate of \sim 100 nm of gold (Alfa Aesar, 99.999%) thermally evaporated onto cleaved mica disks. The substrate is magnetically mounted on a piezoelectric positioner (Mad City Labs, P15), so that sub-angstrom resolution in position is achieved. During the entire break junction procedure, a constant bias (10–350 mV) is applied between the tip and the substrate while the current is measured (Keithley 428-Prog) in series

with a resistor (typically $10\text{ k}\Omega$, but in some cases, up to $1\text{ M}\Omega$). The Keithley I-V converter was chosen because of its large dynamic range, so that, given the influence of the series resistor, currents through junctions from 10s of the quantum of conductance, $G_0 = 2e^2/h = 77.5\text{ }\mu\text{S}$ down to about $10^{-5} G_0$ in gain 6 or to $10^{-7} G_0$ in gain 7 can be measured in a single measurement. Piezo control and data collection were performed using a National Instruments PXI Chassis System (with PXI-4461, PXI-6289) at 40 kHz and driven and managed with a custom-written program using Igor Pro (Wavemetrics, Inc.). The entire apparatus is placed on top of an optical air table (TMC, 63-563) and put under an aluminum/foam hood for acoustic and electrical isolation.

For each experiment, the substrate is cleaned under UV/Ozone for 15 minutes prior to use and the tip is freshly replaced and cut. The system is kept under ambient conditions throughout all of the experiments. First, clean gold breaks are collected to ensure the cleanliness of the setup. Then, the target molecule is deposited on the substrate using one of two methods, depending on the nature of the molecule and the particular experiment being run. In the first case, the analyte is dissolved in 1,2,4-trichlorobenzene (Sigma Aldrich) to produce a $\sim 1\text{ mM}$ solution and drop cast directly onto the substrate. The break junction measurement is therefore carried out in solution as long as the solvent persists, typically about 10 hours. In the second case, the analyte is dry deposited onto the substrate by thermal evaporation or drop cast using a low-boiling solvent, such as acetone or toluene, which is allowed to evaporate before measurement. Because the molecule is analyzed in dry form, the run time can last indefinitely. Every molecule was measured using multiple tip/substrate pairs, on different days, to check for consistency and reproducibility.

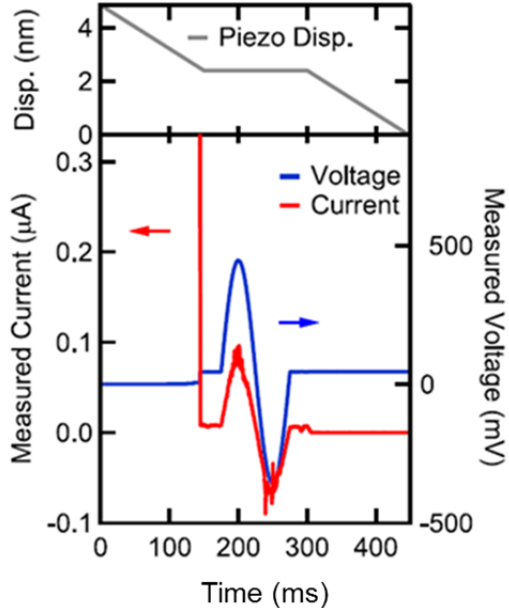


Figure 2.2: Example I-V trace measured during a voltage sweep for a typical molecular junction. The piezo displacement (gray line), shown in the upper panel, includes a momentary hold section to freeze the junction during elongation event. The measured current (red, left axis) and voltage (blue, right axis) are shown in the bottom panel. Note that the voltage is very low when the junction conductance is low due to the series resistor.

At the start of each break junction iteration, the STM tip is brought into hard contact with the substrate so that a conductance greater than $\sim 10 G_0$ is achieved. At this point, the junction electrodes are pulled apart at a speed of 16 nm/s for 0.25 seconds while conductance is recorded. During this time, the initial $10 G_0$ gold contact thins out and ruptures, resulting in the formation of a single molecule junction, which itself proceeds to elongate and rupture. The circuit diagram of a single molecule junction is given in Figure 2.1(b) and example measurements are shown in the next section. For measurement of molecular I-V curves[5], the withdrawal of the tip is temporarily stopped in the middle of the piezo ramp after a distance that ensures the highest likelihood for capture of a molecule in the junction. The tip–substrate distance is held constant for about 150 ms and the applied voltage is ramped either sinusoidally or linearly between $\sim +/ - 1V$ (as seen in Figure 2.2). The current is measured as a function of applied voltage. To confirm that the IV is measured for a single molecule, the conductance is checked immediately before

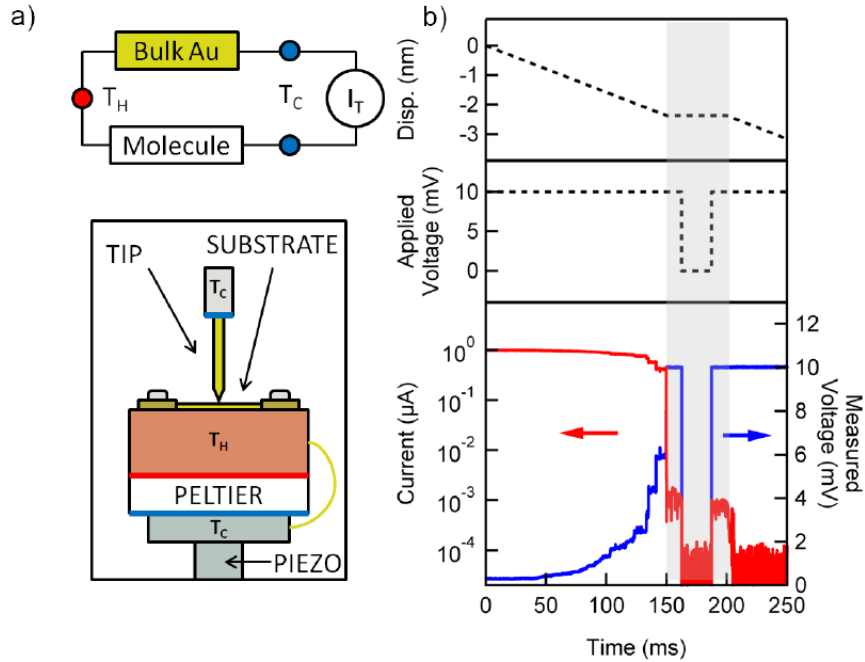


Figure 2.3: (a) Top: Schematic of the STM-BJ setup modified to perform thermal measurements. Bottom: Simplified diagram illustrating measurement of thermoelectric current (I_T) when a temperature gradient is imposed. (b) Top: Piezo ramp used, including a “hold” portion between 150 and 200 ms. Middle: External applied voltage across the leads which drops to zero during the center of the “hold” portion. Bottom: Sample trace for an example molecular junction. The measured current is shown in red and the voltage measured across the junction is shown in blue. Note: The voltage is applied across the junction in series with a $10\text{ k}\Omega$ resistor.

and after the voltage ramp. At the end of this ramp, the applied voltage is again set to be constant and the tip is withdrawn an additional distance to fully break the junction.

2.1B Modifications for Thermal Setup

For measurement of thermoelectric current, the STM-BJ setup was modified[6] as given in Figure 2.3(a). The substrate was mounted onto the hot side of a thermoelectric (Peltier) device, while the cold side was held near room temperature. Additionally, the STM tip was kept near room temperature throughout the measurement. The temperature of the hot side of the Peltier was controlled using a DC power supply (BK Precision, 1750A) between room

temperature and 70°C, though typically only about 40 °C or 50 °C, and recorded using a T- or K-type thermocouple. In order minimize for unaccounted thermoelectric voltages across the leads, a pure gold wire (99.998%) of known thermopower ($S_{Au} = 2 \mu\text{V/K}$ [7]) was connected from the hot side of the Peltier to the cold side to provide electrical connectivity and so that the thermoelectric voltage across the reverse temperature gradient ($-\Delta T$) was known and fixed. As in the I-V measurement, a 50 ms hold portion was added to the piezo ramp (Figure 2.3(b)). During the central two quartiles of the hold (middle 25 ms), the applied bias was dropped to zero, so that all of the current measured here would be due solely to the thermal gradient between the hot substrate and the tip. The data acquisition electronics were carefully calibrated after every 50 measurements to ensure that there were no other sources of bias across the junction. The setup is also allowed to thermally equilibrate for about an hour after adjusting the temperature of the Peltier before the experiment proceeds. A simplified circuit diagram is shown in Figure 2.3(a).

2.2 Conductance Traces, Conductance Histograms, and Statistical Analysis

2.2A Collection of Conductance Traces

Conductance (= current/voltage) is plotted as a function of piezo displacement for every break-junction iteration measured, yielding conductance traces. Conductance traces for clean gold (Figure 2.4(a)) exhibit steps near multiples of G_0 ($= 2e^2/h$), the quantum of conductance[8-11]. (Discussion of the origin of G_0 to follow.) Below 1 G_0 , there is a sharp drop in junction conductance symbolizing the opening of a tunneling gap, which may contribute a few data points but is otherwise featureless. The break of a G_0 contact (or gold point contact) ensures that the resulting electrodes are atomically sharp, so that upon addition of a target molecule, the molecule may bridge the gap and its conductance can be measured.

When a molecule is successfully captured, features at values less than 1 G_0 become evident[3, 4]. Conductance traces for 1,4-diaminobutane (C4A) in Figure 2.4(a) show molecular plateaus at $\sim 10^{-3}$ G_0 in about 30% of traces, and this percentage typically goes up for longer molecules[4]. The STM system takes (on the order of) a single second to record, process, and store each conductance trace. Therefore, up to tens of thousands of conductance traces can be collected during each experiment for a given molecule. The raw data conductance traces are stored as Igor Binary Waves, along with the current and voltage traces for the thermal or I-V measurements when necessary.

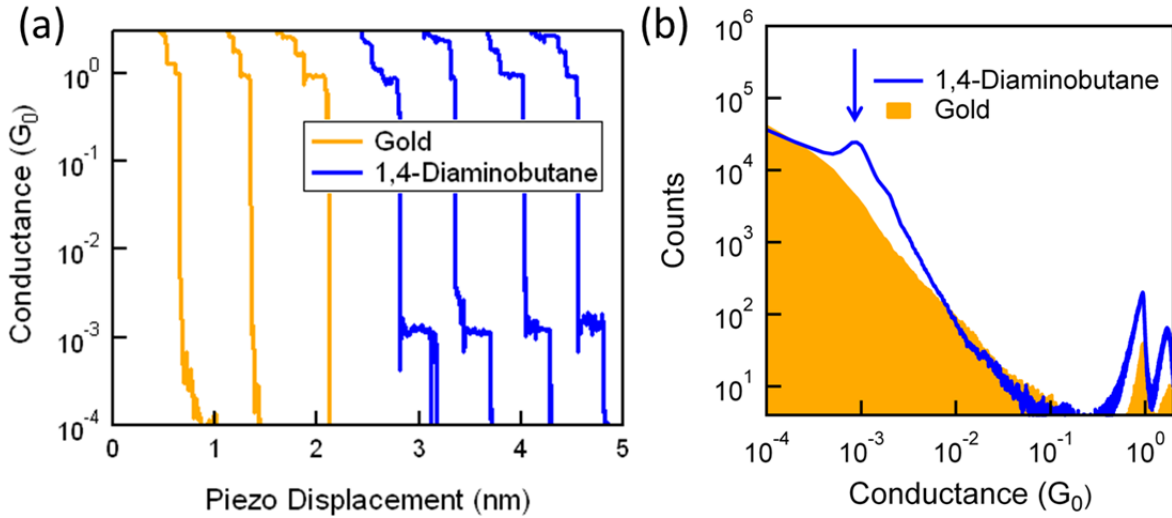


Figure 2.4: (a) Sample conductance traces for clean gold (yellow) and in the presence of 1,4-Diaminobutane (blue) measured at 25 mV. The conductance traces exhibit steps at integer multiples of G_0 . The blue traces also show a molecule-dependent plateau below $1 G_0$ due to the formation of a molecular junction. (b) Conductance histograms for clean gold (solid yellow) and for 1,4-Diaminobutane (blue). The blue histogram exhibits a peak (arrow) above the tunneling background that can be fit to determine the most frequently measured conductance.

2.2B Construction of Conductance Histograms

Due to the trace-by-trace variability within the measurement[12], molecular conductance is defined statistically through the construction of a conductance histogram. The y-axis of each conductance trace is divided into either linearly- or logarithmically-spaced conductance bins into which the data points are collapsed. The histogram is compiled from thousands of traces without any data selection and presented on a logarithmic conductance scale. Peaks in the histogram correspond to values of conductance that are measured more frequently[3, 8]. Conductance histograms for clean gold break junctions contain peaks near multiples of G_0 and a linear tunneling background below G_0 , as shown on a log-log scale in Figure 2.4(b). When a target molecule is introduced into the system, a molecule-dependent peak on top of the linear tunneling background is formed due to conduction through the molecule, as shown for 1,4-diaminobutane in Figure 2.4(b) . The peak can be fit with a distribution function (i.e. Lorentzian, Gaussian, etc.)

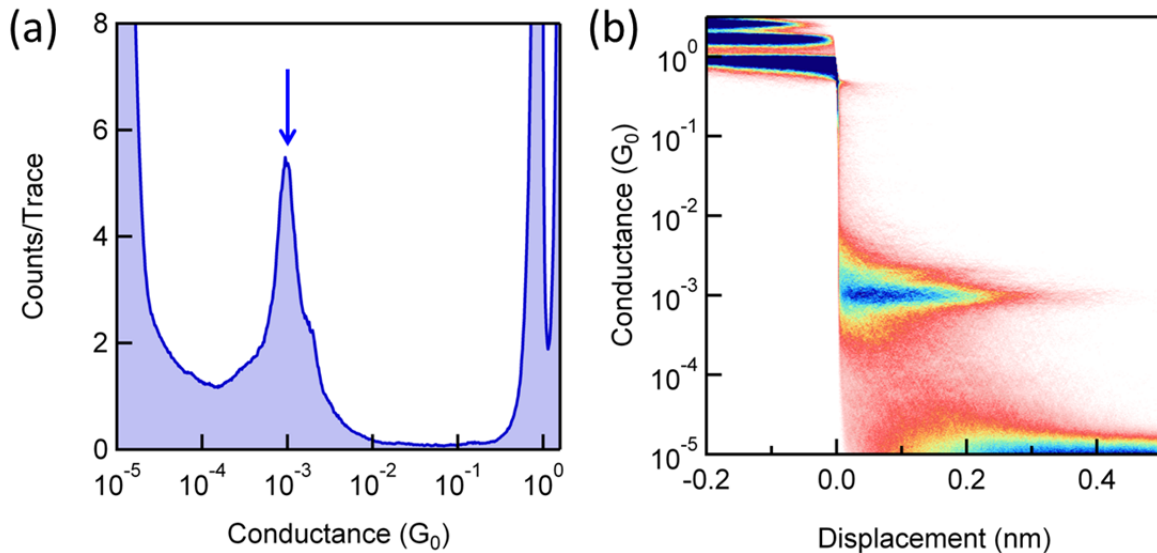


Figure 2.5: (a) Histogram for C4A constructed using a logarithmic binning of 100/decade. (b) Two-dimensional conductance histogram for C4A composed of 10,000 conductance traces measured at 25 mV. Bin sizes of 0.008 nm along the displacement axis and 100/decade along the conductance axis are used. The molecular step at $10^{-3} G_0$ extends to a length 0.3 nm from the rupture of the gold point contact. Clear steps at integer multiple values of G_0 are also evident, as well as the experimental background at $10^{-5} G_0$.

so that the most frequently measured value of conductance, defined as the molecular conductance, can be determined. In this case, for example, the molecular conductance of 1,4-diaminobutane is found to be $8.6 \times 10^{-4} G_0$. Also, constructing the same histogram with logarithmic bins, one method to artificially subtract the background, is shown in Figure 2.5(a).

In some instances, preserving the piezo length information is useful to better define and understand the system. To do this, two-dimensional histograms are constructed[13-15], in which the conductance traces are aligned at the G_0 break and stacked vertically into conductance vs. length histograms. The break is found according to an algorithm by either setting a cross-level threshold value or setting a cutoff parameter on the differentiated conductance trace. Two-dimensional conductance histograms allow for the determination of a conductance step length, which is usually proportional to the length of the molecule and thus an indication of the junction elongation length. The 2D histogram for 1,4-diaminobutane is given in Figure 2.5(b).

2.3 Understanding Molecular Conductance with a Single Level Model

In order to understand why a molecule exhibits a particular conductance, let us first consider a model system with two independent and isolated atoms, so that the atomic orbitals of each atom are identical. If the two atoms are brought together and allowed to interact, the levels of the orbitals would change to make the system more energetically favorable. The simplest case for us to consider is molecular hydrogen. If two 1s hydrogen atoms are brought close together so that the interaction energy between the two is τ , the resulting Hamiltonian becomes

$$H = \begin{bmatrix} \mathcal{E}_{1s} & \tau \\ \tau & \mathcal{E}_{1s} \end{bmatrix}$$

Diagonalization of the Hamiltonian results in the formation of two new states that are linear combinations of the original 1s states and the energies of these states are given by

$$\mathcal{E}_{+-} = \mathcal{E}_{1s} \pm \tau$$

One state, \mathcal{E}_- , called the bonding state, is lower in energy than the original 1s states and is occupied to facilitate energetic stabilization. The second state, \mathcal{E}_+ , which has an energy greater than the 1s states, is called the antibonding state and is empty. A depiction of this energy splitting is given in Figure 2.6(a).

For molecules with a greater number of shell atomic orbitals, the tight binding approach is commonly used to gauge how the orbitals change with interaction. Within the tight binding

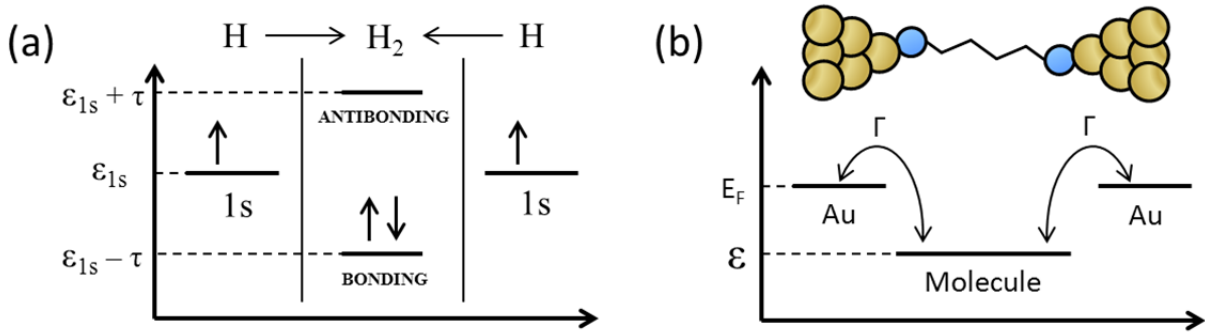


Figure 2.6: (a) Energy level diagram describing the formation of molecular hydrogen. The two original 1s atomic orbitals hybridize to form an occupied bonding state and unoccupied antibonding state. (b) Energy level diagram of a ‘single-level’ molecule bound to metallic electrodes with coupling Γ . A picture of a junction with C4A is given as well.

formalism, hybridization only occurs between the valence atomic orbitals while core atomic orbitals remain largely unaffected. These hybridized molecular levels are filled to a particular energy state, called the highest occupied molecular orbital (HOMO) (for H_2 , the bonding state). Beyond that, the states are empty, and the first of these is called the lowest occupied molecular orbital (LUMO) (for H_2 , the antibonding state). The energies of these molecular states are one of the factors affecting the molecular conductance.

Let us now assume that only one of these molecular orbitals is responsible for conduction and that we bring this ‘one-level’ molecule close to an electrode. The electrode exhibits a continuous distribution of energy states, which are filled to an energy E_F , the Fermi level. The energy of the molecular orbital will shift as it interacts with the electrode due charge transfer and image charge effects. Also, according to the Heisenberg uncertainty principle, given a state lifetime τ , the molecular level will go from being discrete to broadened (as $\hbar/2\tau$) due to coupling to states in the electrode. Let us denote \mathcal{E} as the difference in energy between the Fermi energy of the electrodes and the adjusted molecular orbital and Γ as the level-broadening parameter which arises from the electronic coupling. The transport model for this is shown Figure 2.6(b). Both \mathcal{E} and Γ could be different for different molecules and both can independently affect the

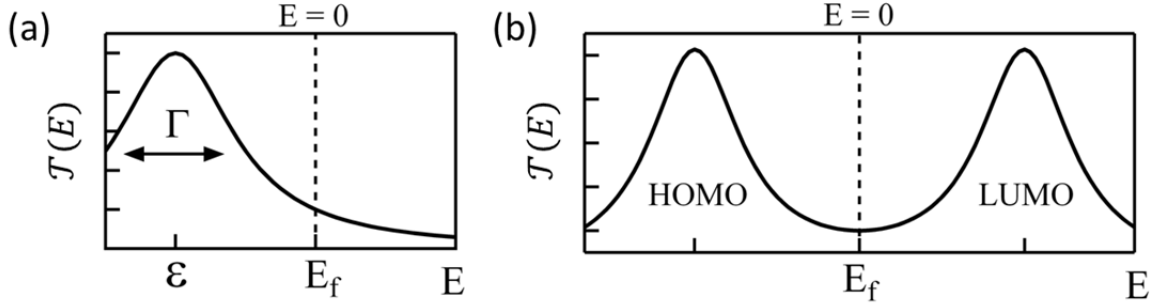


Figure 2.7: (a) Example of a single Lorentzian transmission function. The conductance of the junction is equal to the value of the transmission function at the Fermi energy in units of G_0 , the quantum of conductance. (b) Example of a double Lorentzian transmission function, with the Fermi energy shown between the highest occupied and lowest unoccupied molecular orbitals.

tunnel conductance across the molecular junction. The coupling can be approximated as an imaginary correction to the orbital energy, so that

$$\mathcal{E} \rightarrow \mathcal{E} - i\Gamma$$

From this, the transmission function, $\mathcal{T}(E)$, can be calculated according using the Green's function formalism[16-18]. When the coupling to the left and right electrodes is equal ($\Gamma_L = \Gamma_R \equiv \Gamma$), the transmission function is Lorentzian[19] and of the form

$$\mathcal{T}(E) = \frac{\Gamma^2}{|E - \mathcal{E}|^2} = \frac{\Gamma^2}{(E - \mathcal{E})^2 + \Gamma^2}$$

A sample Lorentzian transmission curve is given in Figure 2.7(a). The low-bias conductance, G , is determined using the formula derived by Landauer[20] for transport through a one-dimensional system. For a single, perfectly conducting 1D channel, $G = G_0 = 2e^2/h = 77.5 \mu S$, and is defined as the quantum of conductance[21]. When conduction occurs through a

multi-channel 1D system, the conductance is equal to the sum of the transmission probabilities through the conducting channels given in units of G_0 , so that[18]

$$G = G_0 \sum_{i=1}^M \mathcal{T}_i$$

where M is the number of conducting channels and \mathcal{T}_i is the probability of transmission through particular channel i . In the case of our ‘single level’ molecule (which has one transmitting channel), the conductance is given by

$$G = G_0 \mathcal{T}(E_f) = \frac{\Gamma^2}{\mathcal{E}^2 + \Gamma^2} G_0$$

When the molecule is connected to the electrodes with a donor-acceptor bond (or coordinate-covalent bond), as is the case with common linkers such as amine[4, 17], pyridines[14, 22], or methyl sulfides, the electronic coupling is much less than the difference in energy between the conducting orbital and the Fermi energy ($\Gamma \ll \mathcal{E}$) so that $G \approx (\Gamma/\mathcal{E})^2 G_0 \ll 1 G_0$. This establishes limitations on the possibility of finding molecular junctions with unit transmission (thereby minimizing resistive loss), especially when considering the length scale of one to several nanometers.

A single level model is too simple to describe transport through most molecular systems[6]; it is only directly applicable if all other molecular orbitals are sufficiently far away from the Fermi level and no other bond/electrode states interfere. If two molecular orbitals contribute to transmission, such as in a two level (HOMO and LUMO) system, the transmission

function is double Lorentzian (Figure 2.7(b))[23]. In other cases, the d-state of the gold electrode becomes visible in the transmission function[24]. The impact of such features is non-trivial and can vary dramatically when focusing on different systems. By probing both electronic and thermoelectric properties of molecular junctions, we can learn more about the possible forms of the transmission functions of various families of molecules. Results of these studies will be described in the following chapters.

2.4 References

1. Binnig, G. and H. Rohrer, *Scanning tunneling microscopy*. Surface Science, 1983. **126**(1–3): p. 236-244.
2. Kamenetska, M., M. Dellâ€™Angela, J.R. Widawsky, G. Kladnik, A. Verdini, A. Cossaro, D. Cvetko, A. Morgante, and L. Venkataraman, *Structure and Energy Level Alignment of Tetramethyl Benzenediamine on Au(111)*. The Journal of Physical Chemistry C, 2011. **115**(25): p. 12625-12630.
3. Xu, B.Q. and N.J. Tao, *Measurement of single-molecule resistance by repeated formation of molecular junctions*. Science, 2003. **301**(5637): p. 1221-1223.
4. Venkataraman, L., J.E. Klare, I.W. Tam, C. Nuckolls, M.S. Hybertsen, and M.L. Steigerwald, *Single-Molecule Circuits with Well-Defined Molecular Conductance*. Nano Letters, 2006. **6**(3): p. 458 - 462.
5. Widawsky, J.R., M. Kamenetska, J. Klare, C. Nuckolls, M.L. Steigerwald, M.S. Hybertsen, and L. Venkataraman, *Measurement of voltage-dependent electronic transport across amine-linked single-molecular-wire junctions*. Nanotechnology, 2009(43): p. 434009.
6. Widawsky, J.R., P. Darancet, J.B. Neaton, and L. Venkataraman, *Simultaneous Determination of Conductance and Thermopower of Single Molecule Junctions*. Nano Letters, 2012. **12**(1): p. 354-358.
7. Blatt, F.J., *Thermoelectric Power of Metals*. 1976: Plenum Press, New York.
8. Brom, H.E.v.d., A.I. Yanson, and J.M.v. Ruitenbeek, *Characterization of individual conductance steps in metallic quantum point contacts*. Physica B: Condensed Matter, 1998. **252**(1–2): p. 69-75.
9. Agraït, N., J.G. Rodrigo, and S. Vieira, *Conductance steps and quantization in atomic-size contacts*. Physical Review B, 1993. **47**(18): p. 12345.
10. Yanson, A.I., G.R. Bollinger, H.E. van den Brom, N. Agraït, and J.M. van Ruitenbeek, *Formation and manipulation of a metallic wire of single gold atoms*. Nature, 1998. **395**(6704): p. 783-785.
11. Agraït, N., A.L. Yeyati, and J.M. van Ruitenbeek, *Quantum properties of atomic-sized conductors*. Physics Reports, 2003. **377**(2–3): p. 81-279.
12. Ulrich, J., D. Esrail, W. Pontius, L. Venkataraman, D. Millar, and L.H. Doerrer, *Variability of Conductance in Molecular Junctions*. Journal of Physical Chemistry B, 2006. **110**(6): p. 2462-2466.

13. Meisner, J.S., M. Kamenetska, M. Krikorian, M.L. Steigerwald, L. Venkataraman, and C. Nuckolls, *A Single-Molecule Potentiometer*. Nano Letters, 2011. **11**(4): p. 1575-1579.
14. Quek, S.Y., M. Kamenetska, M.L. Steigerwald, H.J. Choi, S.G. Louie, M.S. Hybertsen, J.B. Neaton, and L. Venkataraman, *Mechanically controlled binary conductance switching of a single-molecule junction*. Nature Nanotechnology, 2009. **4**(4): p. 230-234.
15. Martin, C.A., D. Ding, J.K. Sorensen, T. Bjornholm, J.M. van Ruitenbeek, and H.S.J. van der Zant, *Fullerene-based anchoring groups for molecular electronics*. Journal of the American Chemical Society, 2008. **130**(40): p. 13198-13199.
16. Nitzan, A., *Electron transmission through molecules and molecular interfaces*. Annual Review of Physical Chemistry, 2001. **52**: p. 681-750.
17. Hybertsen, M.S., L. Venkataraman, J.E. Klare, A.C. Whalley, M.L. Steigerwald, and C. Nuckolls, *Amine-linked single-molecule circuits: systematic trends across molecular families*. Journal of Physics: Condensed Matter, 2008. **20**(37): p. 374115.
18. Datta, S., *Electronic Transport in Mesoscopic Systems*. 1995: Cambridge University Press.
19. Peskin, U., *An introduction to the formulation of steady-state transport through molecular junctions*. Journal of Physics B: Atomic, Molecular and Optical Physics, 2010. **43**(15): p. 153001.
20. Landauer, R., *Spatial Variation of Currents and Fields Due to Localized Scatterers in Metallic Conduction*. IBM Journal of Research and Development, 1957. **1**(3): p. 223-231.
21. Ashcroft, N.W. and N.D. Mermin, *Solid State Physics*.
22. Kamenetska, M., S.Y. Quek, A.C. Whalley, M.L. Steigerwald, H.J. Choi, S.G. Louie, C. Nuckolls, M.S. Hybertsen, J.B. Neaton, and L. Venkataraman, *Conductance and Geometry of Pyridine-Linked Single-Molecule Junctions*. Journal of the American Chemical Society, 2010. **132**(19): p. 6817-6821.
23. Malen, J.A., P. Doak, K. Baheti, T.D. Tilley, R.A. Segalman, and A. Majumdar, *Identifying the Length Dependence of Orbital Alignment and Contact Coupling in Molecular Heterojunctions*. Nano Letters, 2009. **9**(3): p. 1164-1169.
24. Quek, S.Y., L. Venkataraman, H.J. Choi, S.G. Louie, M.S. Hybertsen, and J.B. Neaton, *Amine-gold linked single-molecule circuits: Experiment and theory*. Nano Letters, 2007. **7**(11): p. 3477-3482.

Chapter 3

The Development of Highly Conducting Junctions

The work described in this chapter was performed in collaboration with synthetic chemists from Prof. Ronald Breslow's group, including Zhan-Ling Cheng, Rachid Skouta, Severin Schneebeli, and Wenbo Chen, and Rebekka Klausen from Prof. Colin Nuckolls's group. Theoretical work was provided by Mark Hybertsen, Hector Vazquez, and Michael Steigerwald. I performed all of the STM measurements and data analysis.

The development of molecular-scale electronics hinges on understanding the charge transport properties of single molecules. A molecular junction consists of a molecule bound between two electrodes via terminal functional groups that link the molecule both electronically and mechanically. The measured conductance of the trapped molecule depends not only on nature of the molecular backbone, but also on the choices of the electrode metal and the chemical link group. All of these together control both the junction's mechanical stability as well as its observable electronic properties. Several single molecule junction experiments have been performed in search of a link group that combines the selectivity needed for junction formation with reproducible conductance and mechanical stability over a prolonged period. Attempts to build stable single molecule junctions include using diphenylphosphine terminal groups[1], frustrating the rotation of methyl-sulfide linkers[2], and attempting to directly attach molecular chalcogenide clusters to the electrodes[3].

We took a large step forward when we found that we were able to use *in situ* chemistry to directly attach the carbon-based molecular backbone to the leads. This is done with trimethylstannyll end groups, which cleave off to allow the formation of covalent Au-C bonds. We generally saw that, when compared to other linkers that use donor-acceptor bonds, the covalent bond dramatically reduced the junction contact resistance. These results were highlighted in a Chemical & Engineering News review[4].

In this chapter, we report the conductances of alkanes and polyphenyls when directly attached to gold electrodes and study the effect of the Au-C bond on transmission with DFT studies. We also investigate conduction across silanes and compare them to several families of organic molecules.

3.1 *In situ* Formation of Highly Conducting Covalent Au–C Contacts for Single-Molecule Junctions*

Abstract

Charge transport across metal–molecule interfaces has an important role in organic electronics[5]. Typically, chemical link groups such as thiols[6] or amines[7] are used to bind organic molecules to metal electrodes in single-molecule circuits, with these groups controlling both the physical structure and the electronic coupling at the interface. Direct metal–carbon coupling has been shown through C₆₀, benzene and π -stacked benzene[8-11], but ideally the carbon backbone of the molecule should be covalently bonded to the electrode without intervening link groups. Here, we demonstrate a method to create junctions with such contacts. Trimethyl tin (SnMe₃)-terminated polymethylene chains are used to form single-molecule junctions with a break-junction technique[6, 7]. Gold atoms at the electrode displace the SnMe₃ linkers, leading to the formation of direct Au–C bonded single-molecule junctions with a conductance that is ~100 times larger than analogous alkanes with most other terminations. The conductance of these Au–C bonded alkanes decreases exponentially with molecular length, with a decay constant of 0.97 per methylene, consistent with a non-resonant transport mechanism. Control experiments and *ab initio* calculations show that high conductances are achieved because a covalent Au–C sigma (σ) bond is formed. This offers a new method for making reproducible and highly conducting metal–organic contacts.

In this work, we synthesize a series of SnMe₃-terminated polymethylene chains with 4–12 carbons in the backbone, and measure the conductance of single-molecule junctions formed from these molecules using a scanning tunneling microscope (STM)-based break-junction method[6, 7]. We show that these junctions have a conductance that is significantly higher than those formed with conventional linkers such as thiols[6] and amines[7]. For example, with 1,4-bis-trimethylstannylbutane we form a single-molecule junction with a conductance that is about one-tenth of the quantum of conductance $G_0 = 2e^2/h$ (where e is the electron charge and h is Planck's constant). This conductance is ~100 times larger than that achieved with 1,4-diaminobutane[7]. The high conductance we observe suggests strongly that the SnMe₃ groups

* Z-L Cheng, R. Skouta, H. Vazquez, J. R. Widawsky, S. Schneebeli, W. Chen, M. S. Hybertsen, R. Breslow, and L. Venkataraman, **Nature Nanotechnology** 6, 353-357, (2011)

are cleaved *in situ*, leading to the formation of covalent Au–C bonds (Figure 3.1(a)). Although other explanations (such as C–Sn–Au bonds; see below) are possible in principle, compelling evidence for direct Au–C sigma (σ) bond formation comes from the fact that the conductance of two control molecules that contain covalent Au–C bonds (1,6-bis-(triphenylphosphinylauryl)hexane (**C6Au**) and 1,8-bis-(triphenylphosphinylauryl)octane (**C8Au**)) are the same as those of the respective SnMe₃-terminated alkanes[12]. Finally, calculations using density functional theory (DFT) show that formation of a direct, covalent Au–C bond is energetically favorable and results in a high zero-bias conductance.

Single-molecule junctions were created by repeatedly forming and breaking Au point contacts[6] with a modified STM (Figure 3.1(a)) in a 10 mM 1,2,4-trichlorobenzene solution of the target molecules. Conductance (current/voltage) was measured as a function of the relative tip/sample displacement to yield conductance traces, which were used to generate conductance histograms. The SnMe₃-terminated alkanes used in this study were prepared by coupling the corresponding di-Grignard reagents with SnMe₃Cl following known procedures taken from the literature[13].

Figure 3.1(b) compares individual conductance traces from measurements of butane, hexane, octane and decane molecules terminated on both ends with SnMe₃ linkers (**C4**, **C6**, **C8** and **C10**, respectively). We see clear conductance plateaus at molecule-dependent conductance values below G_0 that are due to conduction through a molecule bonded in the gap between the two Au point contacts. The position of the conductance plateaus is $\sim 0.09G_0$ for **C4**, and decreases by about an order of magnitude for every two carbons added to the molecular backbone. Furthermore, sample traces show that the plateau length increases with molecule length, as has been observed for other linkers[14, 15]. For the longer molecules, we also see

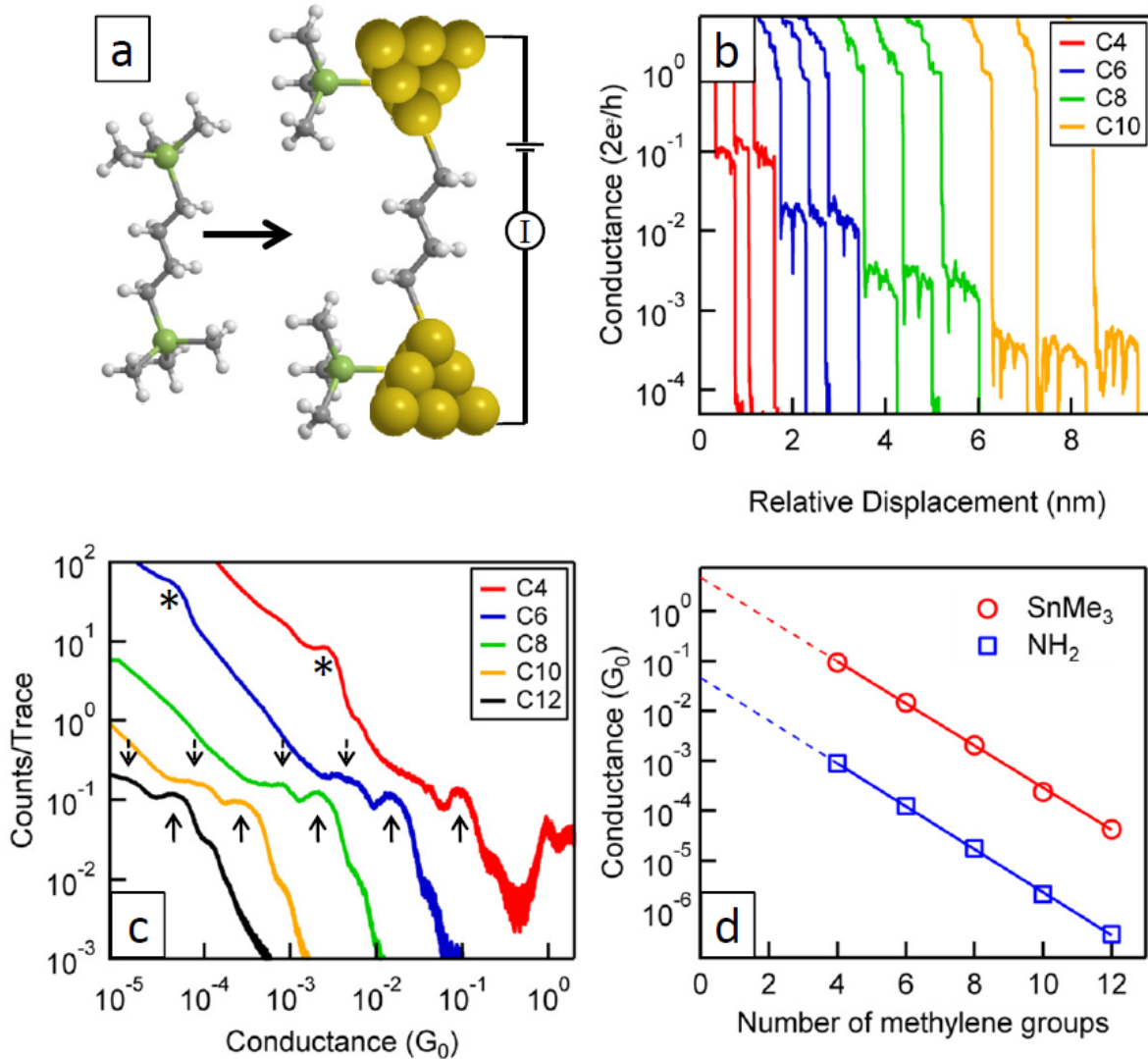


Figure 3.1: (a) Junction formation and conductance measurements with 1,4-bis(trimethylstanny)butane molecules between gold electrodes. (H atoms, white; C atoms, grey; Sn, green). (b) Sample traces showing conductance (on a logarithmic scale) versus relative displacement for SnMe₃-terminated alkanes with four (**C4**: red), six (**C6**: blue), eight (**C8**: green) and ten (**C10**: yellow) methylene groups in the backbone. (c) Conductance histograms for **C4**, **C6**, **C8**, **C10** and **C12**. Each histogram is constructed from 10,000 traces and is generated without any data selection. Bin size is $10^{-4} G_0$ for **C4**, $10^{-5} G_0$ for **C6** and **C8**, $10^{-6} G_0$ for **C10** and $10^{-7} G_0$ for **C12**. Upward arrows indicate primary conductance peaks; downward arrows indicate lower conducting shoulders; asterisks indicate conductance peaks due to the dimer molecule formed *in situ*. (d) Conductance at the peak (as determined by fitting a Lorentzian to the histograms) on a logarithmic scale versus number of methylene groups in the backbone for SnMe₃-terminated alkanes (red) and analogous diamine-terminated alkanes (blue).

sharp dips within the conductance plateau, separated by about 2 Å. We will discuss these features later.

Repeated measurements give a statistical assessment of the junction properties. Figure 3.1(c) presents conductance histograms, generated without any data selection from over 10,000 measurements for each of the five alkanes studied (**C4–C12**). Each conductance histogram reveals a clear peak at a conductance value that decreases exponentially with molecule length. The positions of these peaks are shown in Figure 3.1(d), together with conductance measurements of the same linear alkanes terminated at both ends with amine linkers[16].

We find that conductance G decays as $G \approx e^{-\beta N}$ where $\beta = 0.97 \pm 0.02$ is the decay constant and N is the number of methylene groups on the backbone; this value of β is equivalently to a decay constant of 0.76 per Å using a C–C vertical separation of 1.27 Å. This β value is comparable to that of alkanedithiols (0.8 per Å in refs [6, 17, 18]) or alkanediamines[19] (0.79 per Å in Figure 3.1(d)), indicating that the mechanism for electron transfer across these alkane junctions is by means of non-resonant tunneling or super-exchange[20]. Thus, in these single-molecule junctions, we measure transport characteristics of the molecular backbone—tunneling through the σ -system for alkanes—while achieving a very high coupling across the molecule–metal interface. Extending the fit in Figure 3.1(d) towards the origin shows that we would achieve a G_0 conductance with a backbone of 1–2 carbons, implying that the transport mechanism will change from non-resonant to resonant at this length. This view is supported by the calculations discussed in the following.

In addition to the main peaks discussed above, we see additional peaks for **C4** and **C6** at conductance values that correspond to the main peaks for **C8** and **C12**, respectively (indicated by asterisks in Figure 3.1(c)). There are, therefore, a statistically significant number of junctions formed with conductance plateaus corresponding to the molecule that has twice the number of backbone carbons, which must be formed *in situ*. From analyzing over 10,000 traces measured

with a 10 mM solution of **C4**, we see that ~50% of traces show plateaus at the conductance value for **C8**. As a comparison, ~60% of the traces measured with a 10 mM solution of **C8** show plateaus at the conductance value corresponding to **C8**, but no conductance peak is seen if the **C8** solution is diluted to a concentration of 1 mM or lower. A similar analysis of the measurements carried out in a ~10 mM solution of **C6** shows that 85% of the traces have a step at the **C12** conductance value compared with measurements in a **C12** solution, where nearly 100% of the measured traces show a conductance plateau corresponding to **C12**.

Because we see a large number of traces with conductance plateaus of alkanes twice as long as those prepared synthetically, *in situ* dimerization of the carbon backbones must be occurring. This could only result if the C–SnMe₃ bond was cleaved during measurements. The Grignard reaction that we use for synthesis could also yield longer alkanes, but nuclear magnetic resonance (NMR) analysis of the synthesized compounds shows that we could have only trace quantities (<1%). Such small quantities, corresponding to concentrations of 0.1 mM or less, do not yield a peak in the conductance histograms. These results confirm that we are measuring transport through a Au–(CH₂)_n–Au junction rather than through Au–SnMe₃–(CH₂)_n–SnMe₃–Au, because in the latter case, the ‘dimer’ molecular junction (Au–SnMe₃–(CH₂)_n–SnMe₃–SnMe₃–(CH₂)_n–SnMe₃–Au) would have a different conductance when compared with the molecular junction with twice the number of backbone carbon atoms (Au–SnMe₃–(CH₂)_{2n}–SnMe₃–Au). These results also support the idea that molecules could be bound on one side to the gold surface and can dimerize, making new C–C bonds before bridging the break-junction gap. Although the exact mechanism for dimerization cannot be determined from these measurements, dimerization could occur through a reductive elimination mechanism[21].

Histograms in Figure 3.1(c) also show a small shoulder at a conductance value below that of the main peak for all compounds other than **C4**, as indicated by the downward-pointing (dashed) arrows. The values of the conductance for these broad shoulders correspond to the values observed in the sharp dips seen, for example, in the individual conductance traces shown in Figure 3.1(b). This indicates that during junction formation and elongation, the conductance value can drop as a result of structural rearrangement within the junction. The fact that these dips occur with a separation of ~2–2.5 Å in traces with longer plateaus (see Appendix section A.1 for details) suggests that junction rearrangement involving gold periodicity is involved[22]. Finally, the lack of such dips for **C4** could indicate that for this molecule, where plateau lengths are shortest, junction structures do not allow for reorganization of the molecular attachment point on the electrode[14].

To provide conclusive experimental evidence that we do indeed measure the conductance of Au–C coupled single-molecule junctions, we measured transport through two molecules, **C6Au** and **C8Au**, which, by design, have a Au–C bond built into the structure (Figure 3.2(a), inset). These were made by reacting the corresponding di-Grignard reagents with triphenylphosphine (PPh_3) gold bromide and were stored under argon until just before measurement because of their limited air stability[23]. Figure 3.2(a) shows conductance histograms for these and for **C6** and **C8**. We can see that the peaks are at precisely the same location, irrespective of the terminal group. Moreover, for these control molecules, we do not see a peak corresponding to the dimer molecule or the shoulder at lower conductance. As the **C6Au** and **C8Au** molecules have a direct Au–C link by design[1, 14], these control measurements show that in the case of the SnMe_3 -terminated alkanes, Au–C coupled single-molecule junctions are formed. However, these conductance measurements alone are not sufficient to determine

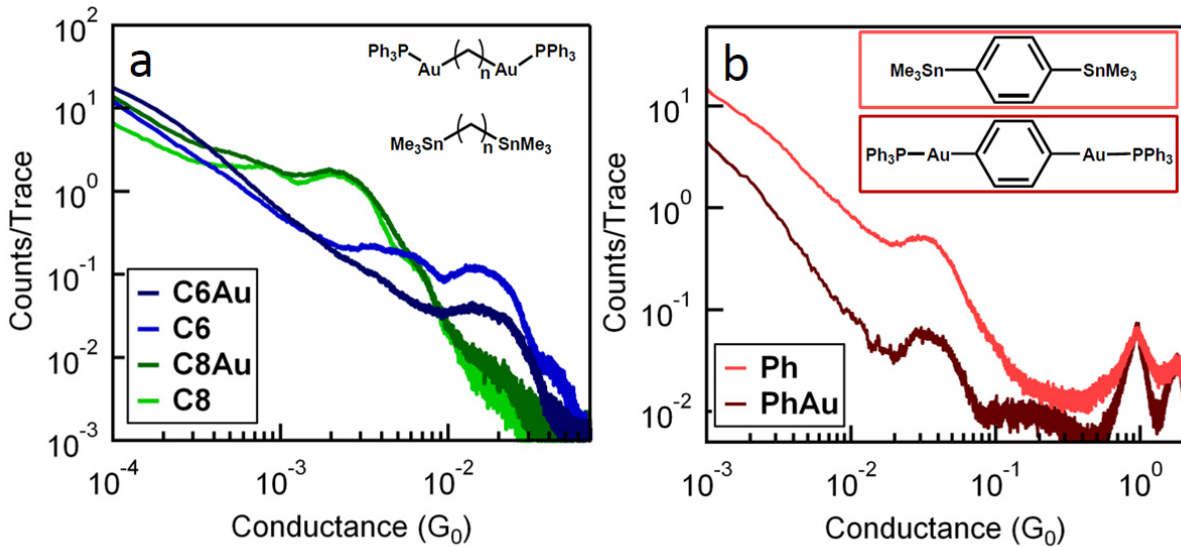


Figure 3.2: (a) Conductance histograms for two SnMe_3 -terminated alkanes (**C6** and **C8**) and two Au-PPh_3 -terminated alkanes (**C6Au** and **C8Au**). Bin size is $10^{-5} G_0$. Inset: structures for SnMe_3 -terminated alkanes (bottom) and Au-PPh_3 -terminated alkanes (top) with $n = 6$ or 8. (b) Conductance histograms for SnMe_3 -terminated benzene (**Ph**) and Au-PPh_3 -terminated benzene (**PhAu**). Bin size is $10^{-4} G_0$. Inset: structures for **Ph** (top) and **PhAu** (bottom).

whether the PPh_3 capping ligand remains bonded locally to the Au link atom or is removed when the junction forms.

To probe transport through a Au–C coupled conjugated molecule, we synthesized 1,4-bis(trimethylstannyl)benzene (**Ph**) and 1,4-bis-(triphenylphosphinylauryl)benzene (**PhAu**) (Figure 3.2(b), inset)[12]. Conductance measurements of **Ph** and **PhAu** were carried out as described above for the alkanes. For **Ph**, we had to wait about 2.5 h after adding the ~10 mM solution of the compound in 1,2,4-trichlorobenzene before conductance traces demonstrated molecular plateaus, indicating that a chemical transformation was occurring before the conducting molecule was formed. We deduce that the Sn–C link is transformed to a Au–C link during this waiting period while the solution is in contact with the gold electrodes. This result also indicates that breaking the C– SnMe_3 bond is harder with the sp^2 benzene carbon than with the sp^3 carbons of the alkanes. For measurements with **PhAu**, conductance plateaus were observed as soon as the measurement started (unlike with **Ph**), as we saw with the alkane–Sn

compounds. In Figure 3.2(b), it can be seen that conductance histograms show a peak around $0.03G_0$ for both **Ph** and **PhAu**. It is noteworthy that the conductance of these benzene derivatives is not very high; **C4** conducts better than a benzene connected directly to Au electrodes[24], in contrast to what is observed with other linkers[7]. This is because the Au atoms are not well coupled to the benzene π system in these molecules, and mainly conduct through the sp^2 linked σ system.

To understand the energetics, physical structure and conductance for the junctions formed in these experiments, we carried out DFT-based, first-principles calculations with a gradient-corrected exchange-correlation functional[25]. We first probed the initial C–SnMe₃ bond scission by calculating the energy required to break the C–Sn bond for an isolated molecule[26]. We found the energy required to break the backbone C–SnMe₃ bond is ~0.3 eV lower than that required to break the Sn–CH₃ bond. This clearly favors direct binding of the C backbone to the gold tip over a scenario in which a single Me group is removed and a Sn–Au bond forms. We then analyzed the binding of the resultant products to model the gold electrodes, which were represented by multilayer slabs and a small, localized structure of Au atoms to represent the tips of the electrodes[27]. For this purpose, we used a shorter example, trimethylethyltin (C₂H₅SnMe₃) and considered several sites on an Au surface with a four- or six-atom model tip structure.

Two scenarios were compared, as shown in Figure 3.3(a) and Figure 3.3(b). For cleavage at the C–SnMe₃ bond, the SnMe₃ group binds to different Au motifs, including an atop, hollow and bridge site on a flat Au surface, as well as to an apex atom on our tip structure. However, the C₂H₅ part binds only to an undercoordinated gold atom of our tip structure or to the atop site on the Au surface. The energy gained from breaking the C–SnMe₃ bond and forming a Au–C bond

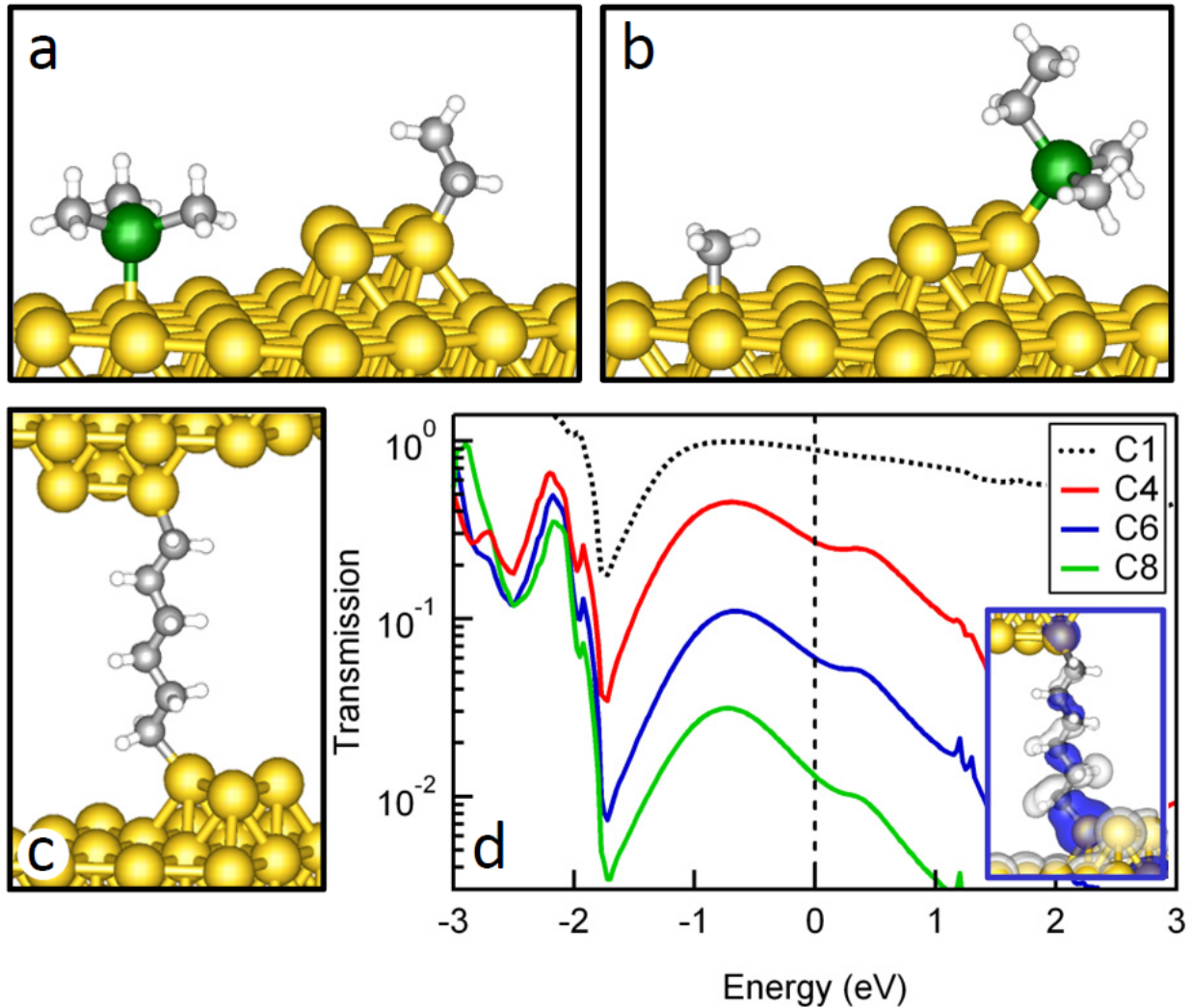


Figure 3.3: (a) Sample geometry used to determine the energy required to first cleave a C–SnMe₃ bond and then bond the SnMe₃ to the Au(111) surface and the C₂H₅ to a model electrode structure. (b) Sample geometry used to determine the energy required to first cleave the Sn–CH₃ bond and then bond the CH₃ to the Au(111) surface and the SnMe₂C₂H₅ to a model electrode structure. (c) Sample geometry used in transmission calculations for **C6**. (d) Transmission (on a logarithmic scale) versus energy (relative to the Fermi energy) for **C1** (dashed back line), **C4** (red), **C6** (blue) and **C8** (green) junctions. Inset: molecular scattering state at the Fermi energy showing σ character.

on the tip and a Au–SnMe₃ bond on the surface was found to be ~0.8 eV, and varied by ~0.05 eV depending on the location of the SnMe₃ group. In contrast, for cleavage of the Sn–CH₃ bond, the resultant methyl bonds either to an apex atom on the tip structure (energy gain, 0.6 eV) or atop on the flat Au surface (energy gain, 0.3 eV; Figure 3.3(b)). Although these energies do not provide details of the reaction path or transition barriers for rupturing the Sn–C bond and

forming an Au–C and Au–Sn bond, they do show that the formation of an Au–C coupled single-molecule junction in the final state is favored energetically and entropically. Finally, we find that the energy required to rupture the Au–C bond in a **C6** junction bonded to a single gold atom as a model of the electrode is 3.0 eV, which is substantially higher than the associative bond formed between gold and benzene[10, 11] or the links that form donor–acceptor bonds to gold[14, 16, 19].

We used a non-equilibrium Green function approach[28] to calculate electronic transmission through junctions formed between gold electrodes and alkane backbones, as illustrated in Figure 3.3(c). Transmission curves for three alkanes used in the experiments, **C4**, **C6** and **C8**, as well as for **C1**, are shown in Figure 3.3(d). Transmission at the Fermi level results primarily from the σ channel, as shown by the transmission channel for **C6** in the inset of Figure 3.3(d). The conductance is dominated by the occupied resonance that is physically derived from the Au–C σ -bond orbitals. These transmission curves have not been corrected for the inherent errors of DFT, so calculated conductance values are larger than those in the experiment, as typically found for other junctions[29-33]. For more quantitative comparison to experiment, the resonance positions are shifted to account for intramolecular self-energy effects as well as the image potential in the junction with a simplified procedure that corrects the conductance[29]. The corrected conductance at zero bias is $0.12G_0$, $0.02G_0$ and $0.004 G_0$ for **C4**, **C6** and **C8**, respectively, falling within the conductance peak of the experiments. The computed decay constant β for **C4**, **C6** and **C8** is 0.86 per methylene group, somewhat smaller than that measured, but still indicative of non-resonant tunneling. Calculations for **Ph** were also carried out. We find that transmission near the Fermi energy is dominated by the σ channel, consistent with the low conductance measured and in agreement with recent calculations[34].

Finally, we return to the trends in conductance seen for **C4–C12**. The exponential decay indicates that the conductance mechanism occurs by means of non-resonant tunneling. Given the direct Au–C bond link to the electrode, the high conductance found here is due in part to the tunneling path being shorter (no intervening link groups). Even taking this into account, and comparing, for example, **C6** with 1,4-diaminobutane, we find that the conductance for direct Au–C coupled junctions is a factor of 10 higher. The calculations show that electronic coupling is mediated by a broad resonance due to the Au–C σ -bond orbitals, which is relatively close to the Fermi energy, resulting in high electronic coupling at the interface. Extrapolating to the limit of a backbone with a single CH₂ group, the electronic coupling through that single unit is large enough that the calculated transmission for **C1** shows near unit transmission over an extended energy range (Figure 3.3(d)). A cross-over from through bond tunneling to single-channel resonant transmission should therefore occur at a backbone length between **C1** and **C4**. Unfortunately, attempts at synthesizing these shorter alkanes were not successful. Focusing on the contribution of the link groups, the high measured conductance and the calculations suggest that the contact resistance has a value that is close to the minimum value ($1/G_0$) dictated by fundamental quantum mechanics for a single conducting channel.

In conclusion, we have created a class of single-molecule junctions that exhibit well-defined structure and high conductance. Starting with organo–tin compounds, *in situ* reactions result in junction formation where the Au electrodes are covalently bonded directly to the C backbone without an intervening link group. For these single-molecule junctions, the conductance depends on the molecular backbone, allowing molecule-dependent, selective highly conducting linkers for single-molecule junctions.

Acknowledgements

This work was supported primarily by the Nanoscale Science and Engineering Initiative of the National Science Foundation (NSF; CHE-0641523), the New York State Office of Science, Technology, and Academic Research (NYSTAR) and an NSF Career Award to L.V. (CHE-07-44185). This work was carried out in part at the Center for Functional Nanomaterials, Brookhaven National Laboratory, which is supported by the Office of Basic Energy Sciences of the US Department of Energy (DOE; DE-AC02-98CH10886). This work was also supported in part by the DOE Energy Frontier Research Centers programme (EFRC; DE-SC0001085).

3.2 Highly Conducting π -Conjugated Molecular Junctions Covalently Bonded to Gold Electrodes*

Abstract

We measure electronic conductance through single conjugated molecules bonded to Au metal electrodes with direct Au–C covalent bonds using the scanning tunneling microscope based break-junction technique. We start with molecules terminated with trimethyltin end groups that cleave off *in situ*, resulting in formation of a direct covalent σ bond between the carbon backbone and the gold metal electrodes. The molecular carbon backbone used in this study consist of a conjugated π system that has one terminal methylene group on each end, which bonds to the electrodes, achieving large electronic coupling of the electrodes to the π system. The junctions formed with the prototypical example of 1,4-dimethylenebenzene show a conductance approaching one conductance quantum ($G_0 = 2e^2/h$). Junctions formed with methylene-terminated oligophenyls with two to four phenyl units show a 100-fold increase in conductance compared with junctions formed with amine-linked oligophenyls. The conduction mechanism for these longer oligophenyls is tunneling, as they exhibit an exponential dependence of conductance on oligomer length. In addition, density functional theory based calculations for the Au–xylylene–Au junction show near-resonant transmission, with a crossover to tunneling for the longer oligomers.

It is a great challenge to achieve electronically transparent connections between metal electrodes and organic molecules[5], so as to minimize resistance introduced by the chemical linkers normally used to form such interfaces[7, 8, 10, 11, 19, 35-38]. Typically, thiols[6, 36, 39, 40] that bind covalently to gold, or amines[7, 36, 41] that form donor–acceptor bonds to under-coordinated gold, are used to electronically couple organic backbones to metal electrodes. For each link group, analysis of a series of single-molecule junctions as a function of length has generally revealed a large contact resistance, significantly larger than the ideal limit for a single channel of one conductance quantum ($G_0 = 2e^2/h$)[7, 19, 42]. A junction with conductance close to G_0 has been demonstrated for H₂ and benzene molecules with platinum electrodes under high-

* W. Chen, J. R. Widawsky, H. Vázquez, S. T. Schneebeli, M. S. Hybertsen, R. Breslow, and L. Venkataraman, **J. Am. Chem. Soc.** 133, 17160–17163 (2011)

vacuum conditions at low temperatures[8, 43]. However, the ability to create and control transport through highly conducting molecular–metal interfaces remains a major challenge, especially under ambient conditions.

We have shown previously that direct Au–C covalent σ bonds can be created *in situ* at the molecule–gold interface, resulting in highly conducting σ -bonded systems[43]. For example, a conductance of $0.1 G_0$ through a butane backbone was demonstrated. These direct Au–C bonded molecular junctions were created starting with trimethyltin-terminated alkanes. The trimethyltin end-groups cleaved off *in situ*, yielding direct Au–C bond coupled junctions. Our density functional theory (DFT)-based calculations showed that, in the limit of a single methylene group, a conductance approaching G_0 could be achieved, suggesting that the direct Au–C link has near-ideal transmission characteristics. While we succeeded in forming junctions with benzene, the conductance was relatively low, consistent with calculations indicating conduction occurred through the σ system[34, 43].

Here, we create single-molecule junctions using conjugated backbones terminated with methylene groups that bind covalently to gold metal electrodes, again through the use of SnMe_3 groups that cleave off *in situ*. We find that the resulting junctions have a conductance that is 100-fold higher than those of similar junctions formed with conventional linkers[44]. These junctions are highly conducting because the Au–C bonds to the terminal methylene units are well coupled to the conjugated π system. This is in contrast to similar junctions created previously, where Au was bound directly to a carbon on the benzene ring[43]. Specifically, we find that the conductance of *p*-xylylene bonded to gold electrodes approaches $1 G_0$. Our theoretical calculations show that conductance occurs via near-resonant transmission. For longer

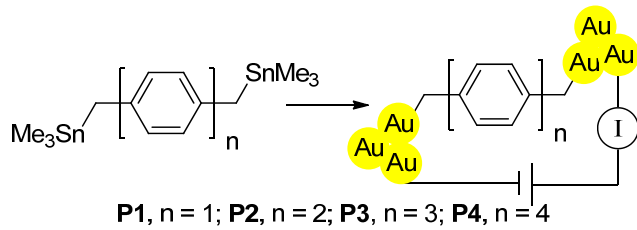


Figure 3.4: *In situ* formation of direct Au–electrode–C bonds starting from SnMe_3 precursors.

polyphenyls with 2–4 phenyl units, we find that the conductance decreases exponentially with increasing length, with a characteristic decay constant of 1.9/phenyl group.

We synthesized a series of trimethylstannylmethyl-terminated polyphenyls and measured the conductance of single-molecule junctions formed from these molecules using the scanning tunneling microscope based break-junction (STM-BJ) method (Figure 3.4)[6, 7]. In this technique, single-molecule junctions are created by repeatedly forming and breaking Au point contacts[6] in a ~10 mM 1,2,4-trichlorobenzene solution of the target trimethyltin-terminated molecules. Conductance (current/voltage) is measured as a function of the relative tip/sample displacement to yield conductance traces, which are used to generate conductance histograms. We synthesized 1,4-trimethylstannyl-terminated xylylene using two different methods. In one, we converted 1,4-bis-bromomethylbenzene (*p*-xylylene dibromide) to the dilithio compound and reacted it with trimethylstannyl chloride[45]. In the other method, we reacted the *p*-xylylene dibromide with trimethylstannyl lithium[46, 47] The latter procedure was used to attach the trimethylstannyl groups for the polyphenyl compounds. *We note here that these compounds are toxic and should be handled with care.*

Figure 3.5(a) compares individual conductance traces from measurements of solutions of stannylylated 1,4-dimethylenebenzene, 4,4'-dimethylenebiphenyl, 4,4''-dimethylene-*p*-terphenyl, and 4,4'''-dimethylene-*p*-tetraphenyl (**P1**, **P2**, **P3**, and **P4**, respectively). We see clear

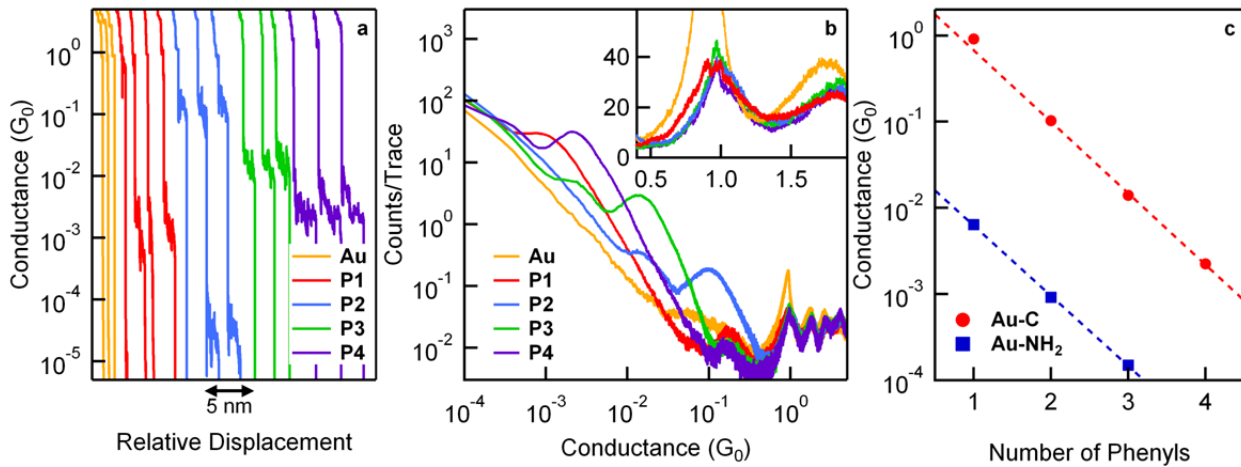


Figure 3.5: (a) Individual conductance traces measured in solutions of the SnMe₃-terminated polyphenyl compounds **P1–P4**. Measurements in solvent alone are also shown for comparison (Au). The applied bias is 250 mV. (b) Conductance histograms of over 10,000 traces generated with linear bin size of 0.0001 G_0 , shown on a log–log scale. Inset: the same data on a linear scale. (c) Conductance versus number of phenylene units in the chain for **P1–P4**, and analogous measurements with the related amine-terminated series. Dotted lines represent linear least-squares fit to **P2–P4** series. Note the point for **P1** above the line.

conductance plateaus at molecule-dependent conductance values, although in the case of **P1** it is not straightforward to distinguish the molecular plateau from that of the single-atom contact at a conductance around G_0 . These plateaus are due to conduction through a molecule bonded in the gap between the two Au point-contacts. These conductance plateaus are seen in the measurements immediately after a solution of the target molecule terminated with SnMe₃ groups is added, in contrast with measurements of 1,4-bis(trimethylstannyl)benzene[43], where conductance plateaus were seen in measurements only after 2.5 h. This delay seen in measurements of 1,4-bis(trimethylstannyl)-benzene indicated that conduction did not occur through trimethylstannyI terminated molecules. In our past work[43], this was confirmed by showing that the conductance of auryltriphenylphosphine terminated compounds were the same as those terminated by SnMe₃ groups.

In addition to plateaus seen at a high conductance, the traces in Figure 3.5(a) show a second series of plateaus at 0.001 G_0 for **P1** (red) and 3×10^{-5} G_0 for **P2** (blue). These are

attributed to *in situ* dimerization of the target compounds after the SnMe₃ linkers have been lost on the gold electrodes, in which the conjugated systems are linked by a dimethylene bridge. Indeed, some traces show two plateaus, one due to the monomer and one from the dimer. However, we cannot determine, on the basis of conductance alone, whether both are present during the entire measurement. We will return to these features later in this section.

Repeated measurements give a statistical assessment of the junction properties. In Figure 3.5(b), we show conductance histograms for each of the compounds studied here. Each conductance histogram, generated from over 10,000 traces without any data selection, reveals clear peaks at conductance values that depend on the molecular backbone. The inset of Figure 3.5(b) shows the same conductance histograms on a linear scale around 1 G₀. Here, we see a clear peak around 0.9 G₀ for **P1** that can be distinguished from the peak near 1 G₀ that is due to the conductance through a single gold-atom contact. By fitting the peaks in these conductance histograms with Lorentzians, we determine that the conductance of **P1** is about 0.9 G₀, while the values for **P2**, **P3**, and **P4** are 0.1 G₀, 0.014 G₀, and 0.0022 G₀, respectively. The position of the highest conductance peak in each histogram is plotted on a semilog scale against the number of phenyl rings in the molecule in Figure 3.5(c). We find that, for the series **P2**–**P4**, the conductance decays exponentially with increasing number of phenyl groups, with a decay constant $\beta = 1.9/\text{phenyl}$ or $0.43/\text{\AA}$. For comparison, in Figure 3.5(c), we also plot the conductance of polyphenyls doubly terminated with amine linkers, which show a similar decay in conductance with length[16].

The histogram for **P1**, in Figure 3.5(b), also shows a peak around 0.001 G₀ due to the presence of dimer molecules formed *in situ* during the measurement. To show that this is indeed due to conduction through a dimer molecule, we synthesized the ditin precursor of *p*-xylylene

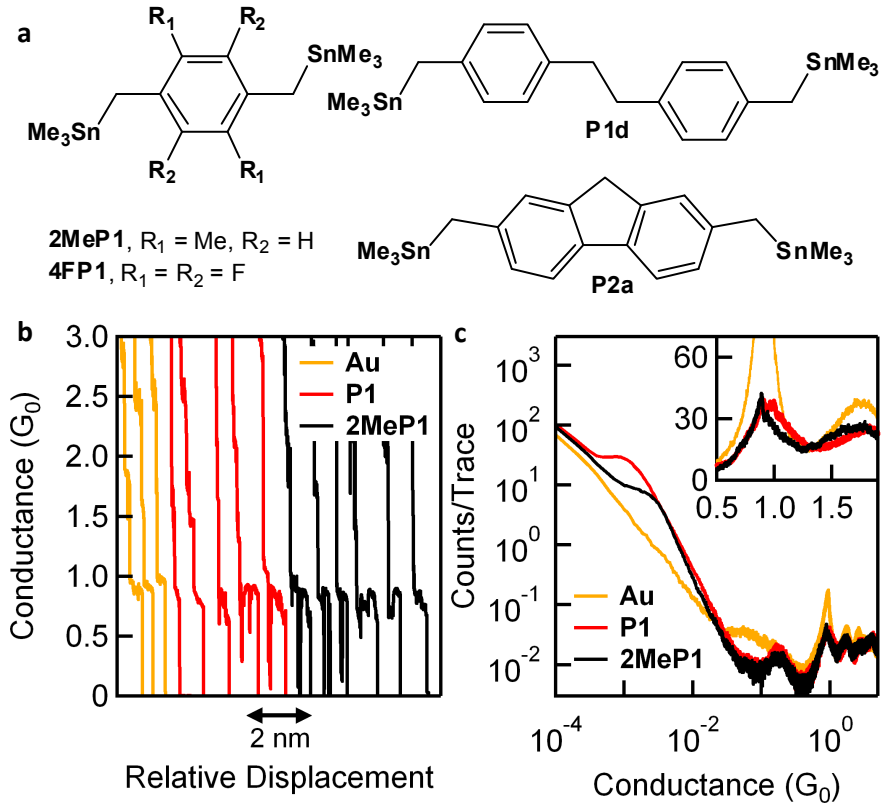


Figure 3.6: (a) Structures of additional compounds studied. (b) Individual conductance traces measured in solutions of the SnMe_3 -terminated compounds **P1** (red) and **2MeP1** (black) at 25 mV applied bias. (c) Conductance histograms of over 10 000 individual measurements, generated with linear bin size of 0.0001 G_0 , shown on a log–log scale. Inset: same histograms on a linear scale.

dimer (**P1d**, see Figure 3.6(a)) and measured its conductance in the STM-BJ setup. The conductance histogram for **P1d** shows a clear peak at $0.001 G_0$ but no feature other than the gold conductance peak at $1 G_0$ (Appendix Figure A.3(a)). This clearly demonstrates that the dimer molecule **P1d** is created *in situ* when measurements of **P1SnMe₃** are carried out. That the conductance of the dimer is almost 3 orders of magnitude lower than that of the monomer can be attributed to the saturated dimethylene bridge between the two conjugated parts.

We also synthesized and measured the conductance of two xylylene derivatives with trimethyltin terminations. The first is a dimethyl-substituted xylylene (**2MeP1**), and the second is a tetrafluoro-substituted xylylene (**4FP1**) (Figure 3.6(a)). For **2MeP1**, we see a conductance peak at $\sim 0.9 G_0$, very close to that of the unsubstituted **P1**, as shown in Figure 3.6(c). The fact that the

methyl substituents do not affect conductance significantly is consistent with a near-resonant transport mechanism, as will be discussed further below. Thus for both **P1** and **2MeP1**, we demonstrate near-resonance transport across a molecular junction 0.8 nm in length.

The histogram for **2MeP1** in Figure 3.6(c) also shows a second peak around $0.002 G_0$, due to the formation of the dimer molecule, as in the case of **P1**. However, here we see a change in the conductance of the **P1** dimer when compared with that of the **2MeP1** dimer, as we expect when the mechanism for transport involves tunneling through the saturated ethano group. In contrast to the results with **2MeP1**, we find that **4FP1** does not show clear evidence for junction formation. The conductance histogram generated from 10 000 measurements does not show two clear peaks around G_0 or a peak due to the molecular dimer formed *in situ* (Appendix Figure A.3(b)). We attribute this to a stronger Sn–C bond in **4FP1SnMe₃**, making *in situ* cleavage of the SnMe₃ group more difficult.

In our past work with Au–C coupled alkanes and benzene [43], we found that the conductance of 1,4-didehydrobenzene covalently bonded to Au electrodes was only $0.03 G_0$, significantly lower than that of *p*-xylylene. For benzene, only the molecular σ system, which is a rather poor conductor, was well coupled through the Au–C bonds[34, 43]. In contrast, with xylylene the Au–C bonds are very well coupled to the π system, yielding the high conductances observed. In principle, this coupling will depend on the angle between the Au–C bond and the phenyl plane and will be maximum when this angle is 90° [2]. On the basis of calculations for this system, we find indeed that the minimum energy configuration has a 90° angle, and the barrier for rotation is 10.4 kcal/mol, or 0.45 eV.

The conductance of **P2**, the biphenyl analogue of **P1**, is $0.10 G_0$ (Figure 3.5(b)). This conductance is a factor of 9 lower than that of **P1**, while in the case of amine-terminated

polyphenyls, the difference between benzene and biphenyl was a factor of only ~ 6 . To see if the difference between **P1** and **P2** is partly due to an anomalous internal twist angle at the central C–C bond, we synthesized a trimethyltin-terminated analogue of fluorene with two methylene groups (**P2a**) and measured its conductance using the STM-BJ setup. We find that **P2a** has a conductance of $0.17 G_0$ (Appendix Figure A.3(c)), but the conductance ratio between **P1** and **P2a** (5.3) is still larger than the ratio for the diamine analogues (4.3)[44]. This indicates that the lower conductance of an Au–**P2**–Au junction compared with that of the Au–**P2a**–Au junction partly reflects a twist in the phenyl–phenyl bond that is absent in the fluorene analogue. However, we see that an Au–**P1**–Au junction still has a higher conductance than one would expect, just extrapolating the exponential dependence seen for the longer polyphenyl compounds investigated here.

To understand the origin of the high conductance observed in these junctions, we carried out DFT-based, first-principles calculations[27] with a gradient-corrected exchange-correlation functional[25] and a nonequilibrium Green's function approach[28] to calculate electronic transmission through these junctions. Transmission curves for **P1**–**P4** junctions are shown in Figure 3.7. The calculated zero-bias conductances are $0.9 G_0$, $0.5 G_0$, $0.15 G_0$, and $0.05 G_0$ for **P1**–**P4**, respectively. Transmission at the Fermi level is derived from the molecular orbitals (MOs) on the Au–C bonds that are very well coupled to the molecular π backbone and to the gold electrodes. For **P1**, this results in two distinct resonances, one for an even combination of the Au–C bond MOs and one for the odd combination, as seen from the isosurface plots of the transmitted scattering state for each resonance (Figure 3.7(a))[48]. Physically, the Au–C bond MOs and the nearby π backbone MOs are nominally fully occupied by electrons. The extent to which the Fermi level for this junction falls within the nearest resonance depends on the amount

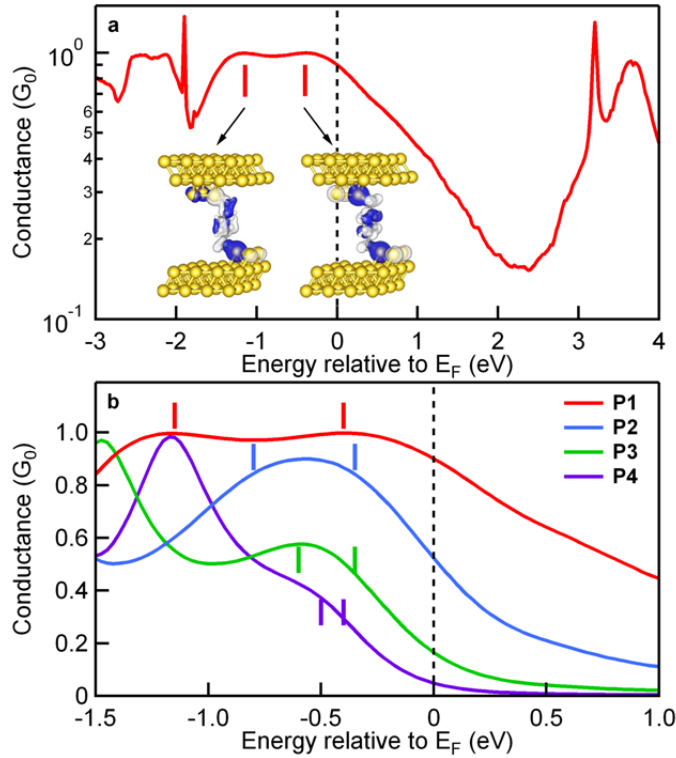


Figure 3.7: (a) Calculated transmission spectrum for **P1** bonded to Au electrodes. Inset: isosurface plots of the real part of the transmitted scattering states for energies at the vertical bars (-1.15 and -0.4 eV), showing the even and odd combinations of the Au–C bonds coupled through the π backbone. (b) Transmission spectra for **P1**–**P4**. Bars indicate the approximate position Au–C MO energies.

of charge transfer from the molecule to the electrodes. An analysis of the Mulliken populations for the **P1** junction shows net positive charge, with the molecule having lost about 0.5 electron. The electrostatic balance leads to the Fermi energy being placed slightly above the highest MO resonance, resulting in conductance of **P1** being near-resonant, with a magnitude close to G_0 .

For the longer derivatives, the effective through- π -system coupling between the Au–C MOs is reduced. The corresponding energy splitting between the even and odd combinations of these MOs also gets smaller, and the two distinct resonances seen for **P1** merge into a single, broad feature at ~ -0.5 eV, with decreased transmission at the peak (Figure 3.7(b)). However, the distinct even and odd combinations of the Au–C MOs can still be clearly seen in the transmitted scattering states. The charge transfer from the molecule to the electrodes is similar to that for **P1**,

and the Fermi level is pinned at an energy just above the highest resonance. The computed decay constant β for **P2–P4** is 1.2/phenyl group.

There are inherent errors in the use of the DFT MOs and energies for transport calculations in nanoscale junctions.[30, 32, 49–53] While the impact is minor for cases where the junction conductance is close to G_0 , e.g., for metal point contacts[54], the calculated conductance values in the tunneling regime for single-molecule junctions are typically larger than those measured in experiment[29, 49, 53, 55, 56]. In the present case, we expect that corrections to the DFT-based theory will only change the **P1** transmission modestly, leaving a resonance with near-unit transmission close to the Fermi energy. However, the DFT-calculated π backbone MO energy is likely too close to the Fermi energy in general, an effect that will be larger for longer oligomers, where screening by the electrodes becomes less effective. In this case, the conductance will be smaller than indicated by the DFT calculations, with an increase in the effective β value for**P2–P4**.

In conclusion, we have demonstrated a clear method to create circuits with strong electronic coupling between gold electrodes and conjugated molecules. We achieve a single-molecule junction conductance close to one quantum across a length of ~ 0.8 nm. This remarkable result opens up new methods to create long and highly conducting molecular junctions.

Acknowledgments

This work was supported in part by the Nanoscale Science and Engineering Initiative of the NSF (award CHE-0641523), the New York State Office of Science, Technology, and Academic Research (NYSTAR), and NSF Career Award CHE-07-44185 (L.V.). J.R.W. was supported by

the EFRC program of the U.S. Department of Energy (DOE) under Award No. DE-SC0001085. S.T.S. was the recipient of a Guthikonda Graduate Chemistry Fellowship. Part of this work was carried out at the Center for Functional Nanomaterials, Brookhaven National Laboratory, which is supported by the DOE Office of Basic Energy Sciences, under contract no. DE-AC02-98CH10886.

3.1 Conductive Molecular Silicon*

Abstract

Bulk silicon, the bedrock of information technology, consists of the deceptively simple electronic structure of just Si–Si σ bonds. Diamond has the same lattice structure as silicon, yet the two materials have dramatically different electronic properties. Here, we report the specific synthesis and electrical characterization of a class of molecules, oligosilanes, that contain strongly interacting Si–Si σ bonds, the essential components of the bulk semiconductor. We use the scanning tunneling microscope based break-junction technique to compare the single molecule conductance of these oligosilanes to alkanes. We find that the molecular conductance decreases exponentially with increasing chain length with a decay constant $\beta = 0.27 \pm 0.01 \text{ \AA}$, comparable to that of a conjugated chain of C=C π -bonds. This result demonstrates the profound implications that σ conjugation has on the conductivity of silicon.

Bulk silicon exclusively contains Si–Si σ bonds; indeed, the material can be imagined as a series of one-dimensional chains of Si-atoms cross-linked in three dimensions. It was first shown in the mid-twentieth century that short chains of Si atoms (oligosilanes) have markedly differently electronic properties relative to their structural analogs, the alkanes[57]. While alkanes do not absorb light above 190 nm, Gilman *et al.* observed that permethyloligosilanes (e.g. hexamethyldisilane and higher oligomers) display strong absorbance in the range of 200–300 nm[58]. In a trend similar to linearly conjugated systems such as oligoenes[59], the position of maximum absorbance (λ_{\max}) and absorption coefficient (ϵ) increases with the length of the Si chain[58, 60]. This observation led to speculation that saturated oligosilanes may undergo electron transfer chemistry similar to conjugated carbon-based materials. Indeed, the pioneering work of West established that the stable delocalized decamethylcyclopentasilane radical anion can be observed by EPR spectroscopy[61] and that linear and cyclic oligosilanes form charge

* R. Klausen, J. R. Widawsky, M. L. Steigerwald, L. Venkataraman, and C. Nuckolls, **J. Am. Chem. Soc.**, 134, 4541–4544, (2012)

transfer complexes with π -acceptors such as tetracyanoethylene (TCNE)[62].

These promising initial experiments inspired considerable interest in the development of polymeric silanes as electronic materials; however, the challenges in silane synthesis ultimately hindered the widespread study of oligo- and polysilanes after the 1980's[63-65]. High molecular weight polymers are obtained via sodium-mediated Wurtz-type coupling of dichlorosilane monomers. The harsh conditions limit the functional group tolerance to relatively inert alkyl and aryl substituents[66] and the resultant polymers also suffer from low yields/wide molecular weight distributions[67]. Herein, we report the synthesis of oligomeric silanes of specific length functionalized with anchor groups, which enable single molecule conductance measurements. We carry out these conductance measurements on a set of SiMe₂ oligomers that are terminated with 4-(methylthio)phenyl groups (Figure 3.1Figure 3.8), which bind to undercoordinated Au to form single molecule junctions with linear silane backbones that are stable under ambient conditions[6, 19, 44].

We synthesize the oligomeric materials via silylation of an aryllithium reagent with a symmetric α,ω -dichlorooligosilane (**5a-e**) (Figure 3.9(a)). α,ω -Dichlorooligosilanes are a known class of molecules and are typically synthesized by chlorination of dodecamethylcyclohexasilane[68-70]. This method yields a complex mixture of chlorosilanes that we found cumbersome. Instead, we employed an iterative synthesis of the α,ω -dichlorooligosilanes (**5c-e**) in which dimethylphenylsilyllithium (**3**)[70-72] is coupled to commercially available dichlorodimethylsilane (**5a**) or dichlorotetramethylsilane (**5b**) to yield α,ω -diphenyloligosilanes (**4a-b**) (Figure 3.9(b)). Protodesilylation with HCl/AlCl₃ yields α,ω -dichlorooligosilanes (**5c-d**) that can then be coupled with the aryl lithiates or with silyllithium **3** to yield pentasilane **4c**[73]. The arylsilylation reaction efficiently yielded the bis(4-

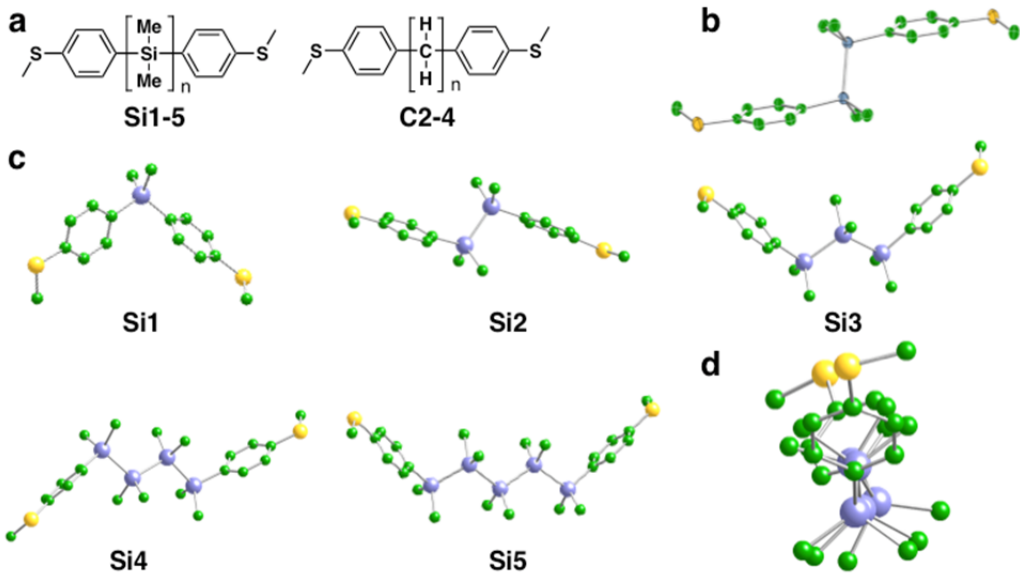


Figure 3.8: (a) Molecular structures of methyl sulfide-capped oligosilanes **Si1–5** and alkanes **C2–4**. (b) ORTEP of a single molecule of silane **Si2**. Ellipsoids are shown at the 50% probability level. (c) B3LYP/6-31G**-calculated lowest-energy structures of oligosilanes **Si1–5**. (d) Perspective drawing of the lowest-energy conformation of pentasilane **Si5**, demonstrating the flexible silicon backbone. In (b–d), H atoms have been omitted for clarity; S is shown in yellow, Si in blue, and C in green.

(methylthio)phenyl)silanes in 60–80% yield. These compounds are air-stable solids that are soluble in common organic solvents including hydrocarbon, aromatic, and chlorinated solvents. The crystal structure of disilane **Si2** (Figure 3.8(b)) confirms that the Si-chain adopts a fully staggered *trans* conformation, which is expected to have the optimal orbital overlap for electronic communication[71, 74]. It is also important to note that there is no detectable decomposition or oxidation during the break junction measurements.

The conductance of these oligosilanes **Si1–5** is measured using a scanning tunneling microscope-based break-junction (STM-BJ) technique[7, 19, 44]. This is carried out using a gold tip and substrate to repeatedly form and break gold point contacts in solutions of the target compounds (1 mM) in 1,2,4-trichlorobenzene. The conductance (current/voltage) is measured across the Au tip/substrate pair as a function of the tip/substrate separation. The conductance

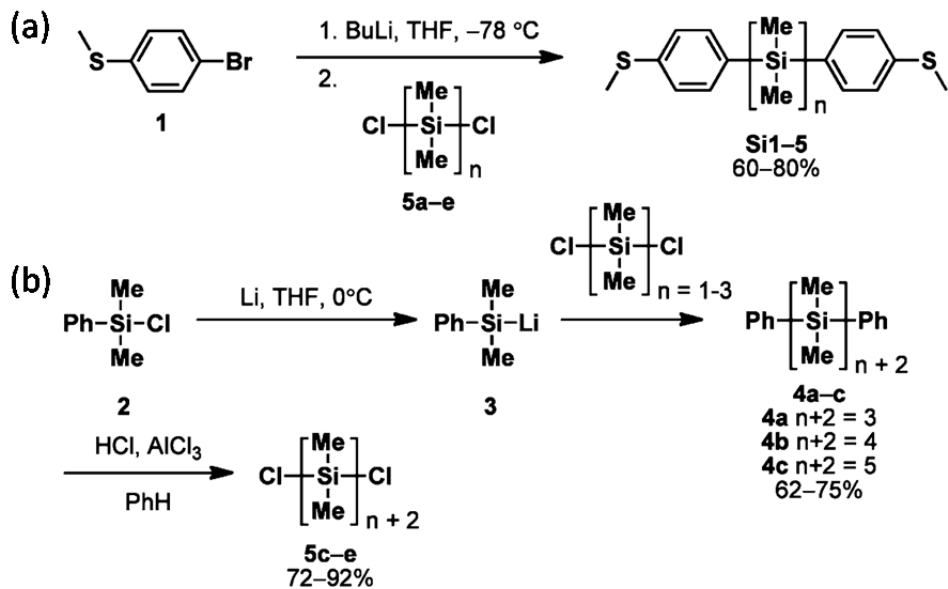


Figure 3.9: Synthetic scheme for α,ω -Bis(4-methylthio)phenyloligosilanes **Si1-5**: (a) Arylsilylation Reaction; (b) Synthesis of α,ω -Dichlorooligosilanes **5c-e**

traces show plateaus at integer multiples of G_0 , the quantum of conductance, which correspond to multiples of Au atoms. At a conductance value below G_0 , a molecule-dependent plateau is observed (Inset, Figure 3.10(a)). Thousands of traces are measured and used to generate two-dimensional conductance-displacement histograms without data selection[75, 76]. Figure 3.10(a) shows such a 2D-histogram measured with **Si1** generated with 27,000 traces (two-dimensional histograms for other compounds are shown in the SI). We see an intense peak around $10^{-4} G_0$, which extends approximately 0.5 nm indicating that single molecule junctions are formed reproducibly with this molecule and can be elongated over that distance.

One-dimensional conductance histograms generated using logarithm bins for the five silanes studied are shown in Figure 3.10(b). A broad peak in the histograms at a molecule dependent conductance value is observed (black arrows). The peak broadness is attributed to conductance variation from junction to junction primarily due to variations in the Au-S-C torsional angle[2, 77]. The peak positions are plotted in Figure 3.10(c) on a semi-log scale

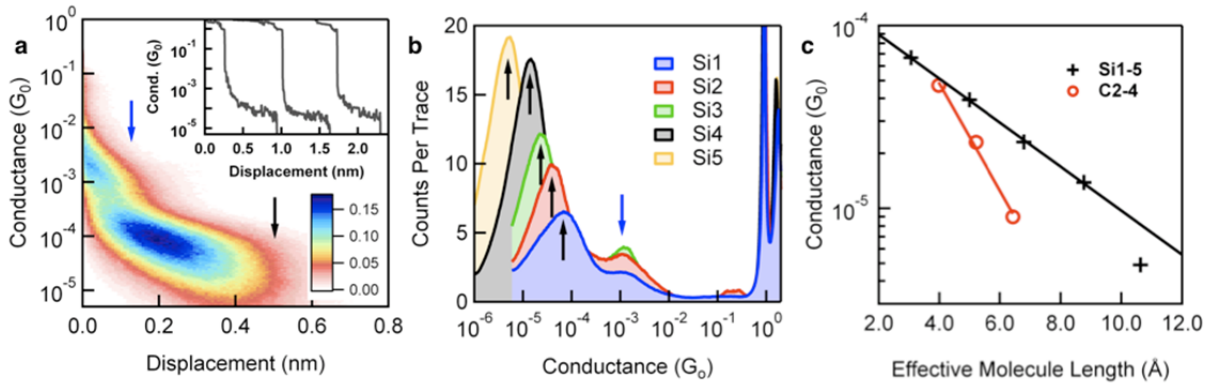


Figure 3.10: (a) 2D conductance histogram for **Si1** showing a clear conductance peak that extends over a distance of 0.5 nm relative to the break of the G_0 contact. The histogram binning is 100 per decade of conductance for the y -axis and 0.0079 nm for the x -axis. The scale bar shows points per trace. The inset shows individual conductance traces. (b) Logarithm-binned conductance histograms generated using a bin size of 100/decade for compounds **Si1–5**. (c) Conductance peak values of the single-molecule junctions for the **Sin** (black) and **Cn** (red) series as functions of the effective molecular length (L , in Å), defined as the distance between the carbons para to the methylthio substituent. L was determined from crystal structures Chem3D and DFT calculations. The values thus obtained varied insignificantly (<3%). The measured decay constants β were $0.27 \pm 0.01 \text{ Å}^{-1}$ for **Sin** and $0.68 \pm 0.05 \text{ Å}^{-1}$ for **Cn**.

against the length of the silane (the distance between the carbons *para* to the methylthio substituent). We see that the conductance decreases exponentially with increasing length for the first four silanes in this series, i.e. $G \sim e^{-\beta L}$ with a $\beta = 0.27 \pm 0.01 / \text{Å}$ [78]. The decay constant measured here is different than the value ($\beta = 0.16 \text{ Å}^{-1}$) measured in a study of photoinduced electron transfer in porphyrin-silane-fullerene dyads[79]. This is not entirely surprising since excited state relaxation and low-bias molecular conduction are fundamentally different processes. This β -value compares favorably to β -values observed for conjugated olefins, which range from $0.17\text{--}0.27 / \text{Å}$ [77, 80]. The statistically determined conductance of the pentasilane **Si5** falls below this line, as can be seen in Figure 3.10(c). We attribute this small decrease in conductance of **Si5** to its slightly twisted backbone structure[81, 82], as determined from DFT calculations (Figure 3.8(d)), which decreases the “conjugation” of this molecule, similar to gauche defects in alkane backbones[83]. Notably, the difference in through-space length between *trans*-**Si5** and the twisted conformer shown in Figure 3.8(d) is insignificant.

Figure 3.10(b) shows that in addition to a strong molecule-dependent peak, all these histograms have a less intense peak at approximately $10^{-3} G_0$ (blue arrows, Figure 3.10(a) and Figure 3.10(b)). The two-dimensional histogram indicates this peak corresponds to conductance features that occur immediately after the single atom contact is broken at a short tip/sample displacement. Although the origin of this high-conductance feature is not fully understood, control experiments with molecules with only one terminal methylsulfide or no anchor groups were conducted to test if the molecule interacts with gold through the Si-backbone, in analogy with an oligoene potentiometer[77]. Neither molecule showed clear conductance signatures (see SI for synthesis and conductance histograms), demonstrating that in fact both sulfides are required for junction formation. Another possibility is that at a short electrode displacement a *cis*-conformation of the molecule in which the thioanisole moieties stack could be formed, leading to a higher conductance with a short molecular plateau length. In support this hypothesis, we offer that conductance through the π - π stack in cyclophanes has been recently reported[84] and that this hypothesis accounts for the observation of the same $10^{-3} G_0$ peak in an analogous alkane series (vide infra).

These conductance results confirm the prediction first advanced several decades ago that while silanes are structural analogs of alkanes, their electronic properties are far more similar to conjugated, unsaturated hydrocarbons[57]. The conductance of oligosilanes **Si1–5** compared to alkanes **C2–4** inspired us to investigate electronic communication between terminal sulfur atoms in these molecules. We conducted density functional theory (DFT) based calculations (B3LYP/6-31G**) on **Si1–Si5**. We found in each case that the HOMO is distributed evenly across the silicon chain, the π systems of the arenes and the p- π orbitals of the two sulfur atoms[85]. The HOMO of **Si4** is depicted as a representative example in Figure 3.11. The contrast with the

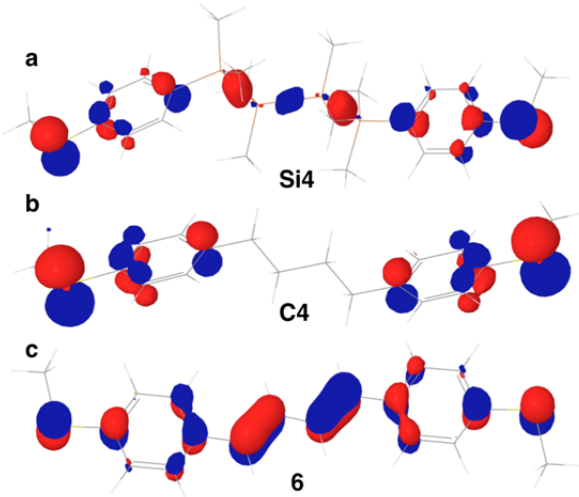


Figure 3.11: B3LYP/6-31G**-calculated HOMOs of (a) tetrasilane **Si4**, (b) butane **C4**, and (c) 1,4-bis(4-(methylthio)phenyl)buta-1,3-diene (**6**).

carbon analog **C4** is dramatic: there is essentially no electron density along the C-C backbone and the HOMO is localized exclusively on the thioanisole fragments. In contrast, the HOMO of a butadiene terminated with 4-(methylthio)phenyl groups (**6**) is fully delocalized, as in the silane, indicating that the two sulfur p- π orbitals couple much more strongly across the Si–Si and C=C bonds than the C–C bond.

To elucidate the greater coupling observed in the Si–Si and C=C materials, we separated the molecular conductors into their constituent components: the 4-(methylthio)phenyl end groups and conducting oligomer[82, 86]. Computational analysis of each part was conducted (see SI, Table S3). We find that the HOMOs of tetrasilane and butadiene are delocalized over the respective C and Si atoms. The HOMO level of 4-methylthioanisole lies at -5.49 eV with respect to vacuum, and it is a close combination of the p- π lone pair on S and the π -space on the ring. We find that of the three oligomers investigated, the tetrasilane (HOMO = -5.96 eV) and butadiene (HOMO = -5.60 eV) lie closest in energy to that of the 4-methylthioanisole, suggesting

that extensive mixing of the thioanisole and Si–Si orbitals (σ (Si-Si)- π conjugation) is occurring; moreover, Figure 3.11 demonstrates that the orbital mixing is geometrically accessible[87]. The HOMO of hexane lies at the substantially lower energy of -8.29 eV, resulting in very minimal mixing of the σ -framework and thionanisole orbitals (negligible σ (C-C)- π conjugation). As a result, the HOMO of **C4** is localized on the thioanisole. Our results indicate that uniform delocalization of the HOMO over the entire molecule improves conductance. Consistent with this observation, a siloxane variant of **Si2** was synthesized in which the Si chain is disrupted with an O atom; no conductance peak was observed (see Appendix Figure A.4 for conductance histogram). We also note in passing that differential orbital coupling may account for the difference in contact resistance observed for alkanes and oligosilanes as seen in Figure 3.10(c).

We present a quantitative comparison of the conductive properties of oligosilanes and alkanes which is enabled by straightforward synthetic access to silanes functionalized with aurophilic contact groups. We have found that saturated Si nanowires display very slow decay of conductance with length; the decay constant is comparable to the decay constant of polyacetylene fragments (oligoenes) and is considerably less than alkane structural analogs. These results, coupled with our theoretical studies, highlight the important role of σ -bond conjugation in charge transport through Si–Si σ bonds. Currently the application of Si oligomers and polymers in electronic devices is limited[64], while applications of conjugated carbon-based materials such as polyacetylene are ubiquitous[88]. The materials described herein have promising physical properties which are complementary to those of rigid, conjugated systems, including conformational flexibility, air and thermal stability, as well as high solubility in common organic solvents. We expect that the desirable physical properties and high conductance

of the materials described herein will result in the development of novel molecular devices and nanoscale architectures.

Acknowledgements

Scanning tunneling microscope-based break junction experiments were supported as part of the Center for Re-Defining Photovoltaic Efficiency Through Molecular-Scale Control, an Energy Frontier Research Center funded by the U.S. Department of Energy (DOE), Office of Science, Office of Basic Energy Sciences under award number DE-SC0001085. LV thanks the Packard Foundation for support. We acknowledge Yi Rong and Ged Parkin of Columbia University for single crystal x-ray diffraction of compound **Si2**. The National Science Foundation (CHE-0619638) is thanked for acquisition of an x-ray diffractometer. We acknowledge Roger A. Lalancette, Department of Chemistry, Rutgers University, Newark, NJ 07102 for the **Si4** x-ray data and solution of the structure. We also acknowledge support by NSF-CRIF Grant No. 0443538 for part of the purchase of the X-ray diffractometer.

3.4 References

1. Parameswaran, R., J.R. Widawsky, H. Vazquez, Y.S. Park, B.M. Boardman, C. Nuckolls, M.L. Steigerwald, M.S. Hybertsen, and L. Venkataraman, *Reliable Formation of Single Molecule Junctions with Air-Stable Diphenylphosphine Linkers*. Journal of Physical Chemistry Letters, 2010. **1**: p. 2114-2119.
2. Park, Y.S., J.R. Widawsky, M. Kamenetska, M.L. Steigerwald, M.S. Hybertsen, C. Nuckolls, and L. Venkataraman, *Frustrated Rotations in Single-Molecule Junctions*. Journal of the American Chemical Society, 2009. **131**(31): p. 10820-10821.
3. Boardman, B.M., J.R. Widawsky, Y.S. Park, C.L. Schenck, L. Venkataraman, M.L. Steigerwald, and C. Nuckolls, *Conductance of Single Cobalt Chalcogenide Cluster Junctions*. Journal of the American Chemical Society, 2011. **133**(22): p. 8455-8457.
4. Wolf, L., *Linker-Free Molecular Wires*. Chemical & Engineering News, 2011. **89**(42): p. 12.
5. Nitzan, A. and M.A. Ratner, *Electron transport in molecular wire junctions*. Science, 2003. **300**(5624): p. 1384-1389.
6. Xu, B.Q. and N.J. Tao, *Measurement of single-molecule resistance by repeated formation of molecular junctions*. Science, 2003. **301**(5637): p. 1221-1223.
7. Venkataraman, L., J.E. Klare, I.W. Tam, C. Nuckolls, M.S. Hybertsen, and M.L. Steigerwald, *Single-Molecule Circuits with Well-Defined Molecular Conductance*. Nano Letters, 2006. **6**(3): p. 458 - 462.
8. Kiguchi, M., O. Tal, S. Wohlthat, F. Pauly, M. Krieger, D. Djukic, J.C. Cuevas, and J.M. van Ruitenbeek, *Highly conductive molecular junctions based on direct binding of benzene to platinum electrodes*. Physical Review Letters, 2008. **101**(4): p. 046801.
9. Kaneko, S., T. Nakazumi, and M. Kiguchi, *Fabrication of a Well-Defined Single Benzene Molecule Junction Using Ag Electrodes*. Journal of Physical Chemistry Letters, 2010. **1**(24): p. 3520-3523.
10. Schneebeli, S.T., M. Kamenetska, Z. Cheng, R. Skouta, R.A. Friesner, L. Venkataraman, and R. Breslow, *Single-Molecule Conductance through Multiple $\pi-\pi$ -Stacked Benzene Rings Determined with Direct Electrode-to-Benzene Ring Connections*. Journal of the American Chemical Society, 2011. **133**(7): p. 2136-2139.
11. Martin, C.A., D. Ding, J.K. Sorensen, T. Bjornholm, J.M. van Ruitenbeek, and H.S.J. van der Zant, *Fullerene-based anchoring groups for molecular electronics*. Journal of the American Chemical Society, 2008. **130**(40): p. 13198-13199.

12. Millar, D., L. Venkataraman, and L.H. Doerrer, *Efficacy of Au-Au Contacts for Scanning Tunneling Microscopy Molecular Conductance Measurements*. J. Phys. Chem. C, 2007. **111**(47): p. 17635-17639.
13. Bulten, E.J. and H.A. Budding, *Synthesis of Small-Ring Monostannacycloalkanes*. Journal of Organometallic Chemistry, 1976. **110**(2): p. 167-174.
14. Kamenetska, M., M. Koentopp, A. Whalley, Y.S. Park, M. Steigerwald, C. Nuckolls, M. Hybertsen, and L. Venkataraman, *Formation and Evolution of Single-Molecule Junctions*. Physical Review Letters, 2009. **102**(12): p. 126803.
15. Hines, T., I. Diez-Perez, J. Hihath, H.M. Liu, Z.S. Wang, J.W. Zhao, G. Zhou, K. Muellen, and N.J. Tao, *Transition from Tunneling to Hopping in Single Molecular Junctions by Measuring Length and Temperature Dependence*. Journal of the American Chemical Society, 2010. **132**(33): p. 11658-11664.
16. Hybertsen, M.S., L. Venkataraman, J.E. Klare, A.C. Whalley, M.L. Steigerwald, and C. Nuckolls, *Amine-linked single-molecule circuits: systematic trends across molecular families*. Journal of Physics: Condensed Matter, 2008. **20**(37): p. 374115.
17. Li, C., I. Pobelov, T. Wandlowski, A. Bagrets, A. Arnold, and F. Evers, *Charge transport in single Au vertical bar alkanedithiol vertical bar Au junctions: Coordination geometries and conformational degrees of freedom*. Journal of the American Chemical Society, 2008. **130**(1): p. 318-326.
18. Akkerman, H.B. and B. de Boer, *Electrical conduction through single molecules and self-assembled monolayers*. Journal of Physics: Condensed Matter, 2008. **20**(1): p. 013001.
19. Park, Y.S., A.C. Whalley, M. Kamenetska, M.L. Steigerwald, M.S. Hybertsen, C. Nuckolls, and L. Venkataraman, *Contact chemistry and single-molecule conductance: A comparison of phosphines, methyl sulfides, and amines*. Journal of the American Chemical Society, 2007. **129**(51): p. 15768-15769.
20. Tomfohr, J.K. and O.F. Sankey, *Complex band structure, decay lengths, and Fermi level alignment in simple molecular electronic systems*. Physical Review B, 2002. **65**(24): p. 245105.
21. Bennett, M.A., S.K. Bhargava, D.C.R. Hockless, L.L. Welling, and A.C. Willis, *Dinuclear Cycloaurated Complexes Containing Bridging (2-Diphenylphosphino)phenylphosphine and (2-Diethylphosphino)phenylphosphine, C₆H₄PR₂ (R = Ph, Et). Carbon–Carbon Bond Formation by Reductive Elimination at a Gold(II)–Gold(II) Center*. Journal of the American Chemical Society, 1996. **118**(43): p. 10469-10478.

22. Yanson, A.I., G.R. Bollinger, H.E. van den Brom, N. Aggrait, and J.M. van Ruitenbeek, *Formation and manipulation of a metallic wire of single gold atoms*. Nature, 1998. **395**(6704): p. 783-785.
23. Porter, K.A., A. Schier, and H. Schmidbaur, α,ω -Bis [(triphenylphosphine)gold(I)] hydrocarbons, in *Perspectives in Organometallic Chemistry*, B.R. Steele and C.G. Scettas, Editors. 2003, Royal Society of Chemistry p. 74-85.
24. Guohui, M. and et al., *Low-bias conductance of single benzene molecules contacted by direct Au-C and Pt-C bonds*. Nanotechnology, 2010. **21**(49): p. 495202.
25. Perdew, J.P., K. Burke, and M. Ernzerhof, *Generalized gradient approximation made simple*. Physical Review Letters, 1996. **77**(18): p. 3865-3868.
26. Jaguar, *Jaguar v7.5*, Schrodinger, L.L.C., New York, NY 2008.
27. Soler, J.M., E. Artacho, J.D. Gale, A. Garcia, J. Junquera, P. Ordejon, and D. Sanchez-Portal, *The SIESTA method for ab initio order-N materials simulation*. Journal of Physics: Condensed Matter, 2002. **14**(11): p. 2745-2779.
28. Brandbyge, M., J.L. Mozos, P. Ordejon, J. Taylor, and K. Stokbro, *Density-functional method for nonequilibrium electron transport*. Physical Review B, 2002. **65**(16): p. 165401.
29. Quek, S.Y., L. Venkataraman, H.J. Choi, S.G. Louie, M.S. Hybertsen, and J.B. Neaton, *Amine-gold linked single-molecule circuits: Experiment and theory*. Nano Letters, 2007. **7**(11): p. 3477-3482.
30. Neaton, J.B., M.S. Hybertsen, and S.G. Louie, *Renormalization of molecular electronic levels at metal-molecule interfaces*. Physical Review Letters, 2006. **97**(21): p. 216405.
31. Koentopp, M., K. Burke, and F. Evers, *Zero-bias molecular electronics: Exchange-correlation corrections to Landauer's formula*. Physical Review B, 2006. **73**(12): p. 121403.
32. Thygesen, K.S. and A. Rubio, *Renormalization of Molecular Quasiparticle Levels at Metal-Molecule Interfaces: Trends across Binding Regimes*. Physical Review Letters, 2009. **102**(4): p. 046802.
33. Delaney, P. and J.C. Greer, *Correlated electron transport in molecular electronics*. Physical Review Letters, 2004. **93**(3): p. 036805.
34. Ma, G.H., X. Shen, L.L. Sun, R.X. Zhang, P. Wei, S. Sanvito, and S.M. Hou, *Low-bias conductance of single benzene molecules contacted by direct Au-C and Pt-C bonds*. Nanotechnology, 2010. **21**(49): p. 495202.

35. von Wrochem, F., D.Q. Gao, F. Scholz, H.G. Nothofer, G. Nelles, and J.M. Wessels, *Efficient electronic coupling and improved stability with dithiocarbamate-based molecular junctions*. Nature Nanotechnology, 2010. **5**(8): p. 618-624.
36. Chen, F., X.L. Li, J. Hihath, Z.F. Huang, and N.J. Tao, *Effect of anchoring groups on single-molecule conductance: Comparative study of thiol-, amine-, and carboxylic-acid-terminated molecules*. Journal of the American Chemical Society, 2006. **128**(49): p. 15874-15881.
37. Mishchenko, A., L.A. Zotti, D. Vonlanthen, M. Burkle, F. Pauly, J.C. Cuevas, M. Mayor, and T. Wandlowski, *Single-Molecule Junctions Based on Nitrile-Terminated Biphenyls: A Promising New Anchoring Group*. Journal of the American Chemical Society, 2011. **133**(2): p. 184-187.
38. Kosov, D.S. and Z.Y. Li, *Dithiocarbamate anchoring in molecular wire junctions: A first principles study*. Journal of Physical Chemistry B, 2006. **110**(20): p. 9893-9898.
39. Haiss, W., C.S. Wang, I. Grace, A.S. Batsanov, D.J. Schiffrian, S.J. Higgins, M.R. Bryce, C.J. Lambert, and R.J. Nichols, *Precision control of single-molecule electrical junctions*. Nature Materials, 2006. **5**(12): p. 995-1002.
40. Reed, M.A., C. Zhou, C.J. Muller, T.P. Burgin, and J.M. Tour, *Conductance of a molecular junction*. Science, 1997. **278**(5336): p. 252-254.
41. Kiguchi, M., S. Miura, T. Takahashi, K. Hara, M. Sawamura, and K. Murakoshi, *Conductance of Single 1,4-Benzenediamine Molecule Bridging between Au and Pt Electrodes*. Journal of Physical Chemistry C, 2008. **112**(35): p. 13349-13352.
42. Smit, R.H.M., Y. Noat, C. Untiedt, N.D. Lang, M.C. van Hemert, and J.M. van Ruitenbeek, *Measurement of the conductance of a hydrogen molecule*. Nature, 2002. **419**(6910): p. 906-909.
43. Cheng, Z.L., R. Skouta, H. Vazquez, J.R. Widawsky, S. Schneebeli, W. Chen, M.S. Hybertsen, R. Breslow, and L. Venkataraman, *In situ formation of highly conducting covalent Au-C contacts for single-molecule junctions*. Nature Nanotechnology, 2011. **6**(6): p. 353-357.
44. Venkataraman, L., J.E. Klare, C. Nuckolls, M.S. Hybertsen, and M.L. Steigerwald, *Dependence of single-molecule junction conductance on molecular conformation*. Nature, 2006. **442**(7105): p. 904-907.
45. Cohen, T. and M. Bhupathy, *Organometallic Compounds by Radical-Anion Induced Reductive Metalation of Phenyl Thioethers*. Accounts of Chemical Research, 1989. **22**(4): p. 152-161.

46. Still, W.C., *(+/-)-Periplanone-B - Total Synthesis and Structure of the Sex Excitant Pheromone of the American Cockroach*. Journal of the American Chemical Society, 1979. **101**(9): p. 2493-2495.
47. Still, W.C., *Stannylation-Destannylation - Preparation of Alpha-Alkoxy Organolithium Reagents and Synthesis of Dendrolasin Via a Carbinyl Carbanion Equivalent*. Journal of the American Chemical Society, 1978. **100**(5): p. 1481-1487.
48. Paulsson, M. and M. Brandbyge, *Transmission eigenchannels from nonequilibrium Green's functions*. Physical Review B, 2007. **76**(11).
49. Thygesen, K.S. and A. Rubio, *Conserving GW scheme for nonequilibrium quantum transport in molecular contacts*. Physical Review B, 2008. **77**(11).
50. Sai, N., M. Zwolak, G. Vignale, and M. Di Ventra, *Dynamical corrections to the DFT-LDA electron conductance in nanoscale systems*. Physical Review Letters, 2005. **94**(18).
51. Toher, C., A. Filippetti, S. Sanvito, and K. Burke, *Self-interaction errors in density-functional calculations of electronic transport*. Physical Review Letters, 2005. **95**(14): p. 4.
52. Evers, F., F. Weigend, and M. Koentopp, *Conductance of molecular wires and transport calculations based on density-functional theory*. Physical Review B, 2004. **69**(23): p. -.
53. Ke, S.H., H.U. Baranger, and W.T. Yang, *Role of the exchange-correlation potential in ab initio electron transport calculations*. Journal of Chemical Physics, 2007. **126**(20): p. 201102.
54. Darancet, P., A. Ferretti, D. Mayou, and V. Olevano, *Ab initio GW electron-electron interaction effects in quantum transport*. Physical Review B, 2007. **75**(7): p. 075102.
55. Quek, S.Y., H.J. Choi, S.G. Louie, and J.B. Neaton, *Length Dependence of Conductance in Aromatic Single-Molecule Junctions*. Nano Letters, 2009. **9**(11): p. 3949-3953.
56. Strange, M., C. Rostgaard, H. Hakkinen, and K.S. Thygesen, *Self-consistent GW calculations of electronic transport in thiol- and amine-linked molecular junctions*. Physical Review B, 2011. **83**(11).
57. West, R. and E. Carberry, *Permethylpolysilanes - Silicon Analogs of Hydrocarbons*. Science, 1975. **189**(4198): p. 179-186.
58. Gilman, H., W.H. Atwell, and G.L. Schwebke, *Ultraviolet Properties of Compounds Containing the Silicon-Silicon Bond*. Journal of Organometallic Chemistry, 1964. **2**(4): p. 369-371.
59. Hausser, K.W., R. Kuhn, A. Smakula, and M. Hoffer, *Photoabsorption and double bonding II Polyenaldehyde and polyencarbon-acids*. Zeitschrift Fur Physikalische

- Chemie-Abteilung B-Chemie Der Elementarprozesse Aufbau Der Materie, 1935. **29**(5): p. 371-377.
60. Gilman, H. and P.J. Morris, *Ultraviolet Spectra of Some Pentahalophenyl-Substituted Silanes*. Journal of Organometallic Chemistry, 1966. **6**(1): p. 102-&.
 61. Carberry, E., R. West, and G.E. Glass, *Cyclic Polysilanes .4. Anion Radicals and Spectroscopic Properties of Permethylcyclopolsilanes*. Journal of the American Chemical Society, 1969. **91**(20): p. 5446-&.
 62. Traven, V.F. and R. West, *Charge-Transfer Complexing between Permethylpolysilanes and Tetranoethylene*. Journal of the American Chemical Society, 1973. **95**(20): p. 6824-6826.
 63. Miller, R.D. and J. Michl, *Polysilane High Polymers*. Chemical Reviews, 1989. **89**(6): p. 1359-1410.
 64. Feigl, A., A. Bockholt, J. Weis, and B. Rieger, *Modern Synthetic and Application Aspects of Polysilanes: An Underestimated Class of Materials?* Silicon Polymers, 2011. **235**: p. 1-31.
 65. David, L.D., P.I. Djurovich, K.L. Stearley, and K.S.V. Srinivasan, *Phenylmethylpolysilanes: formable silane copolymers with potential semiconducting properties*. Journal of the American Chemical Society, 1981. **103**(24): p. 7352-7354.
 66. Holder, S.J., *High-yield controlled syntheses of polysilanes by the Wurtz-type reductive coupling reaction*. Polymer international, 2006. **55**(7): p. 711-718.
 67. Benfield, R.E., R.H. Cragg, and A.C. Swain, *A new insight into the polymodal molecular mass distributions arising in the Wurtz synthesis of polysilanes*. Journal of the Chemical Society. Chemical communications, 1992(2): p. 112-114.
 68. Sen, P.K., D. Ballard, and H. Gilman, *Reaction of chlorine with dodecamethylcyclohexasilane*. Journal of Organometallic Chemistry, 1968. **15**(1): p. 237-&.
 69. Chernyavskii, A.I., D.Y. Larkin, and N.A. Chernyavskaya, *Reactions of dodecamethylcyclohexasilane and polydimethylsilane with metal chlorides*. Journal of Organometallic Chemistry, 2003. **679**(1): p. 17-23.
 70. Shibano, Y., M. Sasaki, H. Tsuji, Y. Araki, O. Ito, and K. Tamao, *Conformation effect of oligosilane linker on photoinduced electron transfer of tetrasilane-linked zinc porphyrin-[60]fullerene dyads*. Journal of Organometallic Chemistry, 2007. **692**(1-3): p. 356-367.
 71. George, C.B., M.A. Ratner, and J.B. Lambert, *Strong Conductance Variation in Conformationally Constrained Oligosilane Tunnel Junctions*. Journal of Physical Chemistry A, 2009. **113**(16): p. 3876-3880.

72. Fleming, I., R. S. Roberts, and S. C. Smith, *The preparation and analysis of the phenyldimethylsilyllithium reagent and its reaction with silyl enol ethers*. Journal of the Chemical Society, Perkin Transactions 1, 1998. **0**(7): p. 1209-1214.
73. Fleming, I., R. Henning, D.C. Parker, H.E. Plaut, and P.E.J. Sanderson, *The Phenyltrimethylsilyl Group as a Masked Hydroxy Group*. Journal of the Chemical Society-Perkin Transactions 1, 1995(4): p. 317-337.
74. Tamao, K., H. Tsuji, M. Terada, M. Asahara, S. Yamaguchi, and A. Toshimitsu, *Conformation control of oligosilanes based on configurationally constrained bicyclic disilane units*. Angewandte Chemie-International Edition, 2000. **39**(18): p. 3287-+.
75. Martin, C.A., D. Ding, J.K. Sorensen, T. Bjornholm, J.M. van Ruitenbeek, and H.S.J. van der Zant, *Fullerene-based anchoring groups for molecular electronics*. Journal of the American Chemical Society, 2008. **130**(40): p. 13198-13199.
76. Quek, S.Y., M. Kamenetska, M.L. Steigerwald, H.J. Choi, S.G. Louie, M.S. Hybertsen, J.B. Neaton, and L. Venkataraman, *Mechanically controlled binary conductance switching of a single-molecule junction*. Nature Nanotechnology, 2009. **4**(4): p. 230-234.
77. Meisner, J.S., M. Kamenetska, M. Krikorian, M.L. Steigerwald, L. Venkataraman, and C. Nuckolls, *A Single-Molecule Potentiometer*. Nano Letters, 2011. **11**(4): p. 1575-1579.
78. Salomon, A., D. Cahen, S. Lindsay, J. Tomfohr, V.B. Engelkes, and C.D. Frisbie, *Comparison of electronic transport measurements on organic molecules*. Advanced Materials, 2003. **15**(22): p. 1881-1890.
79. Sasaki, M., Y. Shibano, H. Tsuji, Y. Araki, K. Tamao, and O. Ito, *Oligosilane chain-length dependence of electron transfer of zinc porphyrin-oligosilane-fullerene molecules*. Journal of Physical Chemistry A, 2007. **111**(16): p. 2973-2979.
80. Visoly-Fisher, I., K. Daie, Y. Terazono, C. Herrero, F. Fungo, L. Otero, E. Durantini, J.J. Silber, L. Sereno, D. Gust, T.A. Moore, A.L. Moore, and S.M. Lindsay, *Conductance of a biomolecular wire*. Proceedings of the National Academy of Sciences of the United States of America, 2006. **103**(23): p. 8686-8690.
81. Albinsson, B., D. Antic, F. Neumann, and J. Michl, *Conformers of n-Si₅Me₁₂: A comparison of ab initio and molecular mechanics methods*. Journal of Physical Chemistry A, 1999. **103**(14): p. 2184-2196.
82. Schepers, T. and J. Michl, *Optimized ladder C and ladder H models for sigma conjugation: chain segmentation in polysilanes*. Journal of Physical Organic Chemistry, 2002. **15**(8): p. 490-498.
83. Jones, D.R. and A. Troisi, *Single molecule conductance of linear dithioalkanes in the liquid phase: Apparently activated transport-due to conformational flexibility*. Journal of Physical Chemistry C, 2007. **111**(39): p. 14567-14573.

84. Schneebeli, S.T., M. Kamenetska, Z.L. Cheng, R. Skouta, R.A. Friesner, L. Venkataraman, and R. Breslow, *Single-Molecule Conductance through Multiple pi-pi-Stacked Benzene Rings Determined with Direct Electrode-to-Benzene Ring Connections*. Journal of the American Chemical Society, 2011. **133**(7): p. 2136-2139.
85. Pitt, C.G. and H. Bock, *Sigma-Pi Mixing in Phenylpentamethyldisilane*. Journal of the Chemical Society-Chemical Communications, 1972(1): p. 28-&.
86. Bock, H. and W. Ensslin, *Photoelectron Spectroscopy and Molecular Properties .3. Bond-Bond Interaction in Polysilanes*. Angewandte Chemie-International Edition, 1971. **10**(6): p. 404-&.
87. Pitt, C.G., E.C. Toren, and R.N. Carey, *Nature of Electronic Interactions in Aryl-Substituted Polysilanes*. Journal of the American Chemical Society, 1972. **94**(11): p. 3806-&.
88. Heeger, A.J., *Semiconducting polymers: the Third Generation*. Chemical Society Reviews, 2010. **39**(7): p. 2354-2371.

Chapter 4

Concurrent Conductance and Thermopower Measurements

The work described in this chapter was done in collaboration with Wenbo Chen, who performed the synthetic chemistry, from the group of Prof. Ronald Breslow. Theoretical work was provided by Mark Hybertsen, Hector Vazquez, Pierre Darancet and Jeffrey Neaton as well. I built the thermal apparatus, performed all of the STM work and data analysis, and developed the models that describe the observed trends.

We can also use single molecule conductance measurements to study the thermoelectric effect. When a temperature difference is imposed across a material, the electric charge carriers, whether they are electrons or holes, will migrate from the hot side to the cold side, thereby resulting in a thermally-induced electrical current (which is fundamentally distinct from the flow of heat current). The extent to which this occurs is an inherent property of the material and gauged by a parameter called the Seebeck coefficient, S . The Seebeck coefficient is given in units of V/K , which describes the open-circuit potential buildup (thermoelectric voltage) that occurs per degree difference in temperature.

Thermoelectric devices can be used to convert excess thermal energy to useful electrical energy in order to minimize the impact of heat loss. The field of thermoelectrics has centered on finding materials that maximize the thermoelectric figure of merit, ZT , a measure of device efficiency. One strategy to do this is to focus on increasing its numerator, the power factor, GS^2 . Here, we study the thermoelectric effect in single molecule junctions, where the thermopower comes as a direct result of the different Fermi distributions in each of the leads. We investigate the thermoelectric properties of a few systems of molecular junctions and because we can measure junction thermopower and conductance concurrently in every junction, we are able to compare junction power factor.

In this chapter, I use measurement of thermopower to identify the conducting orbitals (charge carriers) of amine-linked and pyridine-linked junctions by observing the direction of current flow and we compare the results to DFT calculations. Afterwards, I study how thermopower changes as a function of molecule length by measuring the covalently bonded junctions from Chapter 3. We find that the thermopower increases monotonically and non-linearly with length and offer a tight binding model to explain the trend.

4.1 Simultaneous Determination of Conductance and Thermopower of Single Molecule Junctions*

Abstract

We report the first concurrent determination of conductance (G) and thermopower (S) of single-molecule junctions via direct measurement of electrical and thermoelectric currents using a scanning tunneling microscope-based break-junction technique. We explore several amine-Au and pyridine-Au linked molecules that are predicted to conduct through either the highest occupied molecular orbital (HOMO) or the lowest unoccupied molecular orbital (LUMO), respectively. We find that the Seebeck coefficient is negative for pyridine-Au linked LUMO-conducting junctions and positive for amine-Au linked HOMO-conducting junctions. Within the accessible temperature gradients (<30 K), we do not observe a strong dependence of the junction Seebeck coefficient on temperature. From histograms of 1000's of junctions, we use the most probable Seebeck coefficient to determine a power factor, GS^2 , for each junction studied, and find that GS^2 increases with G . Finally, we find that conductance and Seebeck coefficient values are in good quantitative agreement with our self-energy corrected density functional theory calculations.

Understanding transport characteristics of single metal-molecule-metal junctions is of fundamental importance to the development of functional nanoscale, organic-based devices[1]. Much work has been performed investigating the low-bias conductance of molecules attached to gold leads using a variety of chemical link groups[2-7]. However, conductance measurements provide only a partial description of electron transport through molecules, and cannot directly probe molecular energy level alignment with the electrode Fermi energy or level broadening due to electronic coupling to the leads. Thus, there is significant value in developing complimentary methods to investigate junction electronic structure and attain a more complete understanding of molecular-scale transport. In particular, molecular junction thermopower measurements can be useful in determining the dominant molecular orbital for transport and the identity of the primary

* J. R. Widawsky, P. Darancet, J. B. Neaton, and L. Venkataraman, **Nano Letters**, 12, 354–358, (2012)

charge carriers[8-11]. In a single-molecule junction, the thermopower or Seebeck coefficient, S , determines the magnitude of the built-in potential developed across a material (or molecule) when a temperature difference, ΔT , is applied. With the additional presence of an external voltage bias ΔV across the junction, following Ref. [12], Equation (17), the total current, I , in this case is simply

$$I = -G\Delta V + GS\Delta T, \quad (1)$$

where G is the electrical conductance. Eq. (1) applies for both bulk materials, where transport is (e.g.) diffusive[13], and in single-molecule junctions, where transport can be coherent[14]. For coherent tunneling, the conductance through a molecular junction, in the zero-bias limit, can be given by the Landauer formula[13, 14],

$$G = \frac{2e^2}{h} \mathcal{T}(E_f) \quad (2)$$

and the Seebeck coefficient by

$$S(E_f) = -\left. \frac{\pi^2 k_B^2 T}{3e\mathcal{T}(E)} \frac{\partial \mathcal{T}(E)}{\partial E} \right|_{E=E_f} \quad (3)$$

where $T(E)$ is the transmission function, $T [= (T_1 + T_2)/2]$ is the average temperature of the leads, E_f is the Fermi Energy of the leads and k_B is the Boltzmann constant. In this coherent tunneling limit, the current at zero external bias is then only due to a difference in temperature between the two leads, and depends on the slope of the transmission function at the Fermi energy, E_F . Thus, from the sign of this thermoelectric current (and therefore S), we can potentially deduce whether E_F is closer to the highest occupied molecular orbital (HOMO) or lowest unoccupied molecular orbital (LUMO) resonance energy, assuming a simple Lorentzian-type model.

Here, we present a study of thermopower measurements for several amine-Au linked HOMO-conducting and pyridine-Au linked LUMO-conducting single-molecule junctions. In

contrast to previous measurements in which thermal and electronic properties are not measured on the same junctions[8-11] or have been measured simultaneously on a junction containing a few molecules[15], we determine both the conductance, G , and the Seebeck coefficient, S , concurrently for an individual molecular junction. Conductance values are obtained by measuring the current across the gold-molecule-gold junction at an applied bias voltage of 10 mV. The Seebeck coefficient on the same junction is determined from the measured thermoelectric current through the junction held under a temperature gradient while maintaining a zero (externally-applied) bias voltage across the junction. We find that amine-terminated molecules have $S > 0$, suggesting that the HOMO resonance is closest to E_F , while pyridine-terminated molecules have $S < 0$, indicating that the LUMO resonance is closest. We also find that a diphenylphosphine-terminated alkane has an S near zero, indicating that E_F is probably very close to the middle of the HOMO-LUMO gap. We compare our measurements with first principles transport calculations that are based on standard density functional theory (DFT) that is extended to incorporate self-energy corrections[16, 17], and find quantitative agreement with both conductance values and Seebeck coefficients. Our calculations confirm the sign of S in the case of each junction, and its expected relationship with the frontier orbital closest to E_F , but also reveal a complex transmission for amine-linked junctions, with implications for the relationship between S and G . In particular, for amine-linked junctions, $T(E)$ is non-Lorentzian and thus S varies significantly more than G from junction to junction.

Single molecule junctions are created using the scanning tunneling microscope-based break junction technique (STM-BJ), in which a sharp gold tip is brought in and out of contact with a gold substrate in an environment of a target molecule[3, 18]. The molecules used in this study are 4,4'-diaminostilbene (1), bis-(4-aminophenyl)acetylene (2), 1,5-

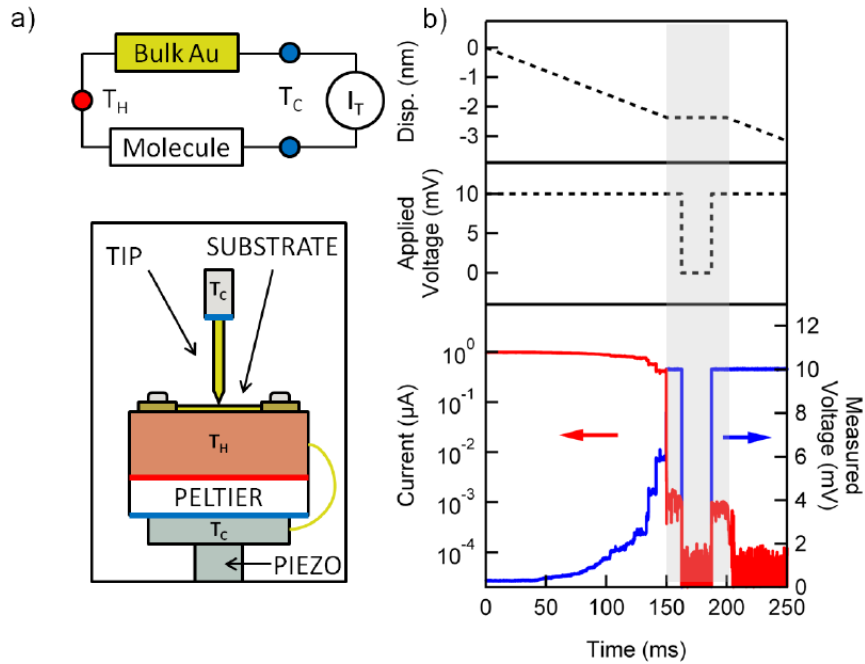


Figure 4.1: (a) Top panel: Schematic of the STM-BJ setup modified to perform thermal measurements. Bottom panel: Simplified diagram illustrating measurement of thermoelectric current (I_T) when a temperature gradient is imposed. (b) Top panel: Piezo ramp used, including a “hold” portion between 150 and 200 ms. Middle panel: External applied voltage across the leads which drops to zero during the center of the “hold” portion. Bottom panel: Sample trace for an example molecular junction. The measured current is shown in red and the voltage measured across the junction is shown in blue. Note: The voltage is applied across the junction in series with a $10 \text{ k}\Omega$ resistor.

bis(diphenylphosphino)pentane (**3**), 4,4'-bipyridine (**4**) and 1,2-di(4-pyridyl)ethylene (**5**). The target molecules are deposited onto the STM substrate by thermal evaporation under ambient conditions (except for (**3**) which is deposited from an acetone solution) and thus measurements are not carried out in solvent. A thermal gradient is applied using a Peltier heater to controllably heat the substrate to temperatures ranging from room temperature to 60°C while maintaining the tip close to room temperature, and the thermoelectric current through these junctions is measured at zero applied bias. The set-up is allowed to come to thermal equilibrium for about one hour at each temperature before measurements are continued. In all measurements reported here, the temperature difference (ΔT) between the tip and substrate is set at approximately one of three values: 0K, 14K, 27K. In order minimize unaccountable thermoelectric voltages across the leads,

a pure gold wire is used to apply the voltage to the hot substrate and is also connected to the cold side of the peltier. A schematic of the circuitry as well as the STM layout is shown in Figure 4.1(a).

Conductance and thermoelectric current measurements are carried out using a modified version of the STM-BJ technique[19]. Briefly, the Au STM tip is brought in contact with the heated Au substrate while applying a bias voltage of 10 mV until a conductance greater than $5 G_0$ is measured. The tip is first retracted from the substrate by 2.4 nm at a speed of 15.8 nm/s, then held fixed for 50 ms, and finally withdrawn an additional 0.8 nm as illustrated by the piezo ramp shown in Figure 4.1(b). During this ramp, the current through the junction and the voltage across the junction is continuously measured at a 40 kHz acquisition rate. The applied bias is set to zero during the middle 25 ms of the 50 ms period when the tip/substrate distance is fixed (Figure 4.1(b)). For every molecule, and tip/sample pair, over 3600 measurements are collected at each of the three ΔT 's listed above. For each measurement, the data during the 50 ms hold period are analyzed further, as described in detail in the SI. Briefly, the junction conductance during the first and last 12.5 ms of the “hold” period is determined. If both values are found to be within a molecule dependent range as determined from a conductance histogram, the trace is selected, for this indicates that a molecular junction is sustained during the entire 50 ms “hold” period. Conductance histograms for **4** and **5**, show two peaks due to two different binding geometries[17]. Here, we analyze these molecular junctions in the high conductance configuration. The analysis of **4** in the low-conducting configuration is included in the Appendix Section A.4. Typically, about 10-20% of the measured traces are selected for analysis, since only these have a molecule bridging the tip and substrate during the “hold” period of the ramp. A single selected measurement for **1** is shown in Figure 4.1(b), where measured current is in red

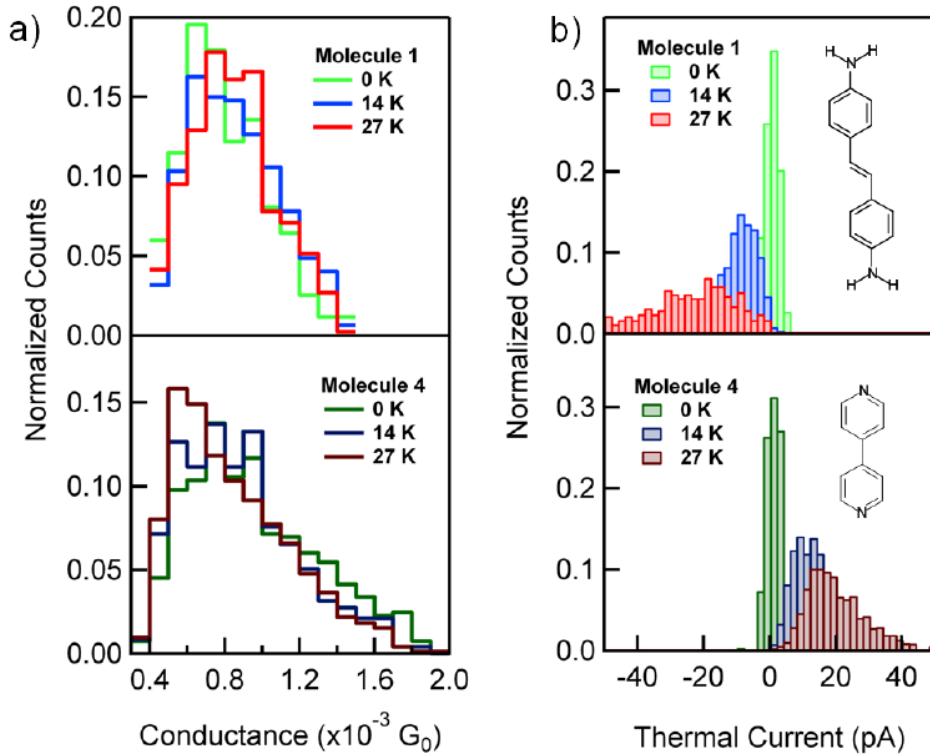


Figure 4.2: (a) Average measured conductance histograms for molecules **1** (top) and **4** (bottom) for the three ΔT s ($\Delta T = 0$ K, green; $\Delta T = 14$ K, blue; and $\Delta T = 27$ K, red). (b) Average thermoelectric current histograms for molecules **1** (top) and **4** (bottom) for the three ΔT s ($\Delta T = 0$ K, green; $\Delta T = 14$ K, blue; and $\Delta T = 27$ K, red). For **1**, the thermoelectric current shifts left with increasing ΔT , while for **4**, the thermoelectric current shifts right.

and measured voltage is in blue. The junction thermoelectric current is determined by averaging the measured junction current during the middle 25 ms of the “hold” period and the junction conductance is determined by averaging the conductance during the first and last 12.5 ms of the “hold” period. This allows a determination of junction conductance and thermoelectric current for each individual junction formed, and thus allows a simultaneous determination of G and S for each junction.

In Figure 4.2, we show histograms of conductance values and average thermoelectric currents for **1** and **4** determined on a trace by trace basis for measurements at three different ΔT values. Conductance and thermoelectric current distributions for other molecules studied are shown in the SI. We see that with a ΔT of 0 K, the thermoelectric current histogram is narrow

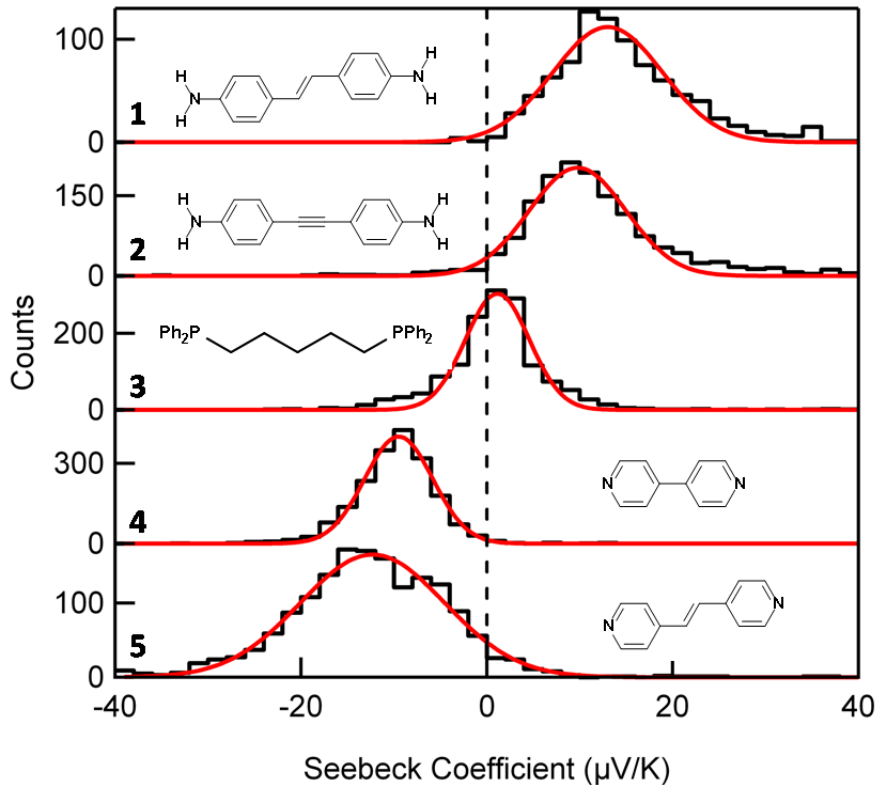


Figure 4.3: Histograms of Seebeck coefficient for all molecules **1**–**5**. Histograms are fit with Gaussians (red). **1** and **2** exhibit positive S while **4** and **5** exhibit negative S . The Seebeck coefficient for **3** is close to zero.

and centered about zero for both molecules, implying that on average, no current flows without an applied temperature difference between the tip and substrate, consistent with the expression for current in Equation 1. For molecule **1**, we find that with a finite ΔT , the thermoelectric current (from the tip to the substrate) is negative while for **4** we measure a positive thermoelectric current. We also see that the peak of the thermoelectric current distributions for **1** (**4**) shifts to lower (higher) value with increasing ΔT , thus the magnitude of the thermoelectric current increases with increasing ΔT .

The Seebeck coefficient for the entire system, S_{Measured} , is determined by first substituting, in Equation (1), the conductance and thermoelectric currents determined for each measured trace ($S_{\text{Measured}} = I/G\Delta T$). Since the system includes a section of gold wire which is maintained under the

Molecule	G_{EXP} [10^{-3} G_0]	S_{EXP} [$\mu\text{V/K}$]	$(GS^2)_{\text{EXP}}$ [10^{-18} W/K^2]	$G_{\text{DFT+}\Sigma}$ [10^{-3} G_0]	$S_{\text{DFT+}\Sigma}$ [$\mu\text{V/K}$]
1	0.63	13.0	8.25	0.58	5.89
2	0.57	9.7	4.16	0.62	4.71
3	0.39	1.1	0.037	0.70	0.33
4 (HighG)	0.68	-9.5	4.76	0.20	-7.88
4 (LowG)	0.12	-11.5	1.23	0.18	-10.1
5 (HighG)	0.24	-12.3	2.81	0.07	-12.11

Table 4.1: Experimental and DFT+ Σ calculated values for conductance (G) and thermopower (S). Also given are the experimental values for the molecular power factor (GS^2).

opposite thermal gradient ($-\Delta T$), the Seebeck coefficient of the Au-molecule-Au junction is given by $S_{\text{Junction}} = S_{\text{Au}} - S_{\text{Measured}}$, where we use $S_{\text{Au}} = 2 \mu\text{V/K}$ [20]. In Figure 4.3, we show the distribution of molecular Seebeck coefficients (when the molecules are attached to Au electrodes) determined for all five compounds studied by including measurements at all ΔT s. These distributions are fit to a Gaussian and the peak positions are given in Table 4.1, along with measured conductance values. We use the most probable molecular junction conductance and Seebeck coefficients to determine a power factor, GS^2 , for these systems, which are also given in Table 4.1. We see first that the amine-terminated molecules (**1** and **2**) have a positive Seebeck coefficients indicating HOMO conductance, while the **4** and **5** have a negative Seebeck coefficient (LUMO-conducting). For molecule **3**, although we measure a small positive S_{Junction} , the magnitude is small enough to conclude that for this alkane, E_F is very close to mid-gap.

To understand these measurements, we use first-principles calculations with a self-energy corrected, parameter-free scattering-state approach based on density functional theory (DFT)[17, 21, 22] to determine both the linear response conductance (Eq. 2) and the Seebeck coefficient

(Eq. 3). Eq. (3) assumes that $T(E)$ varies smoothly for $|E - E_F| < k_B T$, and that ΔT is small compared to T [14, 23]. Both assumptions hold for the systems studied here ($|\Delta T| < 30$ K). Moreover, since the measured thermoelectric current is found to be approximately linear with ΔT for the small values of ΔT in the experiments, we expect the steady-state scattering formalism will also be valid[24].

We model the electrodes using two Au(111) slabs with 7 layers of gold for the leads, using a 4×4 unit cell. To reduce computational burden for molecule **3**, we replace the phenyl groups with methyl groups, a simplification that has been shown not to affect conductance experimentally[25]. Previous work established that for both amine- and pyridine-Au linked molecular junctions that the amine or pyridine group binds selectively to undercoordinated atop Au sites[21, 22]. Accordingly, we use two different undercoordinated binding site motifs, consisting of either a trimer of gold or an adatom to represent the tip to which the molecules bind[16, 21]. All junction geometries are fully relaxed within DFT-GGA (PBE) using SIESTA[26]. Transmission functions are calculated using a self-energy corrected scattering-states approach, “DFT+ Σ ”, to the Landauer formula as implemented in the Scarlet code[27].

Junction structures for molecules **1** and **4** are shown in Figure 4.4. To calculate the junction transmission, we augment the Kohn-Sham excitation energies with a model self-energy correction that has consistently led to quantitative agreement for both conductance[17, 21, 22] and Seebeck coefficient[16]. Specifically, we correct the gas-phase gap with a Δ SCF[28] calculation, and correct for the lack of static non-local correlation effects through an electrostatic “image charge” model, following prior work[17]. G and S are then determined from the transmission and its derivative at E_F , via Eq. 2 and 3. Numerical evaluation of the derivative of $T(E)$ generally requires a very fine k_{\parallel} -point sampling. To minimize sampling errors, we fit $T(E)$

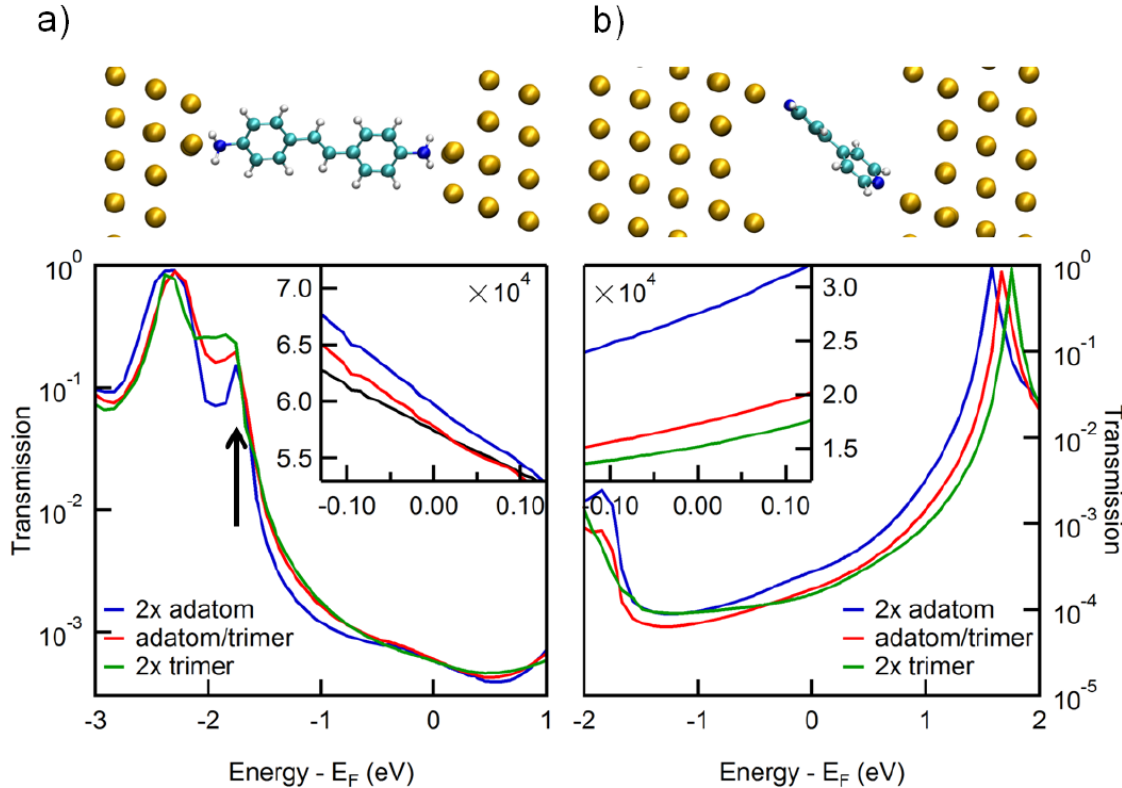


Figure 4.4: Upper panel: The optimized geometries for junctions with molecules (a) **1** and (b) **4**. Lower panel: Transmission curves shown on a log scale for both molecules calculated using DFT+ Σ . Arrow indicates the position of the Au-d states. Insets: Transmission curves around E_F on a linear scale.

around E_F with a smooth function, and take its derivative analytically. Comparing these two approaches for one junction, 1,4-benzenediamine-Au[16], we find a less than 5% difference in S obtained from numerically differentiating $T(E)$ on a 24×24 $k_{||}$ -grid and fitting a $T(E)$ calculated on an 8×8 $k_{||}$ -grid. For all the results presented here, $T(E)$ is computed on a 16×16 $k_{||}$ -grid, with S determined from the analytic derivative of a fit to the transmission function around E_F .

The transmission curves for **1** and **4** are shown in Figure 4.4 and the calculated values for G and $S_{Junction}$ are reported in Table 4.1. We find that for amine-linked junctions, $T(E_F)$ originates with a HOMO-derived peak, and a weakly-transmitting feature formed from a hybridization of Au-d and N-lone pair states, resulting in a positive S . The calculated G are within 15% of the experiments, and do not vary much with the coordination of the Au binding site, in agreement

with past work showing that junction geometry does not affect conductance significantly[21, 29]. For the pyridine-linked junctions, transmission at the Fermi level results from a LUMO derived peak, hence S is negative. The calculated G is within a factor of 3 of the experiment but varies significantly with the Au binding site coordination, again in agreement with past work[30]. The calculated Seebeck coefficients for both series are within a factor of 2 of the experimental values.

For the amine-linked junctions, hybridization between the HOMO resonance and Au d-states \sim 1.8 eV below E_F (cf. arrow in Figure 4.4(a)) results in an appreciable energy-dependent coupling, and the single Lorentzian model breaks down. Increasing the binding site coordination significantly alters the lineshape and the Seebeck coefficients (15% variation for molecule **1**), but results in just a modest rise in the density of states at E_F and small changes in the conductance (3% variation). Interestingly, S is more sensitive to HOMO-Au 5d hybridization features in $T(E)$ than G . Because these features may be underestimated by approximations associated with DFT+ Σ , deviations from experiment may be somewhat greater for S than for G for HOMO-conducting amine-Au junctions. For molecules **1** and **2**, the simultaneous measurement of G and S allows an assessment of the efficacy of Lorentzian models. If the transmission function has a simple Lorentzian form for a molecule symmetrically coupled to both electrodes[8, 9], S and G determine the resonance energy relative to E_F . However, for the amine-Au linked junctions studied here, a single-Lorentzian model (see SI) significantly underestimates the resonance energy. For molecule **1**, the single-Lorentzian model would place the HOMO at -1.1 eV while our DFT+ Σ calculations show that HOMO is around -2.3 eV. Thus the non-Lorentzian behavior of amine-linked junctions observed here, and seen with some other linkers[7] could allow for the tuning of their S without greatly affecting G through the position of the d-states, for example using transition metal contacts with d-states closer to E_F .

For pyridine-linked junctions, the calculated DFT+ Σ transmission function has a Lorentzian form, with a prominent resonance with LUMO character. Increasing the binding site coordination pushes the LUMO resonance away from E_F . In a single Lorentzian model in the weak-coupling limit, $(\Gamma/\Delta E)^2 \ll 1$ (where Γ is an energy-independent coupling or injection rate, and ΔE the difference between the LUMO resonance energy and E_F), and the Seebeck coefficient varies more slowly with ΔE (as $1/\Delta E$) than the conductance ($1/\Delta E^2$). This is indeed what we find in our calculations. For molecule **4**, S has a +/-5% variation for the different binding sites, while the conductance changes by +/-25%. This Lorentzian-like behavior is further validated by the estimate of the resonance positions, in close agreement with first-principles calculations (1.53 eV determined using the experimental S and G compared with 1.47 eV from our calculations of molecule **4**).

In conclusion, we have demonstrated that we can determine the conductance and thermoelectric current concurrently through single-molecule junctions. The thermoelectric currents are used to determine a Seebeck coefficient for each junction. We find that amine-terminated molecular junctions have a positive Seebeck coefficient in agreement with calculations that show that the HOMO is the molecular resonance that is closest to E_F . In contrast, pyridine-terminated molecular junctions have a negative Seebeck coefficient and conduct through the LUMO. These experimental results are in good quantitative agreement with those from self-energy corrected DFT calculations, which also reveal a complex, non-Lorentzian form for transmission for amine-linked junctions.

Acknowledgements

We thank M. S. Hybertsen, H. J. Choi, and S. Y. Quek for discussions and S. Berkley for help with measurements. This work was supported in part by the EFRC program of the U.S. Department of Energy (DOE) under Award No. DE-SC0001085 and the ACS-PRF program. L.V. thanks the Packard Foundation for support. Portions of this work were performed at the Molecular Foundry and within the Helios Solar Energy Research Center, both were supported by the Office of Basic Energy Sciences of the U.S. Department of Energy under Contract No. DE-AC02-05CH11231. We acknowledge NERSC for computing resources.

4.2 Length-Dependent Thermopower of Highly Conducting Au-C Bonded Single Molecule Junctions*

Abstract

We report the simultaneous measurement of conductance and thermopower of highly conducting single-molecule junctions using a scanning tunneling microscope-based break-junction setup. We start with molecular backbones (alkanes and oligophenyls) terminated with trimethyltin end groups that cleave off *in situ*, to create junctions where terminal carbons are covalently bonded to the Au electrodes. We apply a thermal gradient across these junctions and measure their conductance and thermopower. Due to the electronic properties of the highly-conducting Au-C links, the thermoelectric properties and power factor are exceptionally high. Our results show that the molecular thermopower increases non-linearly with the molecular length while conductance decreases exponentially with increasing molecular length. Density functional theory calculations show that a gateway state representing the Au-C covalent bond plays a key role in the conductance. With this as input, we analyze a series of simplified models and show that a tight-binding model that explicitly includes the gateway states and the molecular backbone states accurately captures the experimentally measured trends.

The development of viable thermoelectric devices using organic based materials has centered around finding materials that maximize the thermoelectric figure of merit[31, 32], $ZT = GS^2T/\kappa$, where G is the electrical conductance, S is the thermopower, and κ is the thermal conductivity. Measuring material performance on a fundamental length scale at the single-molecule level[1] can thus provide a better understanding of structure-function relations in these systems. Reliable thermoelectric measurements of molecular assemblies with metal electrodes[15, 33, 34] and at the single-molecule level[8-11, 35] have recently been carried out with different organic systems. In this work, we measure conductance and thermopower for a

* J. R. Widawsky, W. Chen, H. Vazquez, T. Kim, R. Breslow, M. S. Hybertsen, and L. Venkataraman, *submitted*

series of trimethyl-tin terminated oligophenyls and alkanes that bind directly to Au electrodes by forming covalent Au-C sigma bonds[7] after the trimethyl-tin groups cleave *in situ*. The conductances of the oligophenyls range from about $0.9 G_0$ for a single benzene to $1.0 \times 10^{-3} G_0$ for tetraphenyl[7], the longest in this series, and our results show that we maximize the power factor, GS^2 , for the biphenyl (which has a conductance of about $0.1 G_0$ and a thermopower of $14.3 \mu\text{V/K}$) at 1.6 fW/K^2 . We also measure conductance and thermopower for alkanes with 6 to 10 methylene units that bind through Au-C bonds. Their conductance ranges from 1.4×10^{-2} to $2.5 \times 10^{-4} G_0$ and show thermopowers of $5.0\text{--}5.6 \mu\text{V/K}$. This is significantly larger than what we have measured for phosphine-linked alkane chains[35], indicating that these alkane based molecular junctions can have a substantial thermopower despite their low conductance. To explain these results, we examine density functional theory based calculations of electron transmission through exemplary model structures for these junctions. The calculations indicate that gateway states representing Au-C sigma bonds at the links play a key role. In contrast to more simplified models, a tight-binding model that explicitly includes the gateway state in addition to molecular backbone states accurately captures the experimentally measured trends in conductance and thermopower and reproduces the essential qualitative features from the density functional theory based calculations.

In a single-molecule junction, the thermopower or Seebeck coefficient, S , determines the magnitude of the built-in potential developed across a material (or molecular junction) when a temperature difference, ΔT , is applied. With the additional presence of an external voltage bias, ΔV , across the junction,[12, 14] the total current, I , is simply given by $I = -G\Delta V + GS\Delta T$, where G is the electrical conductance. The thermopower can be measured either from the zero-bias thermoelectric current ($S = I/G\Delta T$ when $\Delta V = 0$) or from the open circuit voltage ($S =$

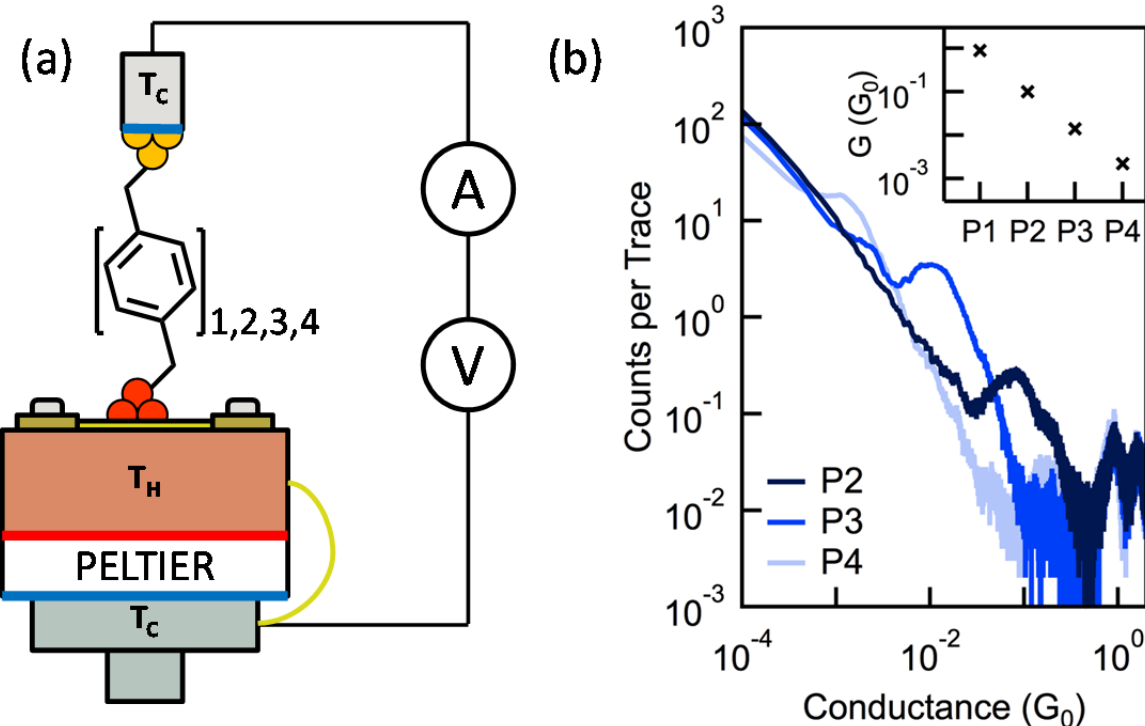


Figure 4.5: (a) Schematic of the STM-BJ set-up representing thermoelectric measurement of **P1-P4**. (b) Conductance histograms of **P2-P4** obtained during the thermoelectric measurement. The bin size is $10^{-4} G_0$. Inset: Conductance plotted as a function of number of phenyls in the molecular backbone.

$\Delta V/\Delta T$ when $I = 0$). These equations applies to both bulk materials, where transport is, for example, diffusive[13] and to single-molecule junctions, where transport can be coherent[14].

For coherent tunneling, the conductance through a molecular junction in the zero-bias limit is

given by the Landauer formula[13, 14], $G = \frac{2e^2}{h} \mathcal{T}(E_f)$, and the thermopower becomes $S =$

$$-\left. \frac{\pi^2 k_B^2 T}{3e \mathcal{T}(E)} \frac{\partial \mathcal{T}(E)}{\partial E} \right|_{E=E_f}.$$

We simultaneously measure the conductance and thermopower of single-molecule junctions using the scanning tunneling microscope-based break junction technique[3, 18] (STM-BJ). A schematic of the circuitry as well as the STM layout is shown in Figure 4.5(a). Single-molecule junctions are formed between an Au STM tip and substrate by repeatedly bringing the substrate in and out of contact with the tip in an environment of the target molecules. The

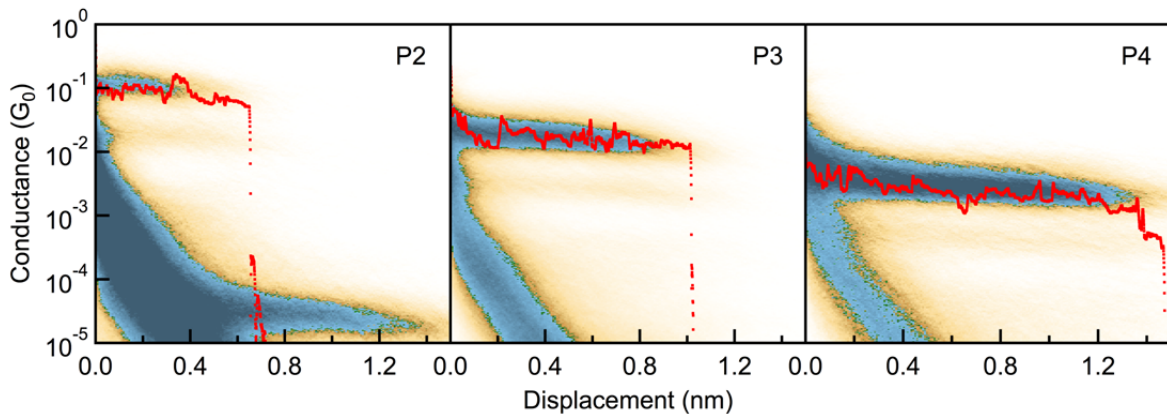


Figure 4.6: Two-dimensional conductance histograms of **P2-P4**. Representative conductance traces for each molecule is shown as superimposed dotted lines. The bins have a width of 0.008 nm along the displacement axis and 100/decade along the conductance axis. The molecular plateau between 10^{-5} and $10^{-4} G_0$ in the 2D histogram for **P2** is due to the dimer molecule formed *in situ*.

molecules used here are trimethylstannylmethyl-terminated oligophenyls with 1-4 phenyl rings (**P1-P4**) and trimethylstannyl[36] terminated alkanes (**C6**, **C8**, and **C10**) (see Appendix Figure A.11 for structures), which were synthesized following procedures detailed before.[7, 37] These compounds are deposited onto the Au substrate from an acetone solution (~10 mM concentration). The trimethyl-tin (SnMe_3) terminations of the molecules cleave off *in situ*, yielding single-molecule junctions where the terminal carbon of the molecular backbone is covalently bonded to the Au electrode. The resulting junctions have a conductance that is significantly higher[7, 37] than those formed with conventional linkers such as thiols[18, 38], amines[3], or methyl sulfides[39].

In these experiments, the molecular junction conductance is measured as a function of the relative tip/sample displacement yielding conductance traces. Conductance traces show plateaus at integer multiples of G_0 , the quantum of conductance and typically an additional plateau at a molecule dependent conductance value. Thousands of conductance traces are collected for each compound and used to create one-dimensional conductance histograms. The linear-binned conductance histograms for **P2**, **P3**, and **P4** are given in Figure 4.5(b) with a bin size of $10^{-4} G_0$.

As the number of phenyls is increased, we see that the molecular junction conductance decreases exponentially as shown in the inset of Figure 4.5(b). To confirm that these peaks are indeed due to the formation of an Au/molecule/Au junction, we also create two-dimensional conductance-displacement histograms. These are shown in Figure 4.6 for **P2-P4**. We see that the plateau length increases systematically as the molecular backbone length increases, indicating that we are indeed measuring transport through these backbones[40]. The conductance feature between 10^{-5} and $10^{-4} G_0$ in the case of **P2** in Figure 4.6 (left) is due to the dimer molecule which forms *in-situ*.[37] This dimer molecule has two biphenyls connected by a saturated 2-carbon bridge, giving it a much lower conductance than the fully conjugated **P4**. **P1** exhibits near resonant transport with a conductance of about $0.90 G_0$ [37]. Data for the alkanes is given in Appendix Figure A.12, and reproduce well our previous results[7].

Thermoelectric current and conductance across a single-molecule junction is measured simultaneously by applying a thermal gradient across the junction using a Peltier heater to controllably heat the substrate to temperatures ranging from room temperature to about 60°C while maintaining the tip close to room temperature. The set-up is allowed to come to thermal equilibrium for about one hour before measurements are carried out. In all measurements reported here, the temperature difference (ΔT) between the tip and substrate is set to either 0 K or 14 K. In order to minimize the impact of unaccounted thermoelectric voltages across the leads, a pure gold wire (99.998%) of known thermopower ($S_{Au} = 2 \mu\text{V/K}$) was connected from the hot side of the Peltier to the cold side (which was held near room temperature), to provide electrical connectivity and so that the thermoelectric voltage across the reverse temperature gradient ($-\Delta T$) was fixed (see Figure 4.5(a) for schematic). We measure the thermopower by setting the applied bias to 0 V and measuring the thermoelectric current through the circuit.

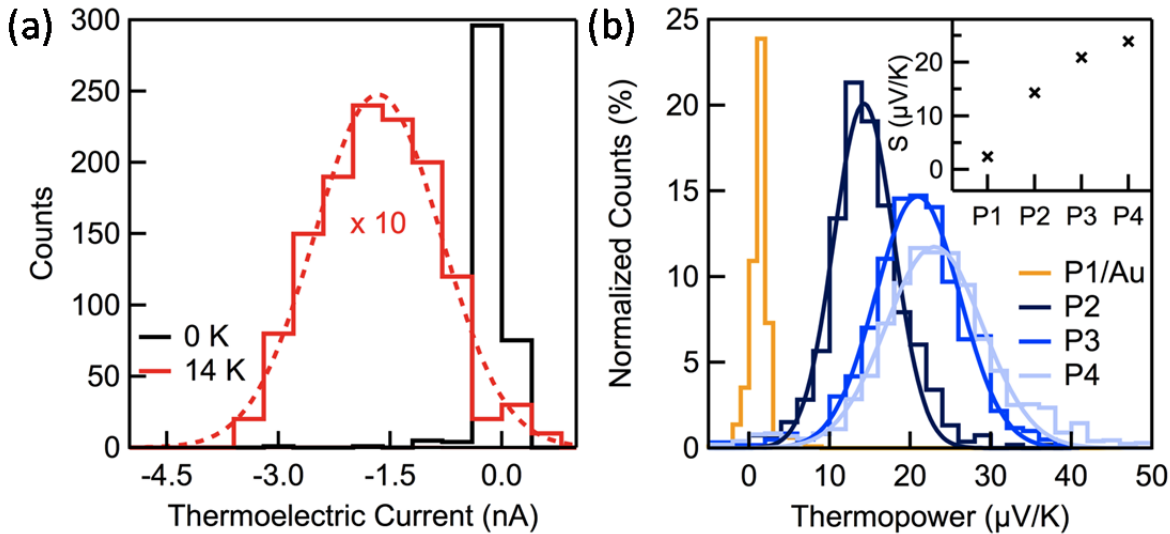


Figure 4.7: (a) Average thermoelectric current histograms for **P2** for $\Delta T=0$ K (black, 386 traces) and $\Delta T=14$ K (red, 129 traces). The histogram at $\Delta T=14$ K is multiplied by a factor of 10 and fit with a Gaussian (dotted line). (b) Histograms of thermopower for **P1/Au** (582 traces) and **P2** (530 traces), **P3** (629 traces), and **P4** (2,942 traces). Gaussians fits to the histograms are also shown. Inset: Molecular thermopower plotted as a function of number of phenyls in the molecular backbone.

The thermopower measurement works as follows. The Au STM tip is brought into contact with the heated Au substrate while applying a bias voltage of 10 mV until a conductance greater than $5 G_0$ is measured. The tip is then first retracted by 2.0 nm at a speed of ~ 16 nm/s, held fixed for 50 ms, and finally withdrawn an additional 1.6 nm. During part of the 50 ms hold section, we turn off the bias ($V=0$) and continue to measure the current. We collect thousands of such current-displacement curves and select the ones that sustained a molecular junction through the entire “hold” portion of the ramp (see Appendix Figure A.13)[19, 35]. We determine the average thermoelectric current for each such junction. The distributions of the average thermoelectric currents measured for **P2** are given in Figure 4.7(a) for $\Delta T = 0$ K (black, 386 traces), which is narrow and centered around 0 nA, and $\Delta T = 14$ K (red, 129 traces), which is broadened and peaked at -1.7 nA. Thermocurrent results from the other oligophenyl derivatives are given in Appendix Figure A.14.

Molecule	Conductance (G_0)	Thermopower ($\mu\text{V/K}$)	Power Factor (fW/K^2)
P1/Au	0.9	2.4	0.4
P2	1×10^{-1}	14.3	1.6
P3	1.4×10^{-2}	20.9	5×10^{-1}
P4	2×10^{-3}	23.9	9×10^{-2}
C6	1.4×10^{-2}	5.0	2.7×10^{-2}
C8	2×10^{-3}	5.6	5×10^{-3}
C10	3×10^{-4}	5.6	7×10^{-4}

Table 4.2: Experimental conductance (G), thermopower (S), and power factor (GS^2) for directly bonded junctions. The power factor for P2 is exceptionally high.

From the measured thermoelectric current, the thermopower of the single molecule junctions are calculated on a trace-by-trace basis ($S = I/G\Delta T$) and compiled into a histogram. The thermopower for all other molecules (**P1**, **P3**, **P4** and the three alkanes) were determined following the same procedure. Results from these measurements are given in Figure 4.7(b) for the oligophenyls and in Appendix Figure A.15 for the alkanes. For **P1** (yellow curve in Figure 4.7(b)), we cannot distinguish, on a trace-by-trace basis, the difference between a molecular junction and a gold single-atom contact as the conductance of **P1** ($0.9 G_0$) is too close to that of the Au contact ($1 G_0$). We also see the thermopower for these junctions is very similar, i.e. the distribution is peaked at $2.4 \mu\text{V/K}$, indicating that the thermopower of an Au $1 G_0$ junction is not very different from that of a **P1** junction. As the number of phenyl rings in the molecule is increased from 2 to 4, the center of the distributions of measured thermopower increases systematically. The values obtained for molecular conductance and thermopower using statistical fits to the data are given in Table 4.2 and are used to calculate the molecular power factor. We

note that the power factor for **P2** (1.6fW/K^2) is far higher than that of any other single molecule junction previously reported in literature due to its high conductance and relatively high thermopower. Measurements for the alkanes are carried out in a similar way and all data are summarized in Table 4.2. We find that the thermopower of the alkanes does not have a strong dependence on the chain length from C6 to C10.

Our measurements show that the conductance of these oligophenyls decreases exponentially with increasing length, while the thermopower increases non-linearly with increasing length. To rationalize these findings, we consider a series of models. In general, within the Landauer picture, the zero-bias conductance is proportional to the electron transmission through the junction, evaluated at the electrode Fermi energy, E_F . In the simplest description of non-resonant transmission through a single molecule, a single frontier orbital controls the transmission. The transmission function can then be described by a Lorentzian function centered at the energy of that molecular level, E_0 , with a width, Γ , that relates to the electronic coupling of the molecular state to the electrodes. The exponential decrease in conductance as a function of molecule length must be captured by varying the model parameters.[8] We use our conductance and thermopower data for all the oligophenyls from the experiments to determine the corresponding single-Lorentzian transmission curves. Results are shown in Appendix Figure A.16, where we see that we get un-physical parameters for E_0 and Γ . Specifically, the fit to experiment drives the backbone state to be pinned close to the Fermi energy, essentially independent of oligomer length.

To better understand trends in our conductance and thermopower data, we turn to tight-binding based model systems and calculate the conductances and thermopowers numerically using the Green's function approach[41-43]. We first consider a simple improvement to the

single-Lorentzian approximation discussed above that captures the length dependence explicitly. This tight-binding model (Model 1) assigns a single level to each phenyl ring and an electronic coupling (hopping parameter δ) between the rings. The terminal phenyls are coupled to the electrodes, as described by an imaginary self-energy $i\Gamma/2$, (see Appendix Figure A.17). The best fit-coefficients for the model are determined from experimental data as described in the SI. We find that this model tracks more closely the shift of the highest occupied molecular orbital towards the Fermi Energy yielding a transmission function where the resonances are fundamentally non-lorentzian for all molecules but **P1**, but predicts a strictly linearly increasing thermopower in contrast to what we see in the experiments.

For more insight to the electronic states in the junction, we examine results from calculations carried out using the Density-Functional Theory and Non-Equilibrium Green's Functions (DFT-NEGF) formalism[26, 44] with a gradient-corrected exchange-correlation functional[45]. The molecular junctions are described using a unit cell where each metallic layer consists of 16 atoms and the molecules are bound to a gold mound consisting of three atoms[37]. The junction geometry is first relaxed by minimizing the forces acting on all molecular and tip atoms, and subsequent transport calculations are performed using the optimized structures. An exemplary **P4** junction structure is shown in Figure 4.8(a). The DFT-calculated transmission spectra for **P1-P4** for an extended energy range are shown in Figure 4.8(b). The narrow peaks positioned a few eVs from the Fermi level correspond to the molecular backbone resonances. Low-bias conductance is however determined by the states representing the Au-C bonds. As visualized by the contour plot of the transmitted wave at the Fermi in Figure 4.8(b), electrons enter the molecule through a gateway state (a σ Au-C bonding orbital) and then tunnel through the backbone, as evidenced by the decaying amplitude in the plot.

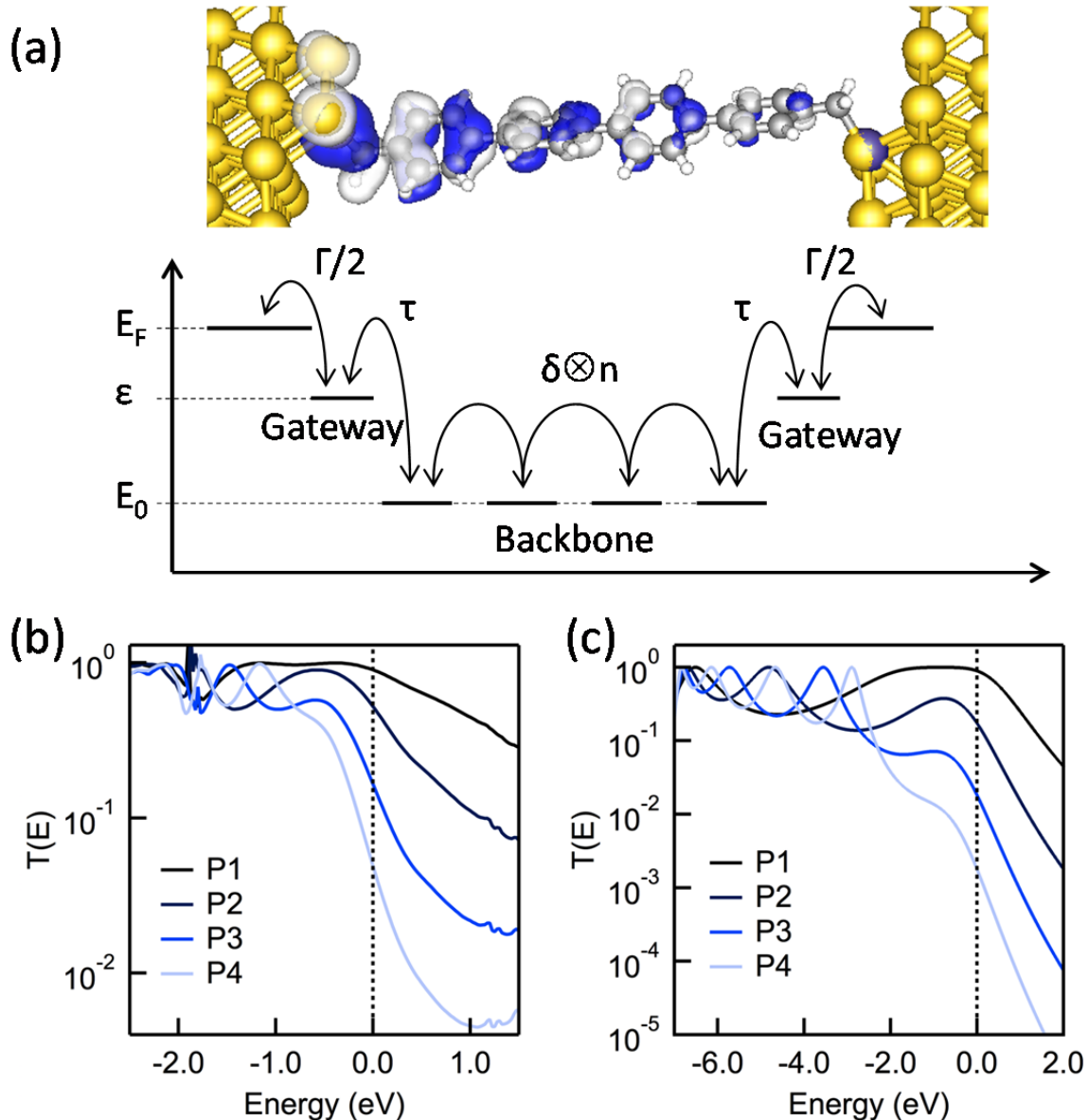


Figure 4.8: (a) Top: The optimized geometry of a **P4** junction with an isosurface plot of the scattering state at the Fermi energy. Bottom: Schematic diagram of the tight-binding model for **P4**. Transmission curves shown on a log scale for **P1-P4** (b) calculated using DFT and (c) as determined by the tight binding model using the best-fit parameters.

Returning to the transmission functions in Figure 4.8(b), near the Au-C bond orbital resonances, the gateway states on opposite sides couple via this tunneling, resulting in a double-peak structure, where the deeper- (shallowest-) energy peak is a bonding (anti-bonding) combination of the Au-C links.[7, 37] For **P1**, the coupling is strong resulting in distinct features

at -1.15 and -0.4 eV (**P1**), which merges into a single peak centered at \sim -0.6 eV for **P2-P4**. The tailing of these peaks to the Fermi level determines the low-bias conductance and thermopower of the **P1-P4** junctions. As shown in Figure 4.9(a), the conductance calculated with DFT is overestimated due to the known errors within DFT that tend to place the key orbital energies in transport calculations too close to the electrode Fermi energy.[46-52] The thermopower, Figure 4.9(b), is also overestimated and further, the calculation does not show saturation with length. Though, notice that, while $G(E_F)$ is dramatically overestimated for **P2-P4**, the overestimation in the calculated values of S is smaller.

Overall, the key and robust feature that emerges from the DFT-based calculations is the role of the gateway state. The gateway states can introduce a qualitatively different trade-off between conductance and thermopower. The essential point is apparent in the transmission functions in Figure 4.8(b) where the amplitude of the peak near -0.6 eV drops approximately exponentially while the width remains approximately constant. To the extent that the width is constant, the thermopower will also be constant, being proportional to a normalized energy derivative of the transmission function. Motivated by the DFT results, we consider a second model that consists of two gateway states that are tunnel coupled to each other through a length dependent parameter $\delta_n = \delta_0 e^{-\beta n/2}$ ($n=0$ is **P1** etc.) These gateway states also interact with the electrodes through an imaginary energy independent self-energy term $-i\Gamma/2$. The parameter β describes the decay of transmission in the long-molecule limit and is assumed to be energy independent. More generally, from the complex band structure calculations in the polymeric limit,[53] we can expect an energy dependent $\beta(E)$ with a semi-elliptic shape spanning the energy gap between the occupied and empty frontier orbital derived bands that control tunneling. Details and results from fitting this model (Model 2) are shown in see Appendix Figure A.18.

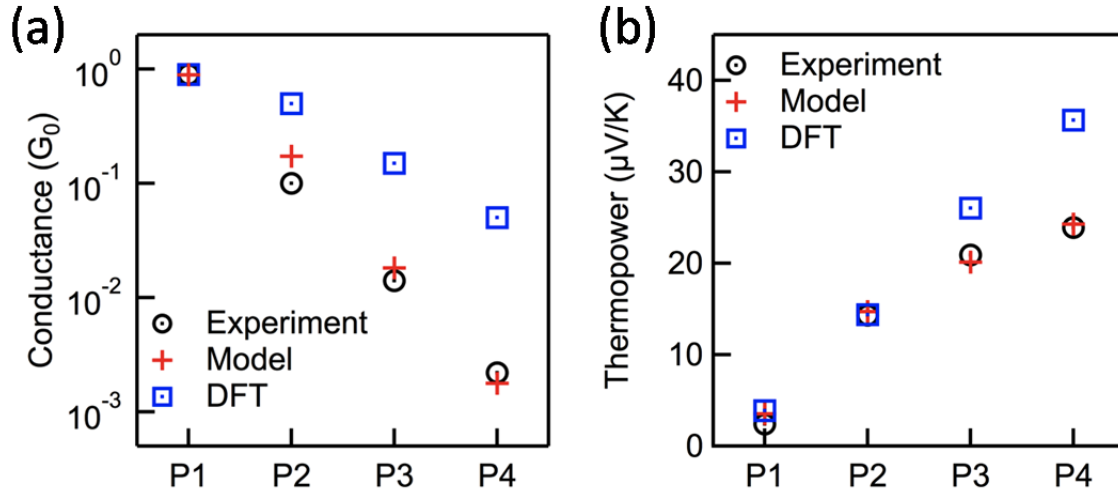


Figure 4.9: (a) Conductance values and (b) thermopower determined from the experiment, tight-binding model, and DFT as a function of the number of phenyl units in the chain.

This model comes closer to describing the data, but does not capture the exponential decay in conductance accurately as the value of β from the fit is found to be larger than what is measured in the experiment.[37] Furthermore, this model with an energy independent β yields a thermopower that saturates to $S_\infty = -\frac{\pi^2 k_B^2 T}{3e} \frac{\varepsilon}{4\varepsilon^2 + \Gamma^2}$ in the long-molecule limit. As detailed in the SI, with an energy dependent β , one would get an additional contribution to S proportional to $\frac{d\beta}{dE}$.

We improve on this by treating the backbone states explicitly while also including the gateway states in a tight-binding Hamiltonian as illustrated in Figure 4.8(a). This combines the physical elements of models 1 and 2 and naturally incorporates $\beta(E)$ valid for energies near the occupied backbone states. The two gateway states at energy ε couple respectively to the left and right electrodes through the self energy and they couple to a tight-binding chain that represents the essential frontier backbone orbitals with strength τ . The Hamiltonian for **P1** is a 3x3 matrix with no dependence on δ . The 4x4 matrix that represents the model Hamiltonian for **P2** is:

$$H\{\mathbf{P2}\} = \begin{bmatrix} \varepsilon - i\Gamma/2 & \tau & 0 & 0 \\ \tau & E_0 & \delta & 0 \\ 0 & \delta & E_0 & \tau \\ 0 & 0 & \tau & \varepsilon - i\Gamma/2 \end{bmatrix}$$

The Hamiltonians for **P3** and **P4** can be obtained by extending this matrix. The best-fit model transmission curves are given in Figure 4.8(c) for all four using (in eV with $E_F = 0$) $\varepsilon = -1.85$, $\Gamma = 2.86$, $E_0 = -4.47$, $\tau = -2.28$, $\delta = -1.27$. The transmission curves are qualitatively very similar to the results from the DFT-based calculations. As seen in Figure 4.9(a) and Figure 4.9(b), the model gives a robust account of both the exponential drop in conductance and the partial saturation in the thermopower, which could not be seen in any of the other models or from the DFT based calculations.

DFT-based calculations for the alkanes are summarized in the Appendix Figure A.19. The comparison to measured conductance and thermopower show the same trends as found for the **P1-P4** series. Furthermore, the transmission functions show the same key role for the Au-C gateway orbital. However, modeling the transmissions for these alkanes is not straightforward because the Fermi energy falls roughly halfway between the highest occupied and lowest unoccupied resonances.[53] Thus using just one molecular level for each methylene (as was done above for the oligophenyls) does not capture the conductance trends correctly. Introducing an unoccupied level into our model will introduce more parameters than can be constrained by the limited data set available from the experiments and is thus beyond the scope of this work. Going back to the simpler model with two gateway states that are tunnel coupled to each other, we see that we would observe a nearly constant thermopower in the limit of large n when $\frac{d\beta}{dE} \approx 0$, as will be the case for alkanes when the Fermi energy falls near mid-gap.[53]

In summary, we have measured the conductance and thermoelectric properties of oligophenyls and alkanes bound to the electrodes through direct, covalent Au-C links. The

highly-conducting nature of these links gives rise to exceptional thermoelectric properties and high values of the power factor, GS^2 , for the phenyl derivatives. A model for nanoscale transport in which only a single (HOMO-type) frontier backbone orbital is considered, either through a single Lorentzian or by a tight-binding model that explicitly accounts for backbone length, does not correctly predict the observed dependences in conductance or thermopower with length. Therefore, as motivated by the DFT calculations, we propose a modified tight-binding model to describe how transport is facilitated by a gateway Au-C state. This gateway-state is close in energy to the Fermi level and couples well into the molecular backbone, thereby dominating the zero-bias transmission properties of these molecules. For the alkanes, we find that conductance decreases exponentially while thermopower increases only modestly with the length of the molecule.

Acknowledgments

Overall project coordination, measurements and sample synthesis was supported as part of the Center for Re-Defining Photovoltaic Efficiency Through Molecular-Scale Control, an Energy Frontier Research Center funded by the U.S. Department of Energy (DOE), Office of Science, Office of Basic Energy Sciences under Award DE-SC0001085. Part of this work was carried out at the Center for Functional Nanomaterials, Brookhaven National Laboratory, which is supported by the U.S. Departement of Energy, Office of Basic Energy Sciences, under contract no. DE-AC02-98CH10886. H.V. and T.K. were supported through the Nanoscience and Engineering center by the New York State Office of Science, Technology, and Academic Research (NYSTAR). L.V. thanks the Packard Foundation for support.

4.3 References:

1. Nitzan, A. and M.A. Ratner, *Electron transport in molecular wire junctions*. Science, 2003. **300**(5624): p. 1384-1389.
2. Chen, F., X.L. Li, J. Hihath, Z.F. Huang, and N.J. Tao, *Effect of anchoring groups on single-molecule conductance: Comparative study of thiol-, amine-, and carboxylic-acid-terminated molecules*. Journal of the American Chemical Society, 2006. **128**(49): p. 15874-15881.
3. Venkataraman, L., J.E. Klare, I.W. Tam, C. Nuckolls, M.S. Hybertsen, and M.L. Steigerwald, *Single-Molecule Circuits with Well-Defined Molecular Conductance*. Nano Letters, 2006. **6**(3): p. 458 - 462.
4. Mishchenko, A., L.A. Zotti, D. Vonlanthen, M. Burkle, F. Pauly, J.C. Cuevas, M. Mayor, and T. Wandlowski, *Single-Molecule Junctions Based on Nitrile-Terminated Biphenyls: A Promising New Anchoring Group*. Journal of the American Chemical Society, 2011. **133**(2): p. 184-187.
5. Martin, C.A., D. Ding, J.K. Sorensen, T. Bjornholm, J.M. van Ruitenbeek, and H.S.J. van der Zant, *Fullerene-based anchoring groups for molecular electronics*. Journal of the American Chemical Society, 2008. **130**(40): p. 13198-13199.
6. Schneebeli, S.T., M. Kamenetska, Z. Cheng, R. Skouta, R.A. Friesner, L. Venkataraman, and R. Breslow, *Single-Molecule Conductance through Multiple $\pi-\pi$ -Stacked Benzene Rings Determined with Direct Electrode-to-Benzene Ring Connections*. Journal of the American Chemical Society, 2011. **133**(7): p. 2136-2139.
7. Cheng, Z.L., R. Skouta, H. Vazquez, J.R. Widawsky, S. Schneebeli, W. Chen, M.S. Hybertsen, R. Breslow, and L. Venkataraman, *In situ formation of highly conducting covalent Au-C contacts for single-molecule junctions*. Nature Nanotechnology, 2011. **6**(6): p. 353-357.
8. Malen, J.A., P. Doak, K. Baheti, T.D. Tilley, R.A. Segalman, and A. Majumdar, *Identifying the Length Dependence of Orbital Alignment and Contact Coupling in Molecular Heterojunctions*. Nano Letters, 2009. **9**(3): p. 1164-1169.
9. Reddy, P., S.Y. Jang, R.A. Segalman, and A. Majumdar, *Thermoelectricity in molecular junctions*. Science, 2007. **315**(5818): p. 1568-1571.
10. Baheti, K., J.A. Malen, P. Doak, P. Reddy, S.Y. Jang, T.D. Tilley, A. Majumdar, and R.A. Segalman, *Probing the chemistry of molecular heterojunctions using thermoelectricity*. Nano Letters, 2008. **8**(2): p. 715-719.

11. Malen, J.A., S.K. Yee, A. Majumdar, and R.A. Segalman, *Fundamentals of energy transport, energy conversion, and thermal properties in organic-inorganic heterojunctions*. Chemical Physics Letters, 2010. **491**(4-6): p. 109-122.
12. Dubi, Y. and M. Di Ventra, *Heat flow and thermoelectricity in atomic and molecular junctions*. Reviews of Modern Physics, 2011. **83**(1): p. 131-155.
13. Ashcroft, N.W. and N.D. Mermin, *Solid State Physics*. 1976: Cengage Learning.
14. Paulsson, M. and S. Datta, *Thermoelectric effect in molecular electronics*. Physical Review B, 2003. **67**(24): p. 241403.
15. Tan, A., J. Balachandran, S. Sadat, V. Gavini, B.D. Dunietz, S.-Y. Jang, and P. Reddy, *Effect of Length and Contact Chemistry on the Electronic Structure and Thermoelectric Properties of Molecular Junctions*. Journal of the American Chemical Society, 2011. **133**(23): p. 8838-8841.
16. Quek, S.Y.Q.S.Y., H.J. Choi, S.G. Louie, and J.B. Neaton, *Thermopower of Amine - Gold-Linked, Aromatic Molecular Junctions from First Principles*. ACS Nano, 2011. **5**(1): p. 551-557.
17. Quek, S.Y., H.J. Choi, S.G. Louie, and J.B. Neaton, *Length Dependence of Conductance in Aromatic Single-Molecule Junctions*. Nano Letters, 2009. **9**(11): p. 3949-3953.
18. Xu, B.Q. and N.J. Tao, *Measurement of single-molecule resistance by repeated formation of molecular junctions*. Science, 2003. **301**(5637): p. 1221-1223.
19. Widawsky, J.R., M. Kamenetska, J. Klare, C. Nuckolls, M.L. Steigerwald, M.S. Hybertsen, and L. Venkataraman, *Measurement of voltage-dependent electronic transport across amine-linked single-molecular-wire junctions*. Nanotechnology, 2009(43): p. 434009.
20. Blatt, F.J., *Thermoelectric Power of Metals*. 1976: Plenum Press, New York.
21. Quek, S.Y., L. Venkataraman, H.J. Choi, S.G. Loule, M.S. Hybertsen, and J.B. Neaton, *Amine-gold linked single-molecule circuits: Experiment and theory*. Nano Letters, 2007. **7**(11): p. 3477-3482.
22. Quek, S.Y., M. Kamenetska, M.L. Steigerwald, H.J. Choi, S.G. Louie, M.S. Hybertsen, J.B. Neaton, and L. Venkataraman, *Mechanically controlled binary conductance switching of a single-molecule junction*. Nature Nanotechnology, 2009. **4**(4): p. 230-234.
23. Butcher, P.N., *Thermal and electrical transport formalism for electronic microstructures with many terminals*. Journal of Physics: Condensed Matter, 1990. **2**(22): p. 4869.
24. Dubi, Y. and M. Di Ventra, *Thermoelectric Effects in Nanoscale Junctions*. Nano Letters, 2009. **9**(1): p. 97-101.

25. Parameswaran, R., J.R. Widawsky, H. Vazquez, Y.S. Park, B.M. Boardman, C. Nuckolls, M.L. Steigerwald, M.S. Hybertsen, and L. Venkataraman, *Reliable Formation of Single Molecule Junctions with Air-Stable Diphenylphosphine Linkers*. Journal of Physical Chemistry Letters, 2010. **1**: p. 2114-2119.
26. Soler, J.M., E. Artacho, J.D. Gale, A. Garcia, J. Junquera, P. Ordejon, and D. Sanchez-Portal, *The SIESTA method for ab initio order-N materials simulation*. Journal of Physics: Condensed Matter, 2002. **14**(11): p. 2745-2779.
27. Choi, H.J., L.C. Marvin, and G.L. Steven, *First-principles scattering-state approach for nonlinear electrical transport in nanostructures*. Physical Review B, 2007. **76**(15): p. 155420.
28. Martin, R., *Electronic structure: basic theory and practical methods*. 2004: Cambridge University Press.
29. Li, Z. and D.S. Kosov, *Nature of well-defined conductance of amine anchored molecular junctions*. Physical Review B, 2007. **76**(3): p. 035415.
30. Kamenetska, M., S.Y. Quek, A.C. Whalley, M.L. Steigerwald, H.J. Choi, S.G. Louie, C. Nuckolls, M.S. Hybertsen, J.B. Neaton, and L. Venkataraman, *Conductance and Geometry of Pyridine-Linked Single-Molecule Junctions*. Journal of the American Chemical Society, 2010. **132**(19): p. 6817-6821.
31. Majumdar, A., *Thermoelectricity in Semiconductor Nanostructures*. Science, 2004. **303**(5659): p. 777-778.
32. Snyder, G.J. and E.S. Toberer, *Complex thermoelectric materials*. Nat Mater, 2008. **7**(2): p. 105-114.
33. Kushvaha, S.S., W. Hofbauer, Y.C. Loke, S.P. Singh, and S.J. O'Shea, *Thermoelectric measurements using different tips in atomic force microscopy*. Journal of Applied Physics, 2011. **109**(8): p. 084341-7.
34. Tan, A., J. Balachandran, B.D. Dunietz, S.-Y. Jang, V. Gavini, and P. Reddy, *Length dependence of frontier orbital alignment in aromatic molecular junctions*. Applied Physics Letters, 2012. **101**(24): p. 243107-5.
35. Widawsky, J.R., P. Darancet, J.B. Neaton, and L. Venkataraman, *Simultaneous Determination of Conductance and Thermopower of Single Molecule Junctions*. Nano Letters, 2012. **12**(1): p. 354-358.
36. Khobragade, D., E.S. Stensrud, M. Mucha, J.R. Smith, R. Pohl, I. Stibor, and J. Michl, *Preparation of Covalent Long-Chain Trialkylstannyl and Trialkylsilyl Salts and an Examination of their Adsorption on Gold*. Langmuir, 2010. **26**(11): p. 8483-8490.

37. Chen, W., J.R. Widawsky, H. Vázquez, S.T. Schneebeli, M.S. Hybertsen, R. Breslow, and L. Venkataraman, *Highly Conducting π -Conjugated Molecular Junctions Covalently Bonded to Gold Electrodes*. Journal of the American Chemical Society, 2011. **133**(43): p. 17160-17163.
38. Li, C., I. Pobelov, T. Wandlowski, A. Bagrets, A. Arnold, and F. Evers, *Charge transport in single Au vertical bar alkanedithiol vertical bar Au junctions: Coordination geometries and conformational degrees of freedom*. Journal of the American Chemical Society, 2008. **130**(1): p. 318-326.
39. Park, Y.S., A.C. Whalley, M. Kamenetska, M.L. Steigerwald, M.S. Hybertsen, C. Nuckolls, and L. Venkataraman, *Contact chemistry and single-molecule conductance: A comparison of phosphines, methyl sulfides, and amines*. Journal of the American Chemical Society, 2007. **129**(51): p. 15768-15769.
40. Kamenetska, M., M. Koentopp, A. Whalley, Y.S. Park, M. Steigerwald, C. Nuckolls, M. Hybertsen, and L. Venkataraman, *Formation and Evolution of Single-Molecule Junctions*. Physical Review Letters, 2009. **102**(12): p. 126803.
41. Nitzan, A., *Electron transmission through molecules and molecular interfaces*. Annual Review of Physical Chemistry, 2001. **52**: p. 681-750.
42. Hybertsen, M.S., L. Venkataraman, J.E. Klare, A.C. Whalley, M.L. Steigerwald, and C. Nuckolls, *Amine-linked single-molecule circuits: systematic trends across molecular families*. Journal of Physics: Condensed Matter, 2008. **20**(37): p. 374115.
43. Datta, S., *Electronic Transport in Mesoscopic Systems*. 1995: Cambridge University Press.
44. Brandbyge, M., J.L. Mozos, P. Ordejon, J. Taylor, and K. Stokbro, *Density-functional method for nonequilibrium electron transport*. Physical Review B, 2002. **65**(16): p. 165401.
45. Perdew, J.P., K. Burke, and M. Ernzerhof, *Generalized gradient approximation made simple*. Physical Review Letters, 1996. **77**(18): p. 3865-3868.
46. Toher, C., A. Filippetti, S. Sanvito, and K. Burke, *Self-interaction errors in density-functional calculations of electronic transport*. Physical Review Letters, 2005. **95**(14): p. 4.
47. Evers, F., F. Weigend, and M. Koentopp, *Conductance of molecular wires and transport calculations based on density-functional theory*. Physical Review B, 2004. **69**(23): p. -.
48. Neaton, J.B., M.S. Hybertsen, and S.G. Louie, *Renormalization of molecular electronic levels at metal-molecule interfaces*. Physical Review Letters, 2006. **97**(21): p. 216405.

49. Ke, S.H., H.U. Baranger, and W.T. Yang, *Role of the exchange-correlation potential in ab initio electron transport calculations*. Journal of Chemical Physics, 2007. **126**(20): p. 201102.
50. Sai, N., M. Zwolak, G. Vignale, and M. Di Ventra, *Dynamical corrections to the DFT-LDA electron conductance in nanoscale systems*. Physical Review Letters, 2005. **94**(18).
51. Thygesen, K.S. and A. Rubio, *Conserving GW scheme for nonequilibrium quantum transport in molecular contacts*. Physical Review B, 2008. **77**(11).
52. Thygesen, K.S. and A. Rubio, *Renormalization of Molecular Quasiparticle Levels at Metal-Molecule Interfaces: Trends across Binding Regimes*. Physical Review Letters, 2009. **102**(4): p. 046802.
53. Tomfohr, J.K. and O.F. Sankey, *Complex band structure, decay lengths, and Fermi level alignment in simple molecular electronic systems*. Physical Review B, 2002. **65**(24): p. 245105.

Chapter 5

Measurement of Molecular I-V Characteristics

The work described in this chapter was done in collaboration with Jennifer Klare, who performed the chemical synthesis, from Prof. Colin Nuckolls's group. The theoretical contributions were made by Mark Hybertsen and Michael Steigerwald. Also, thanks to Masha Kamenetska for helping to run the experiments. Here, I developed the measurement and analysis techniques and completed the STM work.

Conductance and thermopower measurements can only provide a partial description of electron transport through molecules, for they are only able to probe characteristics of the transmission function at the Fermi energy. In order to obtain more information about the transmission function, we can also perform large bias measurements of molecular current-voltage (I-V) curves. Assuming that the coupling to the electrodes is symmetric, the form of I-V curve is given by

$$I(V) = \frac{2e}{h} \int_{-\infty}^{+\infty} d\omega T(\omega, T) [f(\omega + eV/2) - f(\omega - eV/2)]$$

where $f(E) = \left[\exp\left(-\frac{E}{kT}\right) + 1 \right]^{-1}$ is the Fermi-Dirac distribution of current carriers in the leads and ω is the integration parameter with units of energy. Since smoothing of the bias window edges at room temperature is negligible, this equates to the current being proportional to the area under the transmission curve when opening a symmetric bias window of $\pm V/2$ about the Fermi energy.

In this chapter, we explore the electronic and physical effects of applying a large bias to a molecular junction system. We observe an inherent difference in the response of electron/LUMO-conducting junctions and hole/HOMO-conducting junctions and investigate the mechanism behind this. Also, we see that the degree of non-linearity of the IV curves depends on the proximity of the conducting orbital to the Fermi energy of the electrodes.

5.1 Measurement of Voltage Dependent Electronic Transport Across Amine-Linked Single Molecular Wire Junctions*

Abstract

We measure the conductance and current-voltage characteristics of two amine-terminated molecular wires – 4,4'-Diaminostilbene and Bis-(4-aminophenyl)acetylene – by breaking Au point-contacts in a molecular solution at room temperature. Histograms compiled from thousands of measurements show a slight increase in the molecular junction conductance (I/V) as the bias is increased to nearly 450 mV. Comparatively, similar conductance measurements made with 1,6-Diaminohexane, a saturated molecule, demonstrates almost no bias dependence. We also present a new technique to measure a statistically defined current-voltage curve. Application to all three molecules shows that 4,4'-Diaminostilbene exhibits the largest increase in differential conductance as a function of applied bias. This indicates that the predominant transport channel for 4,4'-Diaminostilbene (the highest occupied molecular orbital) is closer to the Fermi level of the metal than that of the other molecules, consistent with the trends observed in the molecular ionization potential. We find that junctions constructed with the conjugated molecules show greater noise in individual junctions and less structural stability on average at biases greater than 450 mV. In contrast, junctions formed with the alkane can sustain a bias of up to 900 mV. This significantly affects the statistically averaged IV characteristic measured for the conjugated molecules at higher bias.

Introduction

Understanding charge transport across metal-molecule-metal junctions could lead to the development of nanoscale devices with functionality that can be tuned chemically[1]. It is thus important to fully understand the mechanisms behind charge transport across single molecule junctions. In the last decade, the characterization of the electronic properties of single molecule junctions has been studied extensively by different methods [2-11]. These have focused both on measuring the low bias conductance of a molecular junction as well as the current-voltage

* J. R. Widawsky, M. Kamenetska, J. Klare, C. Nuckolls, M. L. Steigerwald, M. S. Hybertsen, and L. Venkataraman, **Nanotechnology**, 20, 434009 (2009).

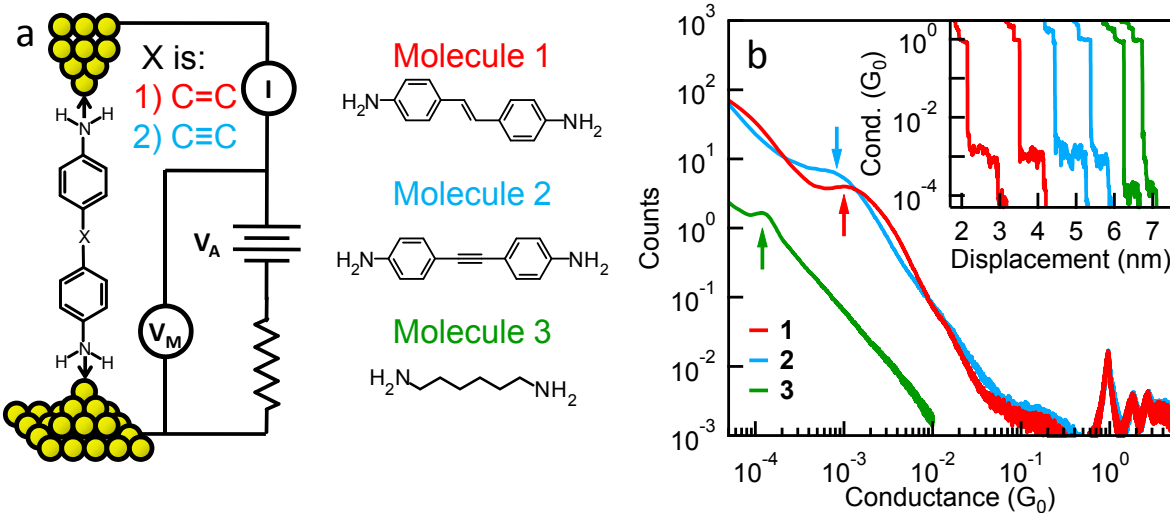


Figure 5.1: (a) Schematic of experimental set-up: V_A is the applied bias voltage, I is the measured current and V_M is the voltage measured across the junction. The ~ 100 k Ω series resistor is also shown. Structures of all three molecules are also shown. The N-N lengths of these molecules are about 1.2 nm, 1.3 nm and 0.9 nm for 1, 2, and 3 respectively. The molecules bind to the gold leads through the lone pair of the amines, represented here by arrows. (b) Normalized conductance histograms for all three molecules measured with a bias $V_M = 45$ mV and a 1mM solution of the molecules in 1,2,4-Trichlorobenzene. A linear bin size of $10^{-5} G_0$ is used for 1 and 2 (showing molecular peak and conductance quantum peaks), and a bin size of $10^{-6} G_0$ is used for 3. The peaks, determined using Lorentzian fits (or Lorentzian fit with background subtraction for 2), are marked with arrows. Inset: Sample measured traces for each of the three molecules showing the molecular conductance steps. All traces except for the extreme left trace have been offset horizontally to the right for clarity.

characteristics under applied voltages up to the 1 V range or larger. However, in practice, it is often hard to confirm that a single molecule is actually bridging the metal electrodes, as well as the structural stability of the molecular conformation, while the current is measured as a function of voltage. Furthermore, a detailed understanding of these properties requires the measurement of a statistically significant number of junctions. As a result, experiments that directly correlate molecular structure and current-voltage characteristics remain challenging.

Here, we investigate the conductances of two short amine-linked molecular wires: 4,4'Diamino-stilbene (**1**), which consists of two benzene rings with a vinyl bridge (C=C), and Bis-(4-aminophenyl)acetylene (**2**), which is similar but with an ethynyl bridge (C≡C) and compare them to that of 1,6-Hexanediamine (**3**). The molecular structures are illustrated in

Figure 5.1(a). These molecules bind to gold metal electrodes through an electronically selective donor-acceptor bond formed between the N-lone pair on the terminal amine link groups and an under-coordinated gold atom [12]. We present a new measurement technique to probe the single molecule junction differential conductance as a function of applied bias voltage. We find that at a bias of about 400 mV, the differential conductance of **1** increases the most, the differential conductance of **2** increase modestly, while **3** shows almost no bias dependence. Since transport in these amine-linked molecules is mediated through the highest occupied molecular orbital (HOMO) [13], these results indicate that the HOMO for **1** is closest to the metal Fermi level. Furthermore, we find that molecular junctions of **1** and **2** become unstable at a higher bias, while **3** can sustain a bias of up to about 900 mV. This suggests that the amine-Au bond can sustain a high bias. However, the partial charging of the resonant level supporting transport in steady state at higher bias, as suggested by the proximity of the HOMO to the Au Fermi level in **1** and **2**, acts to weaken the donor-acceptor bond.

Experimental Method

We form single molecule junctions by breaking a gold point-contact in a solution of the molecules[6], and measure the conductance while pulling the junction apart at a constant speed of 16 nm/s. Molecule **1** was obtained from Astatech (97% purity), molecule **2** was synthesized as described earlier[14], and molecule **3** was obtained from Sigma-Aldrich (>99% purity). Details of our experimental set-up have been described previously[14]. Briefly, we use a home-built modified Scanning Tunneling Microscope (STM), designed with only z-axis mobility. The STM tip is a high-purity (5N) gold wire (Alfa Aesar), 0.025 inches in diameter, cut on an angle to be sharp. The STM substrate consists of 100 nm of gold thermally evaporated onto mica, which

was cleaned under UV/Ozone prior to use. The measurements are carried out at room temperature, in ambient conditions. We measure the current (I) through the tip-substrate junction using a current amplifier. In the measurements described here, we place a $100\text{ k}\Omega$ resistor in series with our tip-substrate junction to limit the voltage drop across the junction when its resistance is very low (Figure 5.1(a)). A bias (V_A) is applied across the junction and series resistor. We measure the bias (V_M) across the tip-substrate junction and determine the conductance ($G = I/V_M$) by dividing the measured current with the measured voltage.

For single molecule junction current-voltage measurements (I-V), the STM tip is brought into contact with the Au substrate until a conductance of greater than a few G_0 is obtained at an applied bias of about 50 mV. The tip is then withdrawn by 2.4 nm at 16 nm/s. This distance is chosen to ensure that the gold point-contact is broken by the end of this elongation, a prerequisite for forming a molecular junction. At this point, the tip-substrate distance is held constant for about 150 milliseconds. During this “hold” period, the V_A is ramped sinusoidally for one period and the current is measured. At the end of this ramp, V_A is set to 50 mV once again and the tip is withdrawn an additional 2.4 nm to fully break the junction.

Results and Discussions

We first measure the conductance of the three molecules in separate experiments at a low bias ($V_M \sim 45\text{ mV}$) from $\sim 1\text{mM}$ solutions of the compounds in 1,2,4-Trichlorobenzene (Sigma-Aldrich, >99% purity). The inset of Figure 5.1(b) shows sample conductance traces measured with each of the three molecules, showing steps at integer multiples of $G_0 = 2e^2/h = 77.5\text{ }\mu\text{S}$, the quantum of conductance, and at a molecule dependent value below G_0 . In Figure 5.1(b), we show conductance histograms constructed from thousands of consecutively measured traces with

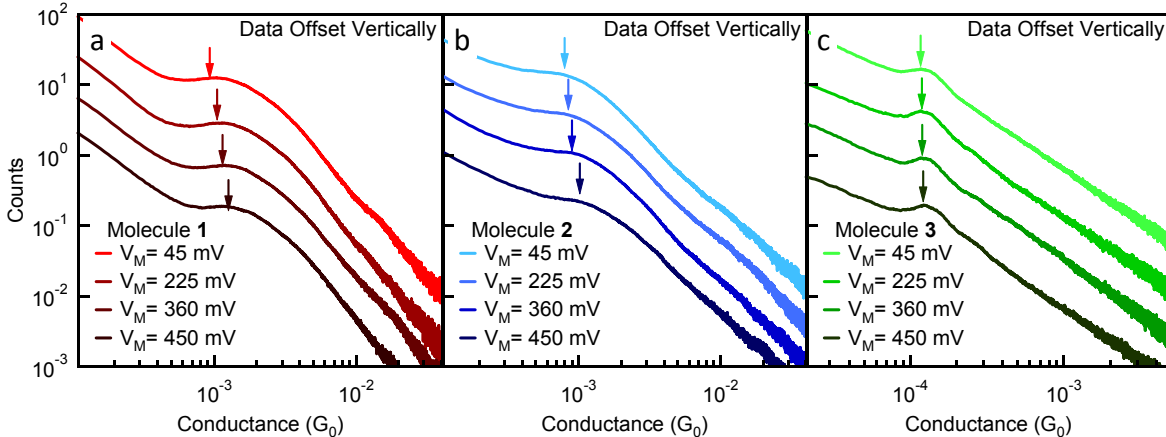


Figure 5.2: Linearly-binned normalized conductance histograms constructed from over 5000 traces without data selection for (a) **1**, (b) **2**, and (c) **3** measured at four different bias voltages, V_M . The peak locations are tracked by the arrows. Note: The histograms have been offset vertically for clarity.

each molecule at $V_M \sim 45$ mV. A histogram measured in solvent alone has no features over this conductance range. By using Lorentzian fits to the peaks (or a Lorentzian fit with a power law background for **2**), we are able to extract the most-probable conductance value for each molecule. We see a peak centered at about $1.0 \times 10^{-3} G_0$, $0.8 \times 10^{-3} G_0$, and $1.2 \times 10^{-4} G_0$ for molecules **1**, **2** and **3** respectively consistent with previous results[14]. For **2**, we need to subtract a power-law background because the peak is broad, probably due to the soft rotation barrier about the $C \equiv C$ bridge[14, 15]. To determine the bias dependence of these conductance histograms, we measure conductance traces at different constant biases. For each molecule, four different biases ranging from $V_M \sim 45$ mV to 450 mV were used and between five and ten thousand conductance (I/V_M) traces were compiled for each molecule at each bias to give the conductance histograms. Results of these bias dependent measurements are shown in Figure 5.2, where the peak of the conductance histogram, indicated by the arrows, shifts to higher conductance with increasing bias for **1** and **2**, as opposed to **3** where there is almost no change in the peak position.

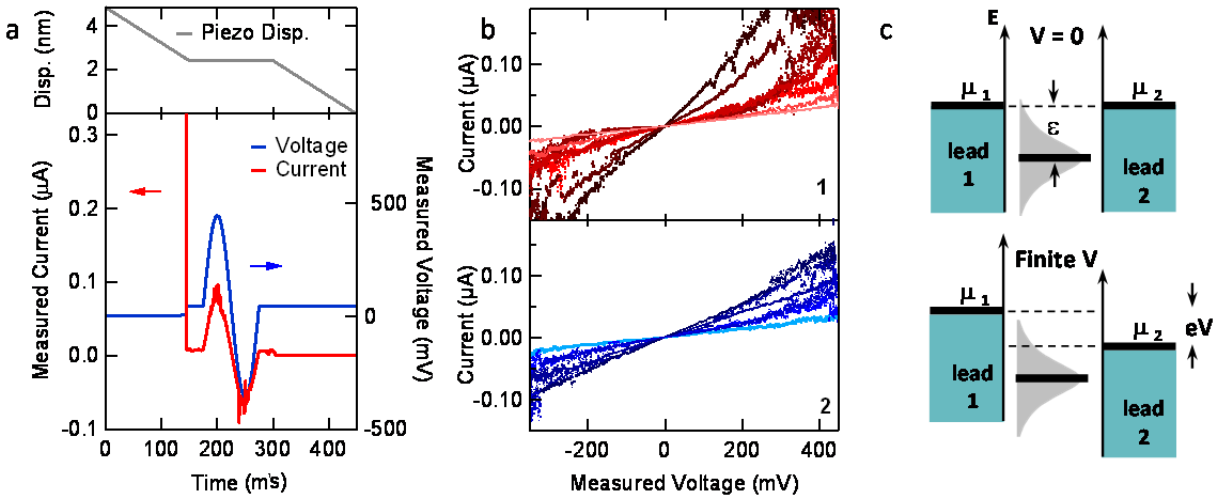


Figure 5.3: (a) Sample trace measured during a voltage sweep for molecule 1. The piezo displacement (grey line) is shown in the upper panel. The measured current (red, left axis) and voltage (blue, right axis) are shown in the bottom panel. Note that the voltage is very low when the junction conductance is low due to the series resistor. (b) Multiple sample current-voltage traces for molecules 1 (upper panel) and 2 (lower panel). These traces are obtained from the middle section of the voltage sweep, with V_M starting at +450 mV and ending at -350 mV and are chosen to illustrate the variety in measured traces. (c) Schematic level alignment diagram for two different biases showing the change in charge transfer (extent of grey shaded region within the bias window) between the molecule and metal at a large applied bias.

These measurements give average conductance (I/V) versus applied bias; to measure the differential conductance (dI/dV) of these molecules as a function of applied bias, we first construct a statistically significant I-V curve for each molecule as follows. We measure thousands of I-V curves on single molecule junctions while holding the relative tip-sample displacement fixed as described in the Experimental Methods section. A sample measured trace for molecule 1 is shown in Figure 5.3(a) to illustrate the method, showing the piezo displacement, the measured current (I) and measured bias (V_M) when a bias ramp of about ± 450 mV is applied. Thousands of such I-V_M traces were measured with each molecule. We further analyzed only those traces for which the conductance just before and just after the voltage ramp was within the peak seen in the respective conductance histograms shown in Figure 5.1(b). These were selected using an automated algorithm. We found that about 15-25% of the measured traces had a molecule bridging the tip and the substrate during the “hold” section for molecules 1 and 2,

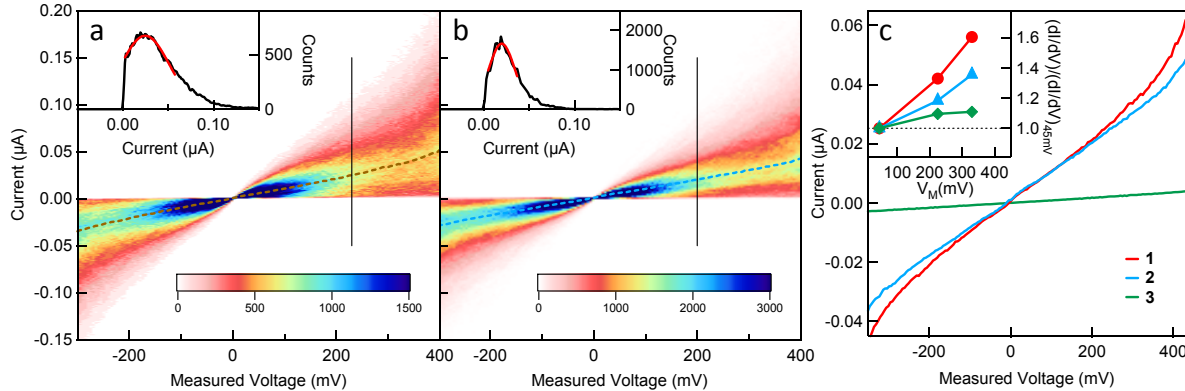


Figure 5.4: (a) and (b) Two-dimensional current-voltage histogram for **1** and **2** made from about 4500 and 6000 individual $I-V_M$ traces, respectively. The current bin size is 0.5nA and the voltage bin size is 5 mV . A vertically cross-section (black line) is displayed in the inset. The upper part is fitted with a Gaussian (red curve) in order to extract the peak location. (c) I-V curves for **1** (red), **2** (blue) and **3** (green) determined from the peak locations of the cross-sections at all voltage bins, like those shown in the insets of (a) and (b). The curves represent the most frequently measured current as a function of bias voltage. Inset: Relative differential conductance (dI/dV) for **1**, **2**, and **3** normalized to the respective differential conductance values at $V_M = 45 \text{ mV}$. These are obtained from the slopes of the linear fits to the IV curves in a small voltage interval about each voltage.

although about 95% of our conductance versus displacement traces had a molecule. Thus some junctions broke within the initial 2.4 nm extension, some did not break until after the 150 ms “hold” section, and some junctions did not sustain the bias ramp, bringing down the total number of successful $I-V_M$ measurements. In our measurements with molecule **3**, only 5% of the measurements resulted in successful $I-V_M$ traces, even though about 85% of the traces had a molecule bridging the tip and substrate. In Figure 5.3(b), we show sample $I-V_M$ traces for molecule **1** and **2**, where we can see that the current increases through the junction with increasing bias. These $I-V_M$ curves were chosen to illustrate the variety in measured $I-V_M$ curves. We find that $I-V$ traces for molecule **1** are much noisier at high bias than those for molecule **2** or **3**. A possible reason for this will be discussed below.

The selected $I-V_M$ data were then used to construct a two-dimensional histogram of current versus voltage. Such histograms, obtained for **1** from about 4500 $I-V_M$ traces and for **2** from about 6000 traces, are shown in Figure 5.4(a) and Figure 5.4(b). An analogous histogram

was also constructed for **3** but is not shown here. We fit Gaussians to vertical sections at each voltage bin of the histogram (as demonstrated in the insets of Figure 5.4(a) and Figure 5.4(b)) to track the peak in the current distribution as a function of voltage. These correspond to the most frequently measured current at each bias voltage for all molecular junctions. The peak position is traced with the dotted curves shown in Figure 5.4(a) and Figure 5.4(b). The resulting I-V_M measurements of **1**, **2** and **3** are shown in Figure 5.4(c) (solid lines). We determine the differential conductance for all three molecules by taking the slope of these I-V_M curves at a few fixed bias values. The inset of Figure 5.4(c) shows the differential conductance (dI/dV) normalized to its value at 45 mV (dI/dV_{45mV}). We can see that the dI/dV of **1** shows the largest increase with applied bias, that of **2** shows a small increase, while **3** shows almost no bias dependence.

Two factors control the conductance of these single molecule junctions in the non-resonant tunneling regime: (1) the position of the dominant transport channel, the HOMO[13, 16-18], relative to the metal Fermi level, and (2) the coupling of the HOMO level to the metal resulting in a level broadening (Figure 5.3(c)). Both could be different for different molecules. The net effect of these two factors determines the tunnel coupling across the junction. Using a density functional theory (DFT) based approach [19, 20], we have previously shown that the trends in the tunnel coupling can be determined by modeling the electronic structure of a single under-coordinated Au atom bonded to each side of the junction [14]. In particular, the tunnel coupling for **1** is found to be about 20% larger than that for **2**. The position of the HOMO relative to the Fermi level can only be determined from a full transmission calculation including corrections for correlation effects beyond DFT [16]. Such calculations are beyond the scope of this paper. However, we have previously measured the effect of substituents on the conductance

of benzenediamine[13]. Electron withdrawing substituents reduced conductance while electron donating substituents increased conductance. Electron withdrawing groups lower the molecular orbital energies (increase ε in Figure 5.3(c)), and the opposite holds for electron donating groups. The conductance results are only consistent with the HOMO being closest to the Fermi energy and mediating the tunneling conductance. These trends were understood using a vertical ionization potential calculation for the substituted species. Subsequent full transmission calculations for benzenediamine confirmed that the HOMO was the sole channel responsible for low bias conductance, with an estimated separation $\varepsilon \approx 3$ eV, including corrections to DFT orbital energies, and a half-width of about 0.5 eV[16, 18]. Calculations for amine linked alkanes show an even larger separation [17].

For the three molecules under study here, we calculated the vertical ionization potential with a triple zeta basis (including polarization and diffuse functions) and found them to be 6.11 eV, 6.25 eV, and 7.67 eV for **1**, **2** and **3** respectively. For reference, the calculated value for benzenediamine is 6.83 eV. The DFT calculations moderately underestimate diamine ionization potentials[13], as also observed for other aromatics [21] but represent the trends. The calculations clearly suggest that the molecular wires (**1** and **2**) should have the HOMO level closer to the electrode Fermi energy than benzenediamine, but not by enough to reach the resonant tunneling regime for the bias ranges under study here. However, as the sketch in Figure 5.3(c) illustrates, proximity to the resonance can lead to enhanced differential conductance. The calculated ionization potentials suggest a larger increase in the differential conductance of **1** compared with **2** at elevated bias. However, the magnitude of the effect observed at 400 mV bias suggests that a more complete transmission calculation will be required for full understanding. On the other hand, the relatively constant differential conductance for the alkane

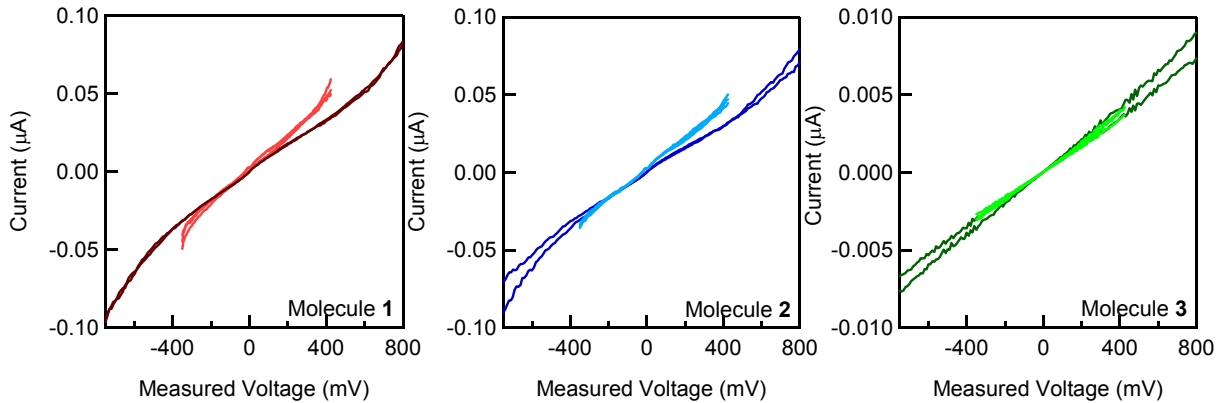


Figure 5.5: Average IV curves determined from 2D $I-V_M$ histograms using a small ramp (± 450 mV) or large ramp (± 900 mV) for all three molecules. Each averaged IV curve is determined from one tip/sample pair and two or three such data sets are superposed for each molecule and ramp value. Variations in the IV curves from the small and large bias ramps are larger for **1** and **2** than the variations.

3 with bias is consistent with the HOMO derived resonance remaining substantially outside the bias window.

To probe this further, we performed similar I-V measurements by applying a bias ramp of about ± 900 mV to all three molecules. Two-dimensional histograms of the selected $I-V_M$ measurements were created and the most frequently measured current versus voltage curves were determined for all three molecules, as described in detail above. We found that the fraction of traces where molecule **1** or **2** bridged the tip-substrate gap was about 10% with the ± 900 mV ramp compared with 15%-25% for the ± 450 mV ramp. This implies that fewer junctions could sustain a ± 900 mV applied bias. For molecule **3** there was no significant difference in the trapping probability with the two different ramps. In Figure 5.5, we compare $I-V_M$ curves for all three molecules with both bias ramps. We see that the $I-V_M$ curves for **1** and **2** have a lower average conductance (I/V_M) with the ± 900 mV ramp when compared with the ± 450 mV ramp. Since these measurements represent the most frequently measured current at each voltage, they imply that for **1** and **2**, the types of junctions measured differ between the two ramps; junctions

with a higher average conductance cannot sustain a bias of about 900mV. In contrast, for **3**, the I-V curves are almost identical. This suggests a correlation between the conductance of an individual junction and stability of the junction under higher applied bias.

One physical explanation for such a correlation would be variations in the proximity of the HOMO to the electrode Fermi energy. Larger conductance corresponds to larger overlap of the HOMO derived transmission resonance to the electrode Fermi energy, resulting in an increased charge transfer from the molecular HOMO to the metal (Figure 5.3(c)). As the applied bias is increased, the portion of the resonance in the bias window increases resulting in more charge transfer. Thus for **1** and **2**, which have a smaller HOMO-LUMO gap, we expect a larger charge transfer between the electrode and the molecules, while for **3**, which has a very large HOMO-LUMO gap, we do not expect a significant change in this charge transfer. There are two donor-acceptor bonds that hold the diamine in place between the emerging Au tips; we hypothesize that this charge redistribution, while it may strengthen one of these bonds, must weaken the other. This weakening of one bond could result in noisier IV curves, as we find experimentally. Furthermore, the cleavage of this weaker link destroys the molecular junction.

The extent to which this bias-dependent charge transfer strongly correlates with conductance could account for the differences observed between low and high applied bias range in both noise level in individual IV characteristics of individual junctions and the changes in the averaged IV curves. Molecule **1** has the highest conductance, and thus a molecular level closest to the Fermi level when comparing these three molecules. We expect a greater charge transfer in molecular junctions with **1**. Experimentally, this would result in noisier IV curves due to a decrease in the N-Au bond strength, as well as a smaller ability to sustain higher biases (decreasing number of successful IV measurements.) Molecule **2** would show similar trend,

though the extent of charge transfer would be smaller as it is less conducting, and therefore has a HOMO level that is not as close to Fermi. For **3**, which has a very large HOMO-LUMO gap, we do not expect a significant change in transfer when comparing an applied bias of 0.4 V or 0.8 V, consistent with the experiment. We also note that while the N lone pair on the amine link group remains highly localized for the alkanes, it is significantly coupled to the π system (HOMO) for **1** and **2**, further supporting a connection between charge removal from the HOMO and bond strength in these cases.

Conclusions

We have presented an new technique to measure statistically averaged current-voltage characteristics of single molecule junctions and have applied this technique to measure the differential conductance of 4,4'-Diaminostilbene (**1**) and Bis-(4-aminophenyl)acetylene (**2**) single molecule junctions as a function of bias voltage. We find that both molecules show an increase in differential conductance as a function of applied bias, in contrast to measurements of 1,6-Diaminohexane (**3**). This is consistent with trends in the ionization potential for the three molecules. We further find that junctions with **1** and **2** show significant increases in noise and reductions in stability at applied biases above about 450 mV, while junctions with **3** remain stable to a bias voltage of 900 mV. This significantly affects the statistically averaged IV characteristics at high applied bias for **1** and **2**.

Acknowledgments

This work was supported in part by the NSF-NSEC (award # CHE-0641523), by NYSTAR, the American Chemical Society under the Petroleum Research Fund and Columbia University RISE

award. This work was supported in part by the DOE (DE-AC02-98CH10886). LV thanks NSF Career Award CHE- 0744185 and the David and Lucille Packard Foundation.

5.2 References

1. Aviram, A. and M.A. Ratner, *Molecular Rectifiers*. Chemical Physics Letters, 1974. **29**(2): p. 277-283.
2. Reed, M.A., C. Zhou, C.J. Muller, T.P. Burgin, and J.M. Tour, *Conductance of a molecular junction*. Science, 1997. **278**(5336): p. 252-254.
3. Park, J., A.N. Pasupathy, J.I. Goldsmith, C. Chang, Y. Yaish, J.R. Petta, M. Rinkoski, J.P. Sethna, H.D. Abruna, P.L. McEuen, and D.C. Ralph, *Coulomb blockade and the Kondo effect in single-atom transistors*. Nature, 2002. **417**(6890): p. 722-725.
4. Liang, W.J., M.P. Shores, M. Bockrath, J.R. Long, and H. Park, *Kondo resonance in a single-molecule transistor*. Nature, 2002. **417**(6890): p. 725-729.
5. Reichert, J., R. Ochs, D. Beckmann, H.B. Weber, M. Mayor, and H. von Lohneysen, *Driving current through single organic molecules*. Physical Review Letters, 2002. **88**(17): p. 176804.
6. Xu, B.Q. and N.J. Tao, *Measurement of single-molecule resistance by repeated formation of molecular junctions*. Science, 2003. **301**(5637): p. 1221-1223.
7. Dadash, T., Y. Gordin, R. Krahne, I. Khivrich, D. Mahalu, V. Frydman, J. Sperling, A. Yacoby, and I. Bar-Joseph, *Measurement of the conductance of single conjugated molecules*. Nature, 2005. **436**(7051): p. 677-680.
8. Emanuel, L., B.W. Heiko, and R. Heike, *Statistical Approach to Investigating Transport through Single Molecules*. Physical Review Letters, 2007. **98**(17): p. 176807.
9. Wu, S.M., M.T. Gonzalez, R. Huber, S. Grunder, M. Mayor, C. Schonberger, and M. Calame, *Molecular junctions based on aromatic coupling*. Nature Nanotechnology, 2008. **3**(9): p. 569-574.
10. Martin, C.A., D. Ding, H.S.J. van der Zant, and J.M. van Ruitenbeek, *Lithographic mechanical break junctions for single-molecule measurements in vacuum: possibilities and limitations*. New Journal of Physics, 2008. **10**: p. 065008.
11. Blum, A.S., J.G. Kushmerick, S.K. Pollack, J.C. Yang, M. Moore, J. Naciri, R. Shashidhar, and B.R. Ratna, *Charge Transport and Scaling in Molecular Wires*. Journal of Physical Chemistry B, 2004. **108**(47): p. 18124-18128.
12. Venkataraman, L., J.E. Klare, I.W. Tam, C. Nuckolls, M.S. Hybertsen, and M.L. Steigerwald, *Single-Molecule Circuits with Well-Defined Molecular Conductance*. Nano Letters, 2006. **6**(3): p. 458 - 462.

13. Venkataraman, L., Y.S. Park, A.C. Whalley, C. Nuckolls, M.S. Hybertsen, and M.L. Steigerwald, *Electronics and Chemistry: Varying Single Molecule Junction Conductance Using Chemical Substituents*. Nano Letters, 2007. **7**(2): p. 502-506.
14. Hybertsen, M.S., L. Venkataraman, J.E. Klare, A.C. Whalley, M.L. Steigerwald, and C. Nuckolls, *Amine-linked single-molecule circuits: systematic trends across molecular families*. Journal of Physics: Condensed Matter, 2008. **20**(37): p. 374115.
15. Li, Y.W., J.W. Zhao, X. Yin, H.M. Liu, and G.P. Yin, *Conformational analysis of diphenylacetylene under the influence of an external electric field*. Physical Chemistry Chemical Physics, 2007. **9**(10): p. 1186-1193.
16. Quek, S.Y., L. Venkataraman, H.J. Choi, S.G. Loule, M.S. Hybertsen, and J.B. Neaton, *Amine-gold linked single-molecule circuits: Experiment and theory*. Nano Letters, 2007. **7**(11): p. 3477-3482.
17. Kamenetska, M., M. Koentopp, A. Whalley, Y.S. Park, M. Steigerwald, C. Nuckolls, M. Hybertsen, and L. Venkataraman, *Formation and Evolution of Single-Molecule Junctions*. Physical Review Letters, 2009. **102**(12): p. 126803.
18. Quek, S.Y., H.J. Choi, S.G. Louie, and J.B. Neaton, *Length Dependence of Conductance in Aromatic Single-Molecule Junctions*. Nano Letters, Submitted, 2009.
19. Jaguar, *Jaguar v7.5*, Schrodinger, L.L.C., New York, NY 2008.
20. Perdew, J.P., K. Burke, and M. Ernzerhof, *Generalized gradient approximation made simple*. Physical Review Letters, 1996. **77**(18): p. 3865-3868.
21. Kadantsev, E.S., M.J. Stott, and A. Rubio, *Electronic structure and excitations in oligoacenes from ab initio calculations*. Journal of Chemical Physics, 2006. **124**(13): p. 134901.

Chapter 6

Conclusions

6.1 Summary and Scientific Impact

I have discussed the electronic and thermoelectric conduction properties of single molecule junctions, measured using the scanning tunneling microscope break junction technique. Employing this technique has enabled us to investigate fundamental quantum transport physics in an effort to further advance the development of viable molecular electronic devices. The work presented here has contributed to the growing wealth of knowledge concerning transport at the nanometer length scale and helped to facilitate a greater understanding of the transfer of charge across interfaces and quantum mechanical systems. It has also provided a foundation on which future studies can be built.

After explaining how the STM-BJ method was performed, we described a new way to construct highly conducting single molecule junctions through the use of *in situ* chemistry. This led to the formation of junctions with effectively no contact resistance and therefore the observed conductances were one to two orders of magnitude higher than that of their equivalents made with more common linkers. The best of the series, a derivative of xylene, exhibited a conductance close to the quantum of conductance G_0 , indicative of a near resonant transport mechanism. DFT calculations showed that conduction through these directly bonded junctions is mediated by the Au-C bond, which serves as a gateway state between the electrode and the molecular backbone. This notion was explored further by measurement of junction thermopower and with a tight binding model posed to reproduce the experimentally observed trends. The presence of the gateway state caused a non-linear increase in thermopower with molecular length. Furthermore, because of their special conduction properties, these highly conducting junctions displayed exceptionally high power factors when compared with other values of single molecule power factor both here and in literature.

Thermopower measurements have also allowed us to assess the validity of the single level model for transport. In the case of HOMO-conducting, amine-linked junctions, the d-state of the gold electrode introduced a non-Lorentzian feature into the transmission curve, which caused the estimation of the frontier orbital alignment to the Fermi level to be inaccurate when compared with DFT-based calculations. A pyridine-linked junction, on the other hand, as a consequence of being a LUMO conductor, is not impacted by this gold state, therefore making a Lorentzian transmission function a reasonable approximation. The properties of amine-linked junctions were also investigated by performing finite bias experiments, in which we saw that applying a large bias tended to weaken one of the bonds and cause junction breakdown. We also observed that the degree of non-linearity of the I-V curves depends on the proximity of the conducting orbital to the Fermi energy of the electrodes.

We probed transport across different molecular backbones by studying transmission through a silicon chain. We observed that their electronic properties more closely resembled the family of oligoenes as opposed to their direct organic analogs, fully saturated alkanes; their decay of conductance with length for the series was comparatively more shallow. We also observed a break in the “sigma-conjugation” of the silane when the backbone reached lengths of five atoms and longer.

6.2 Outlook

While much work has been done to investigate the transport properties of molecular junctions, there remains to be a wide range of related studies that could be performed to better understand these systems. First, the mechanism behind the cleavage of the trimethyltin end groups continues to be an unanswered question. There were dozens of tin-terminated molecules that were run in the STM-BJ setup that did not show any direct evidence for *in situ* cleaving of the end groups. A detailed study of the chemical reaction of the molecule with gold atoms could lead to more reliable formation of the directly-bonded junctions. Perhaps related to that, knowing the toxicity of tin radicals, finding an alternative end group that either cleaves spontaneously or needs a chemical or physical catalyst to cleave would be a worthwhile improvement.

We saw that the tight binding approach accurately models the thermopower of polyphenyl derivatives, but there are other, more complicated physical processes that the model ignores. This includes the energy correction due to image charge effects. Perhaps this is why the model does not seem to explain the alkane thermoelectric data too well. The DFT transmission curves for the alkanes contain a resonance/antiresonance feature between the backbone resonances and Au-C bond state that directly influences their low-bias properties. This probably results from a parallel pathway for transmission, either into or across the backbone. Furthermore, in other, more weakly bound systems, like the series of amine-terminated benzenes, where the d-state of the gold electrode is clearly visible in the transmission, a more sophisticated transmission model should be applied to accurately reproduce the results.

Lastly, we have used single molecule transport measurements to probe the properties of the transmission function near the Fermi level generally in three different ways – low bias

conductance measurements, thermopower, and molecular I-V curves. When focusing on junctions with truly Lorentzian transmission curves, the location of the molecular resonance as predicted by each of the three methods is inconsistent, especially when coupled with DFT calculations. Due to their inherent nonlinearity, fitting the molecular I-V curves always underestimates the gap between the Fermi level and molecular orbital. The underestimation may be the result of a bias-dependent Stark shift, the mechanism behind which is still unknown. Some possible causes might be, but are not necessarily limited to, the polarizability of the junction, bond strengthening/weakening in the presence of an electric field, or current-induced changes in molecular confirmation (a quinoidal resonance effect on a polyphenyl, for example).

These studies and others would help us gain further insight into how charge transport works at the quantum level. Creating molecular junctions using the STM-BJ technique is just one of the many, current approaches to study quantum transport, and others will be discovered in the future. But nonetheless, STM-BJ has proven to be a valuable and widely-used tool in investigating nanoscale conduction. However, there remains to be plenty of unanswered questions when it comes to the field of molecular electronics, not just concerning transport physics, but across multiple disciplines, including synthetic chemistry, electrical and computer engineering, and others. Ultimately, building viable molecular technologies will take a collaborative effort between experts with a variety of different backgrounds.

6.3 Complete List Published Work

- J. R. Widawsky, W. Chen, H. Vazquez, T. Kim, R. Breslow, M. S. Hybertsen, L. Venkataraman, '*Length-Dependent Thermopower of Highly Conducting Au-C Bonded Single Molecule Junctions*' submitted.
- P. Darancet, J. R. Widawsky, H. J. Choi, L. Venkataraman, J. B. Neaton '*Quantitative Current-Voltage Characteristics in Molecular Junctions from First Principles*', **Nano Letters**, 12, 6250–6254, (2012).
- R. Klausen, J. R. Widawsky, M. L. Steigerwald, L. Venkataraman, C. Nuckolls, '*Conductive Molecular Silicon*', **J. Am. Chem. Soc.**, 134, 4541–4544, (2012)
- J. R. Widawsky, P. Darancet, J. B. Neaton, L. Venkataraman, '*Simultaneous Determination of Conductance and Thermopower of Single Molecule Junctions*', **Nano Letters**, 12, 354–358, (2012).
- W. Chen, J. R. Widawsky, H. Vázquez, S. T. Schneebeli, M. S. Hybertsen, R. Breslow, L. Venkataraman, '*Highly Conducting Pi-Conjugated Molecular Junctions Covalently Bonded to Gold Electrodes*', **J. Am. Chem. Soc.** 133, 17160–17163 (2011).
- M. Kamenetska, M. Dell'Angela, J. R. Widawsky, G. Kladnik, A. Verdini, A. Cossaro, D. Cvetko, A. Morgante, L. Venkataraman, '*Structure and Energy Level Alignment of Tetramethyl Benzenediamine on Au(111)*', **J. Phys. Chem. C**, 111, 12625-12630, (2011).
- Z-L Cheng, R. Skouta, H. Vazquez, J. R. Widawsky, S. Schneebeli, W. Chen, M. S. Hybertsen, R. Breslow, L. Venkataraman, '*In situ Formation of Highly Conducting Au-C Contacts for Single Molecule Junctions*', **Nature Nanotechnology** 6, 353-357, (2011).
- B. M. Boardman, J. R. Widawsky, Y. S. Park, L. Venkataraman, M. L. Steigerwald, C. Nuckolls, '*Conductance of Single-Cobalt Chalcogenide Cluster Junctions*', **J. Am. Chem. Soc.** 133, 8455–8457, (2011).
- R. Parameswaran, J. R. Widawsky, H. Vazquez, Y. S. Park, B. M. Boardman, C. Nuckolls, M. L. Steigerwald, M. S. Hybertsen, L. Venkataraman, '*Reliable Formation of Single Molecule Junctions with Air-Stable Diphenylphosphine Linkers*', **J. Phys. Chem. Lett.**, 1, 2114-2119 (2010).
- J. R. Widawsky, M. Kamenetska, J. Klare, C. Nuckolls, M. L. Steigerwald, M. S. Hybertsen, L. Venkataraman, '*Electronic Transport Across Single Molecular Wire Junctions: Voltage Dependence of Conductance*', **Nanotechnology**, 20, 434009 (2009).
- Y. S. Park, J. R. Widawsky, M. Kamenetska, M. L. Steigerwald, M. S. Hybertsen, C. Nuckolls, L. Venkataraman, '*Frustrated Rotations in Single Molecule Junctions*', **J. Am. Chem. Soc.** 131, 10820-10821 (2009).

Appendix

A.1 Supplementary Information for Section 3.1

The conductance of each molecule was measured using the STM-based break-junction technique, where an Au tip (Alfa Aesar, 99.999%) cut to be sharp is perpendicularly brought in and out of contact with a substrate of ~100 nm of gold (Alfa Aesar, 99.999%) evaporated onto cleaved mica disks. The substrate is mounted on a piezoelectric positioner (Mad City Labs), so that sub-angstrom resolution in position is achieved. During the entire break junction procedure, a small, constant bias (25-250 mV) is applied between the tip and the substrate while the current is measured (Keithley 428-Prog). Piezo control and data collection was performed using a National Instruments PXI Chassis System (with PXI-4461, PXI-6289) at 40 kHz and driven and managed with a custom-program using Igor Pro (Wavemetrics, Inc.).

The experimental set-up is kept under ambient conditions. For each experiment, the substrate is cleaned under UV/Ozone for 15 minutes prior to use. For every conductance trace measurement, the STM tip is first brought into hard contact with the substrate to achieve a conductance greater than $\sim 10 G_0$. At this point, the junction electrodes are pulled apart at a speed of 15 nm/s for 0.25 seconds. Conductance is measured as a function of tip-sample displacement to generate conductance traces. For each tip/substrate pair, at least one set of 1,000 traces of clean gold breaks is collected to ensure the system is clean. Then, the target molecule, dissolved in 1,2,4-trichlorobenzene (~10 mM) is deposited and over 10,000 conductance traces are collected for each of the molecules reported here. To determine the conductance of a molecule, every trace is binned linearly into conductance bins, without any data selection, and compiled into a single conductance histogram. The resultant peak in the histogram gives the most frequently measured value of molecular conductance. Every molecule was measured using multiple tip/substrate pairs, on different days to check for consistency and reproducibility.

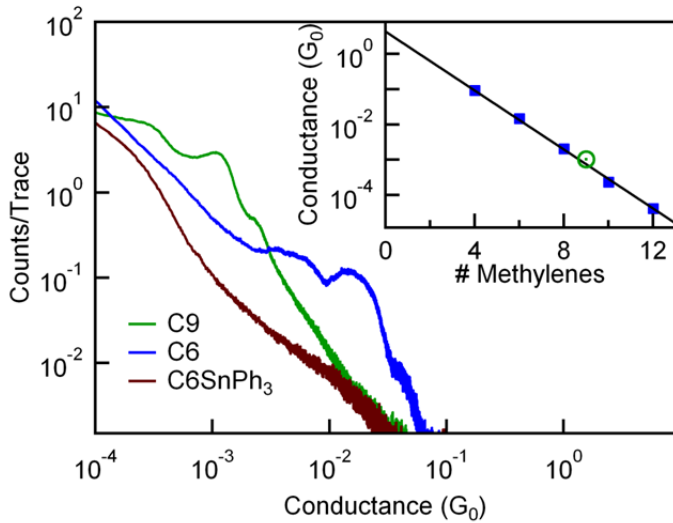


Figure A.1: Conductance histograms for **C6SnPh₃**, **C6** and **C9**, generated from over 15000 conductance traces, without any data selection. Histogram bin size is $10^{-5}G_0$. Inset: Conductance histogram peak position versus number of methylene groups for all data in Figure 3.1(d) and for **C9** (green circle).

Control Experiments: A series of control molecules were measured to reinforce the notions of SnMe₃ cleavage and the direct formation of direct Au-C bonds.

1. **1,9-bis(trimethylstannyl)nonane (C9):** To eliminate the possibility of odd/even effects, 1,9-bis(trimethylstannyl)nonane (**C9**) was synthesized and measured. The conductance histogram and peak position for **C9** is shown in Figure A.1 where we see no unusual odd/even effects.
2. **1,6-bis(triphenyltin)-hexane (C6SnPh₃):** A tri-phenylated, rather than tri-methylated, version of **C6** was also synthesized (1,6-bis(triphenyltin)-hexane (**C6SnPh₃**)). The histogram for this molecule is also shown in Figure A.1. We see no molecular peak, indicating that the steric bulk of the phenyl groups blocks the formation of molecular junctions, probably by inhibiting the accessibility of the Sn-C bond to the gold atoms on the electrode. As comparison, the conductance histogram for C6 is also included.
3. **Additional Experiments With 1,4-bis(trimethylstannyl) benzene (Ph):** Measurement of **Ph** did not show molecular plateaus during the first 2.5 hrs of measurements. In order

to determine whether or not the reaction was triggered by the applied voltage, we introduced the ~1mM solution into the experimental set-up with the tip and substrate at equipotential (grounded) and waited for 3 hours before starting the measurements. We found conductance plateaus appeared immediately, indicating that a bias was not required during the wait period. This implies that the reaction is not voltage induced, but rather just stems from exposure of the target molecules to the gold surface. Second, we found that the length of the wait period depends weakly on the concentration of the solution. When increasing the concentration of the solution by about 2 orders of magnitude, the waiting period decreased by only about half. This reaffirms that the mechanism behind the reaction is indeed surface chemistry, which means that exposure of the target molecule to the gold surface is essential to causing the transformation that facilitates measurement of conductance.

Data Analysis: In order to determine the percent of traces with steps, the following procedure was used. First, conductance cutoffs were designated using the conductance histograms for each molecule. The cutoffs were chosen to properly window the conductance peak (see example for **C6** in Figure A.2(a)).

The number of points in the conductance window was then counted for each trace, yielding a value for an equivalent molecular step length. If a particular trace has a step that is longer than 0.01 nm within the conductance window, we counted these traces as having a molecular plateau. For **C4**, 15% of all measured traces showed a conductance plateau. For **C6**, which is a slightly longer molecule, 30% of the traces showed a conductance plateau. The percentage of traces with **C8** plateaus when measuring the **C4** solution is about 50%, while a

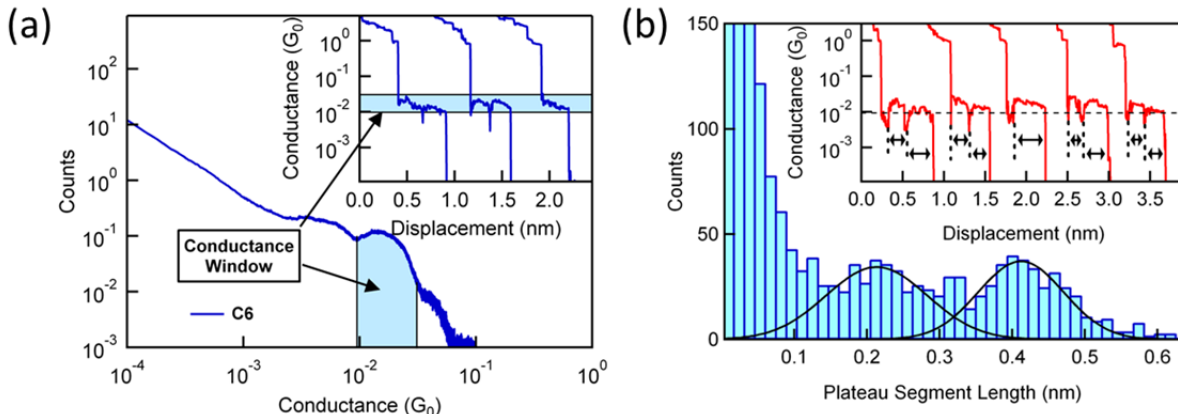


Figure A.2: (a) Conductance histogram for **C6** showing the peak region highlight the conductance window used to determine traces with conductance plateaus. Inset: Conductance window shown for sample traces. (b) Histogram of the length of continuous plateau segments for **C6**. A total of 2682 plateau segments were determined from the selected 700 traces. Inset: Sample conductance traces showing individual segments.

solution initially composed of **C8** yields 60%. The longer molecules, such as **C10** and **C12**, exhibit an almost 100% capture rate.

Many traces with molecular plateaus for **C6-C12** show dips to lower conductance value, as shown in Figure 3.1(b). In contrast to molecular steps observed with amine-terminated or methylsulfide-terminated alkanes which are relatively flat and featureless, the molecular steps here show systematic dips at 2-2.5 Å length intervals as the junction is elongated. To determine these length intervals, we select traces that have plateaus that are longer than 4 Å. From the 16000 traces measured with **C6**, about 4800 had a molecular plateau, but only about 700 had a plateau longer than 4 Å. After selecting this sub-set of 700 traces, we determined the length of each of the continuous segments within the entire molecular plateau (the distance between the dips) designated by the conductance window shown in Figure A.2(a). In Figure A.2(b), we plot a histogram of these continuous segment lengths. Two clear peaks are visible in this histogram indicating that continuous plateau lengths are around multiples of 2.1 Å. As the length of the target molecule increases, the number of dips during each molecular step generally increases.

A.2 Supplementary Information for Section 3.2

The conductance of each molecule was measured using the STM-based break-junction technique, where an Au tip (Alfa Aesar, 99.999%) cut to be sharp is perpendicularly brought in and out of contact with a substrate of ~100 nm of gold (Alfa Aesar, 99.999%) evaporated onto cleaved mica disks. The substrate is mounted on a piezoelectric positioner (Mad City Labs), so that sub-angstrom resolution in position is achieved. During the entire break junction procedure, a small, constant bias (25-250 mV) is applied between the tip and the substrate while the current is measured (Keithley 428-Prog). Piezo control and data collection was performed using a National Instruments PXI Chassis System (with PXI-4461, PXI-6289) at 40 kHz and driven and managed with a custom-program using Igor Pro (Wavemetrics, Inc.).

The experimental set-up is kept under ambient conditions. For each experiment, the substrate is cleaned under UV/Ozone for 15 minutes prior to use. For every conductance trace measurement, the STM tip is first brought into hard contact with the substrate to achieve a conductance greater than $\sim 10 G_0$. At this point, the junction electrodes are pulled apart at a speed of 15 nm/s for 0.25 seconds. Conductance is measured as a function of tip-sample displacement to generate conductance traces. For each tip/substrate pair, at least one set of 1,000 traces of clean gold breaks is collected to ensure the system is clean. Then, the target molecule, dissolved in 1,2,4-trichlorobenzene (~10 mM) is deposited and over 10,000 conductance traces are collected for each of the molecules reported here. To determine the conductance of a molecule, every trace is binned linearly into conductance bins, without any data selection, and compiled into a single conductance histogram. The resultant peak in the histogram gives the most frequently measured value of molecular conductance. Every molecule was measured using multiple tip/substrate pairs, on different days to check for consistency and reproducibility.

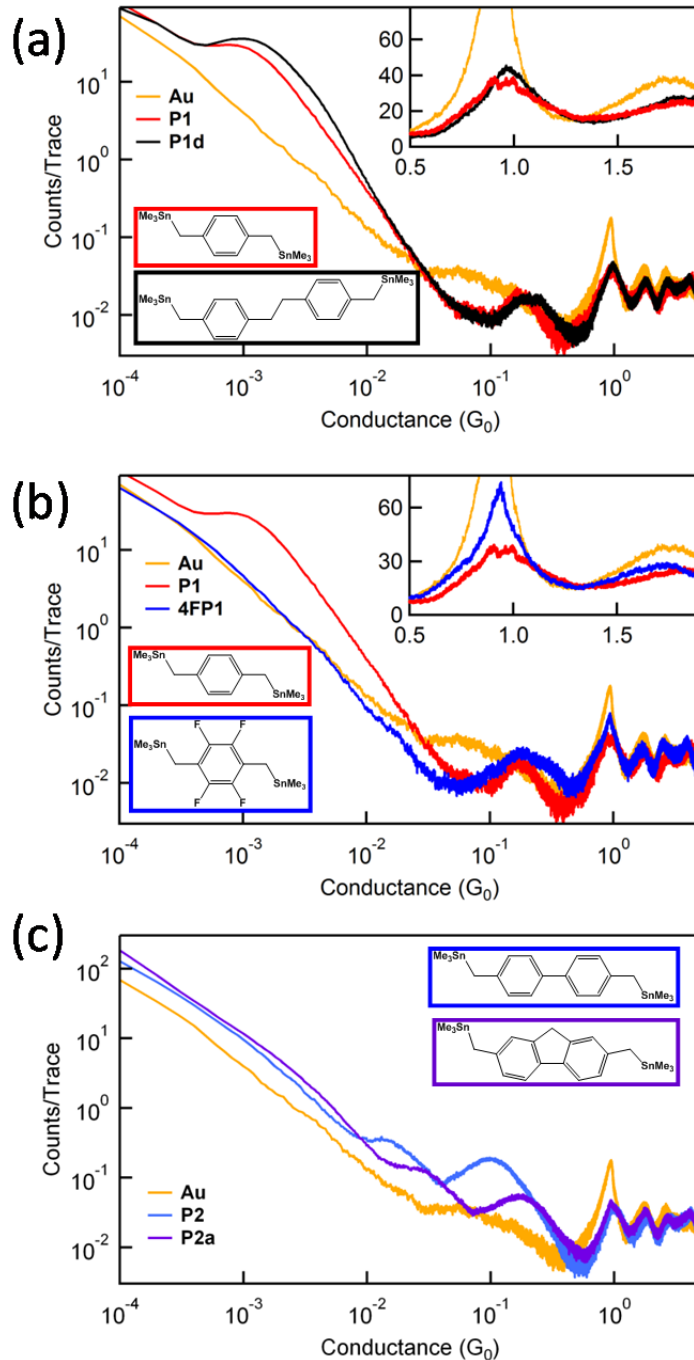


Figure A.3: (a) Conductance histograms from measurements of **P1** and **P1d** at a 25 mV bias. (b) Conductance histograms from measurements of **P1** and **4FP1** at a 25 mV bias. (c) Conductance histograms from measurements of **P2** and **P2a** at a 250 mV bias.

Additional Data: Conductance histograms from additional measurements – all histograms are generated from over 10000 measurements without any data selection.

A.3 Supplementary Information for Section 3.3

General Procedure and Instrumentation: Single molecule conductance measurements were performed using a home-built modified Scanning Tunneling Microscope (STM). A hand-cut 0.25 mm diameter gold wire (99.998%, Alfa Aesar) was used as the STM tip. The substrate was a gold-coated (99.999%, Alfa Aesar) mica surface. Sub-angstrom level control of the tip-substrate distance was achieved using a commercially available single-axis piezoelectric positioner (Nano-P15, Mad City Labs). The STM was controlled using a custom program using IgorPro (Wavemetrics, Inc.). All of the experiments were conducted at room temperature in ambient conditions.

In the STM-Break Junction technique, the tip is repeatedly brought in and out of contact with the substrate, while a constant bias is applied and current is measured. Immediately after the contact breaks, a target molecule in the vicinity can bridge the gap so that its conductance ($G=I/V$) can be measured. The target molecules were introduced in solution form (~1mM in 1,2,4-Trichlorobenzene) and tens of thousands of conductance vs. displacement traces were obtained at 40kHz for each molecule studied so that a statistical analysis of the data can be achieved. In general, a bias of 225mV was used to measure molecular conductance, except in the cases of the **Si4** and **Si5**, which was measured with a bias of 350 mV. Conductance histograms were constructed without any sort of data selection.

Control Experiments: Several control molecules were independently measured to preclude contaminants in the conductance apparatus or analyte solutions and to ensure that the junction are formed as a direct result of the thiomethyl end groups. For the conductance histograms of these molecules, see the Figure A.4. None show a significant conductance peak.

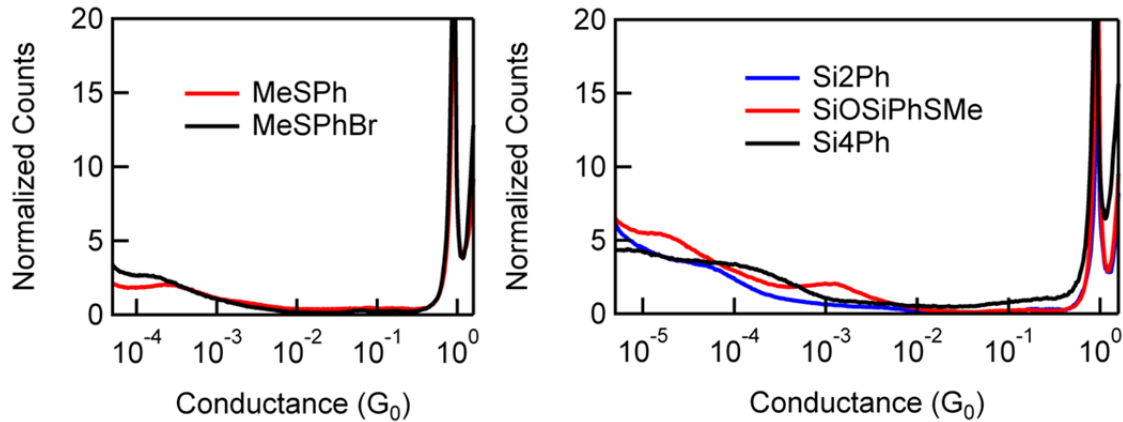


Figure A.4: Conductance histograms for several control molecules shown with logarithmic binning. None show a significant conductance peak in the measurable range of conductance. The molecules include the synthetic precursors as well as possible linkerless/oxidized products.

(1a) thioanisole (**MeSPh**), (1b) 4-bromothioanisole (**MeSPhBr**), (2a) diphenyltetramethyldisilane (**Si2Ph**), (2b) siloxane (**SiOSiPhSMe**), (2c) diphenyloctamethyltetrasilane (**Si4Ph**).

4-Bromothioanisole (**MeSPhBr**) is the precursor for the aryl lithiate employed in the synthesis of silanes **Si1–5** and thioanisole (**MeSPh**) is the product of hydrolysis of that aryl lithiate. These two compounds are intermediates common to all four silanes assayed. We measured the conductance of these molecules to determine if trace impurities could be responsible for the length-independent conductance peak at $\sim 10^{-3} G_0$. The lack of conductance signal in the histogram above suggests that these possible contaminants in the analyte solution are not responsible for the conductance results observed. We also investigated silanes lacking methyl sulfide link groups (**Si2Ph** and **Si4Ph**) to determine if junction formation is still possible (either due to direct Au-Si bonds through cleaving of the phenyl groups or bonding of the phenyl rings directly to the gold). The lack of a conductance signal suggests that Au does not make direct contacts to aryl-capped silanes, confirming the necessity of SMe groups for junction formation. Lastly, to determine if *in situ* oxidation of the silane chain has an effect on the conductance results, we measured the conductance of a siloxane variant (**SiOSiPhSMe**). No

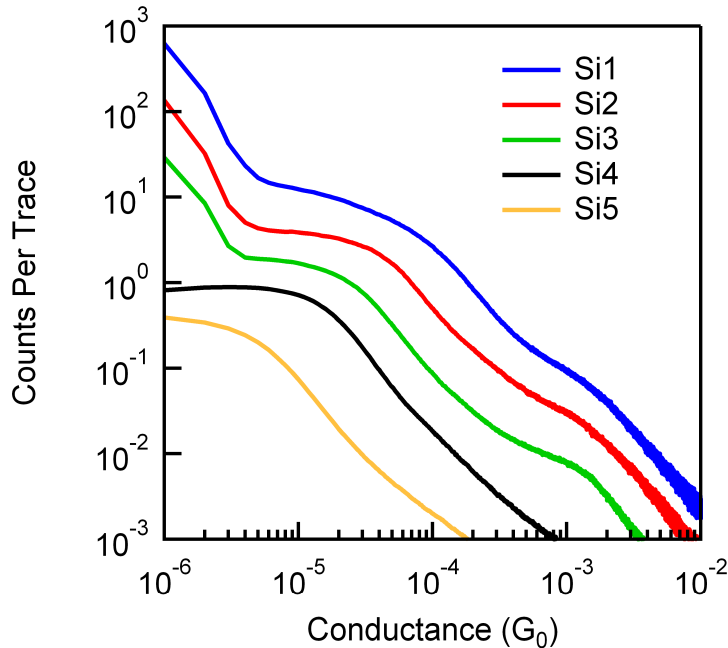


Figure A.5: Linearly binned histograms for **Si1-5** constructed with a bin size of $10^{-6} G_0$. The histograms have been offset vertically for clarity.

conductance peak was observed, consistent with the observation that disruption of the nanowire HOMO through oxidation will reduce conductance.

Additional Conductance Histograms: Given in Figure A.5 are the linearly-binned histograms for **Si1-5**. They were constructed with a bin size of $10^{-6} G_0$ and **Si2-5** are offset vertically downward for clarity. They exhibit broad conductance peaks between 10^{-5} and $10^{-4} G_0$. There is a clear downward shift in conductance as the number of silicon atoms in the molecular backbone increases. The same data sets were used to create the log-binned histograms included in Section 3.3.

The analogous series **C2-4** was also measured in order to compare the two decay constants. The log-binned histograms for **C2-4** are given in Figure A.6. Each histogram includes more than 20000 traces and was prepared using 100 bins per decade of G_0 . The downward red arrows designate the peak locations used in Section 3.3 to calculate the constant β for **C2-4**.

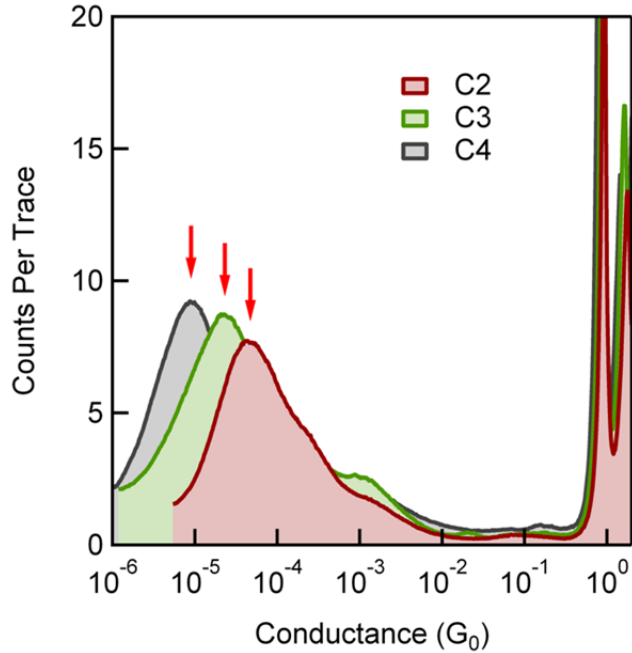


Figure A.6: Logarithmically binned histograms for **C2-4**. The histograms are constructed with a bin size of 100/decade. The peak of each histograms is marked with a downward arrow.

2-Dimensional Histograms Si2-5: The 2D conductance histograms for Si2-4 are given in Figure A.7. The 2D conductance histogram for Si1 is included in Section 3.3. We see here that the molecular junction elongation length increases as the length of the molecule increases.

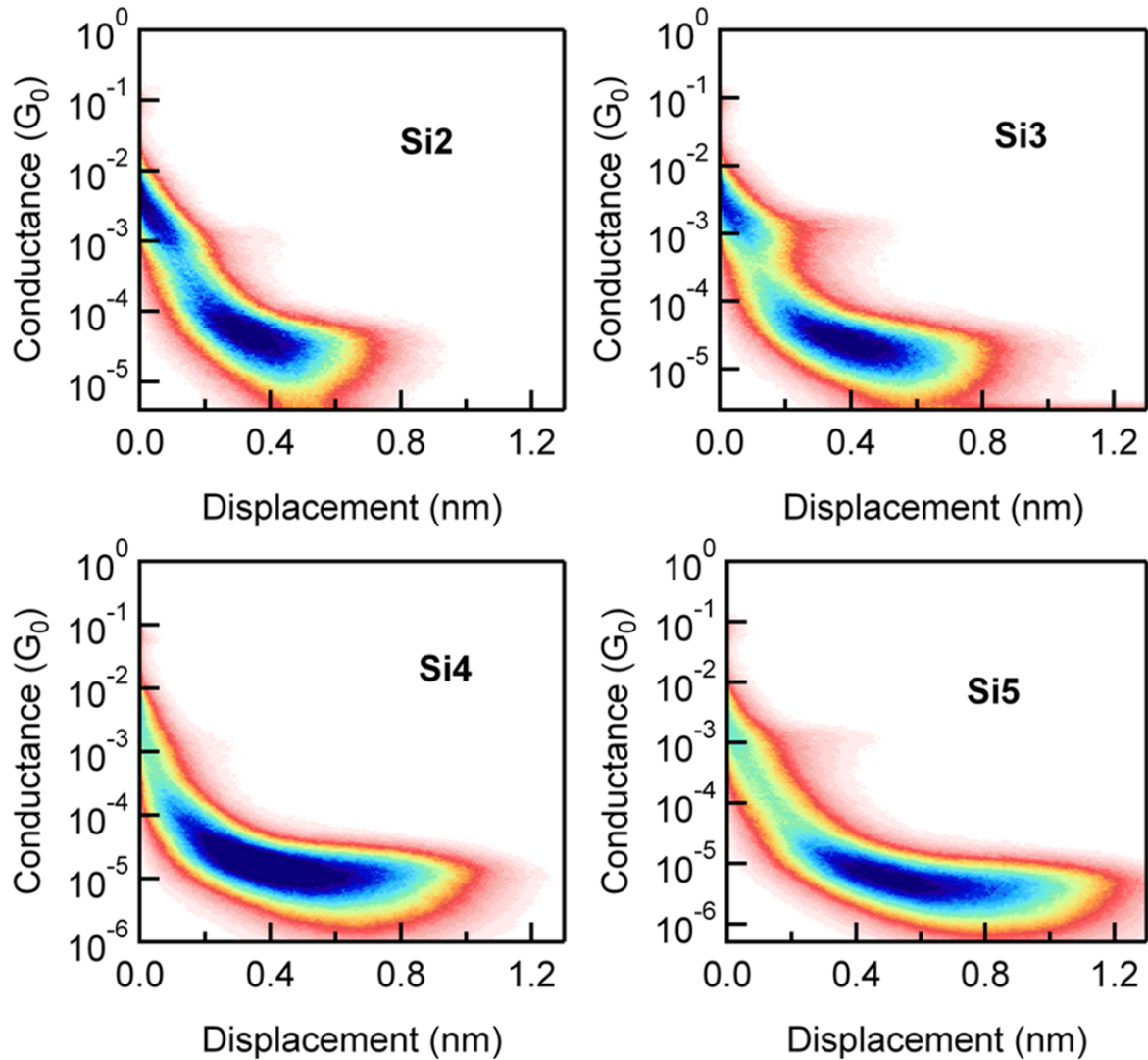


Figure A.7: Two-dimensional conductance histograms for **Si2-5**. The each show a molecule dependent conductance plateau which increases in length with increasing length of the molecule.

A.4 Supplementary Information for Section 4.1

The conductance of each molecule was measured using the STM-based break-junction technique, where an Au tip (Alfa Aesar, 99.998%) cut to be sharp is brought in and out of contact with a substrate of ~100 nm of gold (Alfa Aesar, 99.999%) evaporated onto cleaved mica disks. The substrate is mounted on a piezoelectric positioner (Mad City Labs), so that sub-angstrom resolution in position is achieved. During the entire break junction procedure, a small, constant bias (10 mV) is applied between the tip and the substrate with a 10k Ω series resistance added in the circuit while the current is measured (Keithley 428-Prog). Piezo control and data collection were performed using a National Instruments PXI Chassis System (with PXI-4461, PXI-6289) at 40 kHz and driven and managed with a custom-program using Igor Pro (Wavemetrics, Inc.).

The experimental set-up is kept under ambient conditions. For each experiment, the substrate is cleaned under UV/Ozone for 15 minutes prior to use. For every conductance trace measurement, the STM tip is first brought into hard contact with the substrate to achieve a conductance greater than $\sim 10 G_0$. At this point, the junction electrodes are pulled apart at a speed of 15.8 nm/s for 250 ms (or 3.95 nm). Conductance is measured as a function of tip-sample displacement to generate conductance traces. For each tip/substrate pair, at least one set of 1,000 traces of clean gold breaks is collected to ensure the system is clean. Then, the target molecule is deposited by thermal evaporation (by holding the substrate a few cm above liquid phase molecule in ambient conditions) and an additional 1,000 conductance traces are collected. Every molecular conductance trace is binned linearly into conductance bins, without any data selection, and compiled into a single conductance histogram. The conductance histograms for

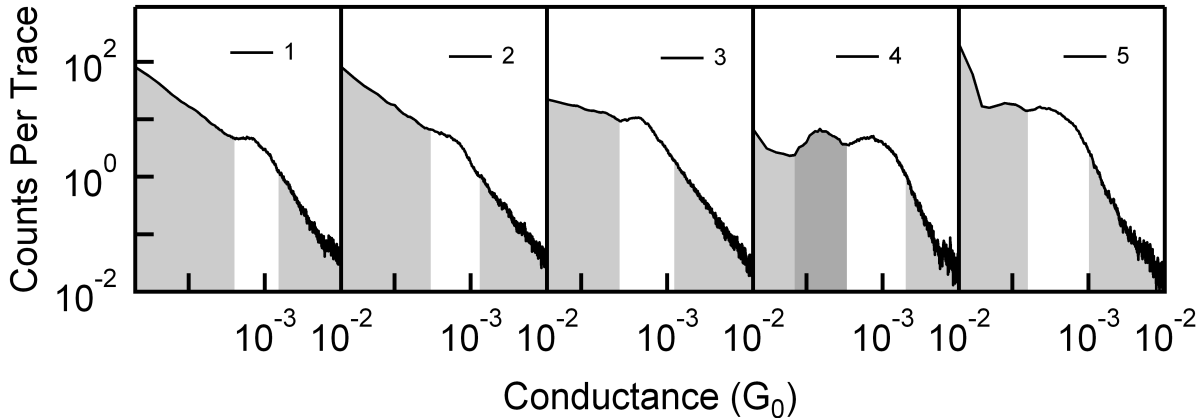


Figure A.8: Conductance histograms of the five molecules under study. The histograms were each formed from 1000 traces without any sort of data selection using a bin size of $10^{-5} G_0$ and are plotted on a log-log scale. The white regions denote the windows used for selection of thermal current measurements. For 4, the dark grey region represents the region of the low-conducting configuration.

each of the five molecules are given in Figure A.8. Every molecule was measured using multiple tip/substrate pairs, on different days to check for consistency and reproducibility.

The molecules measured were as follows:

- (1) 4,4'-diaminostilbene (Astatech, 97%)
- (2) bis-(4-aminophenyl)acetylene (house synthesized)
- (3) 1,5-bis(diphenylphosphino)pentane (Sigma Aldrich, 97%)
- (4) 4,4'-bipyridine (Fluka, 99%)
- (5) 1,2-di(4-pyridyl)ethylene (Fluka, 98%)

For measurement of thermal current, the preceding procedure was modified. A “hold” portion was incorporated into the piezo pull-out ramp, where after the piezo stretched the junction for 2.37 nm, the junction was held constant for 50 ms, and then the stretching continued. During the central two quartiles of the hold (middle 25 ms), the applied bias was dropped to zero, so that all of the current measured here would be due solely to the thermal gradient. The electronics were carefully calibrated after every 1,000 traces to ensure that there were no other

# Kept Traces	(1)	(2)	(3)	(4)	(5)
$\Delta T = 0 \text{ K}$	428	650	528	531	863
$\Delta T = 14 \text{ K}$	474	581	694	475	682
$\Delta T = 27 \text{ K}$	410	898	789	1423	956

Table A.1: Number of traces selected for each molecule at each ΔT .

sources of bias across the junction. The substrate was mounted onto the hot side of a thermoelectric (Peltier) device, while the cold side was kept near room temperature. Additionally, the STM tip was kept near room temperature throughout the measurement. The temperature of the hot substrate and the tip was recorded using a thermocouple. For each molecule, more than 3600 thermal current traces were collected at each of three ΔT 's (0 K, 14 K, 27 K), though not every trace successfully contained a molecular thermal current measurement (i.e. if the gold point contact ruptured “too early” or “too late”). A trace was deemed to successfully measure thermal current through a molecular junction if the average conductance of the first and fourth quartiles of the hold (i.e. when the applied bias is 10 mV) fell within the conductance peak of that respective molecule. The selection regions used are highlighted in white in the conductance histograms in Figure A.8. The number of traces selected for each molecule at each ΔT is given in Table A.1.

Histograms of Measured Average Conductance and Thermal Current

The histograms for (2) bis-(4-aminophenyl)acetylene, (3) 1,5-bis(diphenylphosphino)pentane, (5) 1,2-di(4-pyridyl)ethylene and (4) 4,4'-bipyridine (low conductance geometry), which were not included in Chapter 4, are included here (Figure A.9). In all cases, green denotes $\Delta T = 0 \text{ K}$, blue denote $\Delta T = 14 \text{ K}$, and red denotes $\Delta T = 27 \text{ K}$.

Inclusion of the Low-Conducting State of (4) 4,4'-Bipyridine

Although the sample size is small, we are also able to obtain a distribution of Seebeck coefficients for junctions with 4,4'-bipyridine in the low-conducting state. The conductance

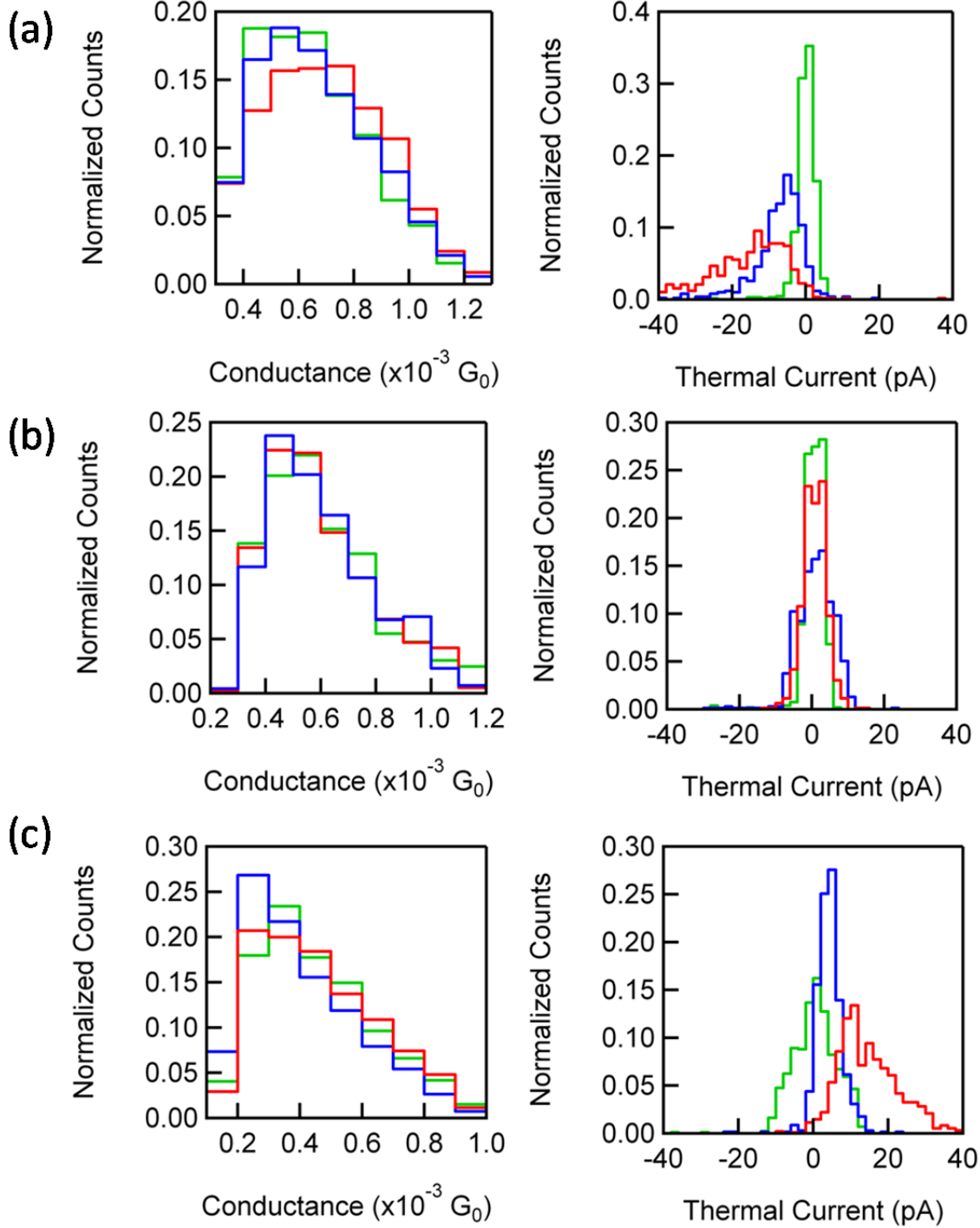


Figure A.9: Histograms for average conductance (left) and thermal current (right) for (a) (2), (b) (3), and (c) (5) for each of the three ΔT 's.

window used is denoted by the dark grey region in the histogram for (4) in Figure A.8. The histograms for thermal current and Seebeck coefficient are given below: We get a molecular

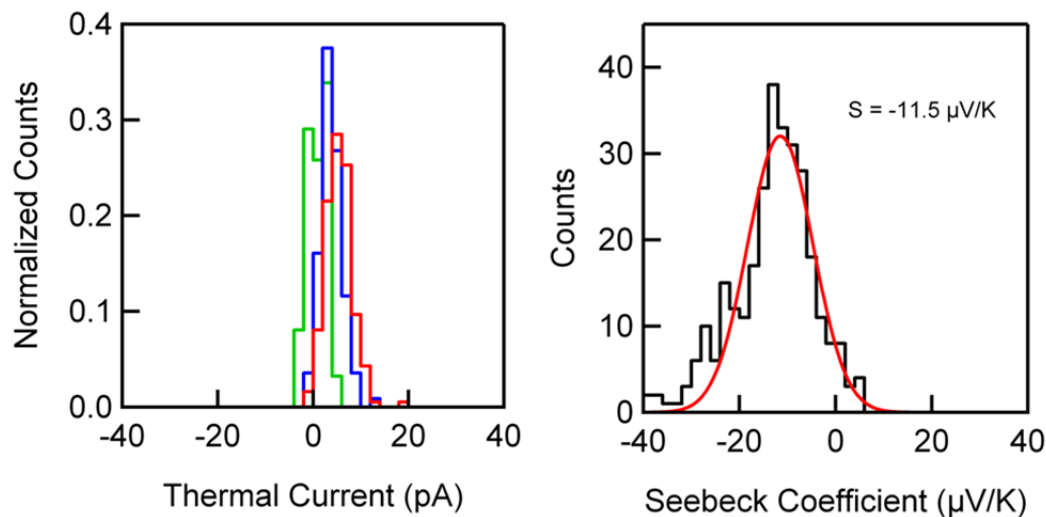


Figure A.10: Histograms of thermal current (left) at each of the three ΔT 's and histogram of molecular Seebeck coefficient (right) for the low-conducting state of 4,4'-bipyridine.

Seebeck coefficient of $-11.5 \mu\text{V}/\text{K}$, which is close to the Seebeck coefficient we get for junctions in the high-conducting state ($-9.5 \mu\text{V}/\text{K}$).

A.5 Supplementary Information for Section 4.2

The following molecules were synthesized according to procedures previously reported in literature[1, 2] and used for the measurements reported here. All structures are shown in Figure A.11:

- 1) 1,4-bis((trimethylstannyl)methyl)benzene (**P1**)
- 2) 4,4'-bis((trimethylstannyl)methyl)-1,1'-biphenyl (**P2**)
- 3) 4,4"-bis((trimethylstannyl)methyl)-1,1':4',1"-terphenyl (**P3**)
- 4) 4,4'''-bis((trimethylstannyl)methyl)-1,1':4',1":4",1'''-quaterphenyl (**P4**)
- 5) 1,6-Bis(trimethylstannyl)hexane (**C6**)
- 6) 1,6-Bis(trimethylstannyl)octane (**C8**)
- 7) 1,10-Bis(trimethylstannyl)decane (**C10**)

The conductance of each molecule was measured using the STM-based break-junction technique[3, 4], where an Au tip (Alfa Aesar, 99.998%) cut to be sharp is brought in and out of contact with a substrate of ~100 nm of gold (Alfa Aesar, 99.999%) evaporated onto cleaved mica disks. The substrate is mounted on a piezoelectric positioner (Mad City Labs), so that sub-angstrom resolution in position is achieved. During the entire break junction procedure, a small, constant bias (10 mV) is applied between the tip and the substrate with a 10k Ω series resistance added in the circuit while the current is measured (Keithley 428-Prog). Piezo control and data collection were performed using a National Instruments PXI Chassis System (with PXI-4461, PXI-6289) at 40 kHz and driven and managed with a custom-program using Igor Pro (Wavemetrics, Inc.). The experimental set-up is kept under ambient conditions.

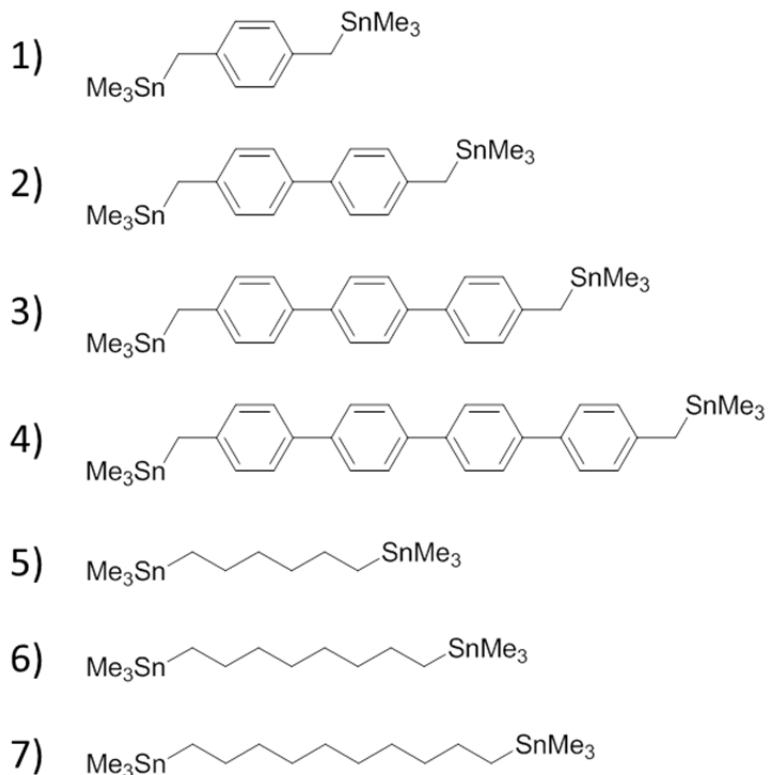


Figure A.11: Structures of the molecules used in the STM-BJ experiment. The trimethyltin end groups cleave off both sides in situ allowing the terminal carbons to covalently bind to the gold electrodes.

For each experiment, the substrate is cleaned under UV/Ozone for 15 minutes prior to use. For every conductance trace measurement, the STM tip is first brought into hard contact

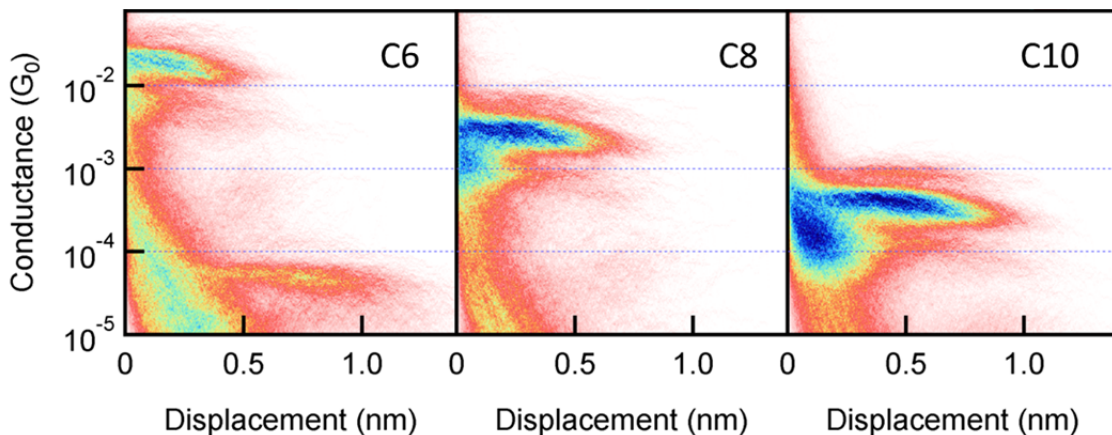


Figure A.12: Two-dimensional conductance histograms of **C6**, **C8**, and **C10**. Thousands of conductance traces are aligned at the rupture of the gold point contact to generate the 2D histograms. The bins have a width of 0.008 nm along the displacement axis and 100/decade along the conductance axis. The feature between 10^{-5} and $10^{-4} G_0$ in the 2D histogram for **C6** is due to the in situ formation of the dimer molecule, **C12**.

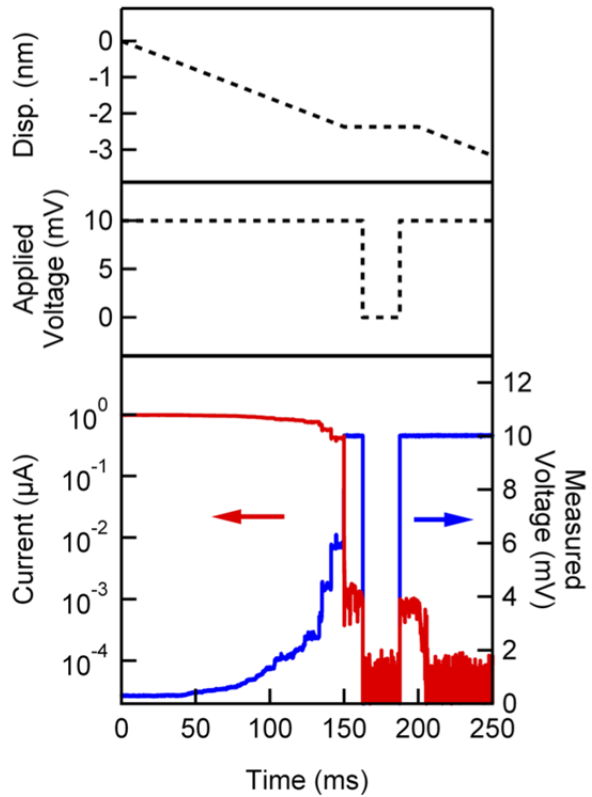


Figure A.13: Top: Piezo ramp used, including a “hold” portion between 150 and 200 ms. Middle: External applied voltage across the leads which drops to zero during the center of the “hold” portion. Bottom: Sample trace for molecular junction. The measured current is shown in red and the voltage measured across the junction is shown in blue.

with the substrate to achieve a conductance greater than $\sim 10 G_0$. At this point, the junction electrodes are pulled apart at a speed of 16 nm/s for 250 ms. Conductance is measured as a function of tip-sample displacement to generate conductance traces. For each tip/substrate pair, at least one set of 1,000 traces of clean gold breaks is collected first to ensure the system is clean. Then, the target molecule is dissolved in acetone ($\sim 10\text{mM}$) and drop cast onto the substrate. The solvent is allowed to evaporate so that a dry layer of analyte remains and an additional 1,000 conductance traces are collected before starting the thermoelectric current measurement.

For measurement of thermoelectric current, the preceding procedure was modified[5]. A “hold” portion was incorporated into the piezo pull-out ramp, where after the piezo stretched the junction for 2.37 nm, the junction was held constant for 50 ms, and then the stretching continued

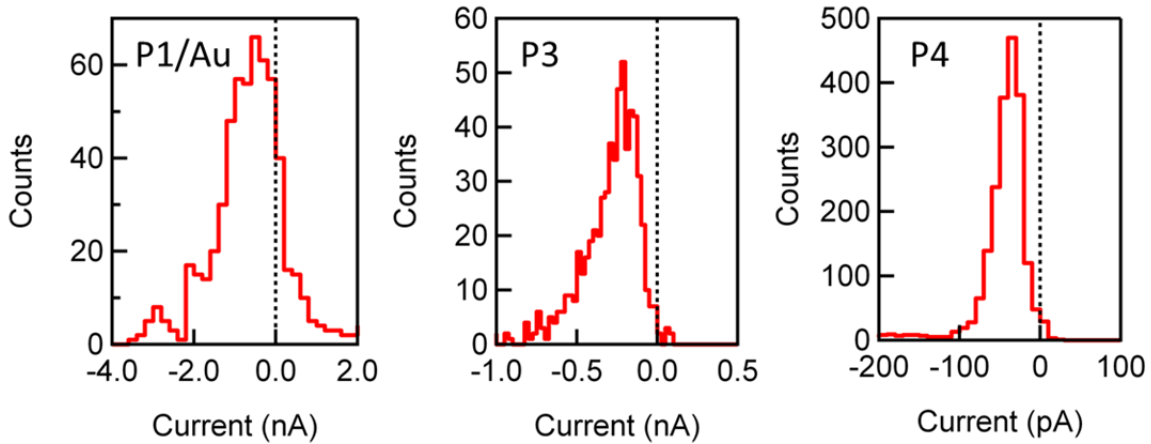


Figure A.14: Average thermoelectric current histograms for **P1/Au** (582 traces), **P3** (629 traces), and **P4** (2,942 traces) for $\Delta T \sim 14$ K. The thermoelectric current histograms for each at $\Delta T = 0$ K (not shown) are narrow and centered at 0 nA and are represented here by dotted lines.

until the junction was broken. During the central two quartiles of the hold (middle 25 ms), the applied bias was dropped to zero, so that all of the current measured would be due solely to the thermal gradient. The electronics was carefully calibrated after every 50 measurements to ensure that there were no other sources of bias across the junction. The substrate was mounted onto the hot side of a thermoelectric (Peltier) device, while the cold side was kept near room temperature. Additionally, the STM tip was kept near room temperature throughout the measurement. The temperature of the hot substrate and the tip was recorded using a thermocouple. For each molecule, more than a few thousand thermal current traces were collected at each ΔT 's (0 K and ~ 14 K), though not every trace included a molecular junction during the “hold” period (i.e. if the gold point contact ruptured “too early” or “too late”). To determine if a molecule was held during this period, the average conductance of the first and fourth quartiles of the hold (i.e. when the applied bias was 10 mV) was analyzed. If it was within the conductance peak of that respective molecule then the trace was selected. A schematic depiction of the procedure along with a sample trace is given in Figure A.13.

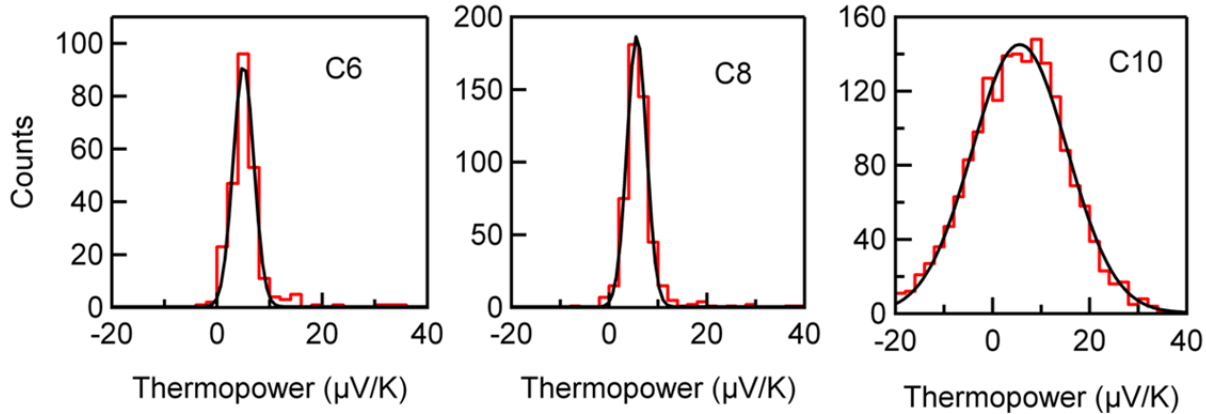


Figure A.15: Histograms of thermopower for **C6** (250 traces), **C8** (506 traces), and **C10** (1,815 traces). The histograms are fit with Gaussians to determine the most frequently measured molecular junction thermopower. The peak thermopower for all three alkanes is 5.0-5.6 $\mu\text{V}/\text{K}$. The width of the **C10** distribution is attributed to signal to noise limitations.

Alternative Models:

Single-Lorentzian Results: We start with the single-Lorentzian model for which the conductance and thermopower are used to determine the energy level alignment relative to the Fermi energy $E_F - E_0$ and the coupling Γ from the equations below[5, 6]:

$$T(E) = \frac{\Gamma^2/4}{(E_0 - E)^2 + \Gamma^2/4}; \quad E_F - E_0 = 2 \frac{S_0}{G} \left(1 - \frac{G}{G_0}\right); \quad \Gamma = \sqrt{\frac{8GS_0(E_F - E_0)}{SG_0}}$$

where $S_0 = \frac{\pi^2 k_B^2 T}{3e} = 7.2576 \text{ eV} \times 1 \mu\text{V}/\text{K}$ and $G_0 = 77.5 \mu\text{S}$. The data in Table 4.2 are used to generate the Lorentzian transmission curves given in Figure A.16.

Modeling Transmission and Fitting Data: For all tight-binding models we first determine the Hamiltonian matrix. The retarded Green's function for the model junction is then $G(E) = [E\mathbb{I} - H]^{-1}$ and the transmission is given by $T(E) = \Gamma^2 |G_{LR}|^2$ where G_{LR} denotes the component of the Green's function matrix that describes the propagation between the left and right electrodes[7]. From this, the conductance and thermopower are calculated numerically. We use this to determine the best fit-coefficients for our data as follows. We pick a set of

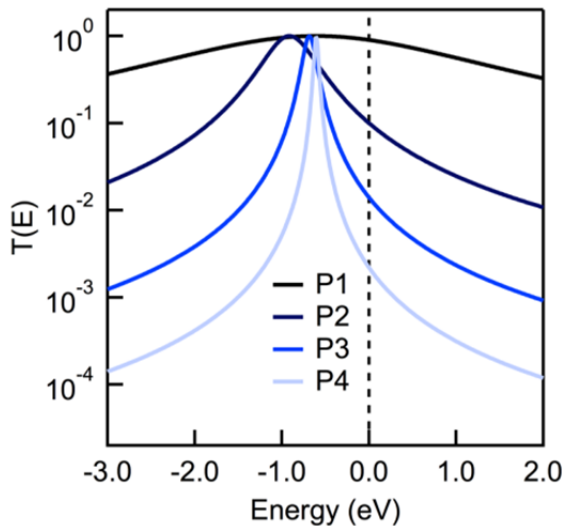


Figure A.16: Lorentzian transmission functions determined individually for each of the oligophenyls measured using the measured values of conductance and thermopower following the equations given above.

coefficients, calculate the transmission functions for all molecules and determine all conductances and thermopowers at E_F . We then systematically vary the coefficients to minimize the total least-squares error given by:

$$\text{Error} = \sum_{n=0}^3 10[\ln(G_{exp,n}) - \ln(G_{model,n})]^2 + [S_{exp,n} - S_{model,n}]^2$$

We use the natural logarithm of the conductance in determining the error so that we don't skew the fit towards higher conducting molecules or just the thermopower.

Model 1: A tight-binding model is constructed to represent the frontier orbital set that controls conductance in which a single energy level is assigned to each individual phenyl ring at an energy E_0 . These are coupled to each other through a hopping parameter δ . The terminal phenyl states also interact with the electrodes through an imaginary energy independent self-energy term $-i\Gamma/2$. The Hamiltonian for this model is similar to that given in the main text, but without the gateway states. We solve for the transmission with the parameters that minimize the error between the model and experiment. As can be seen in Figure A.17, this model gives a

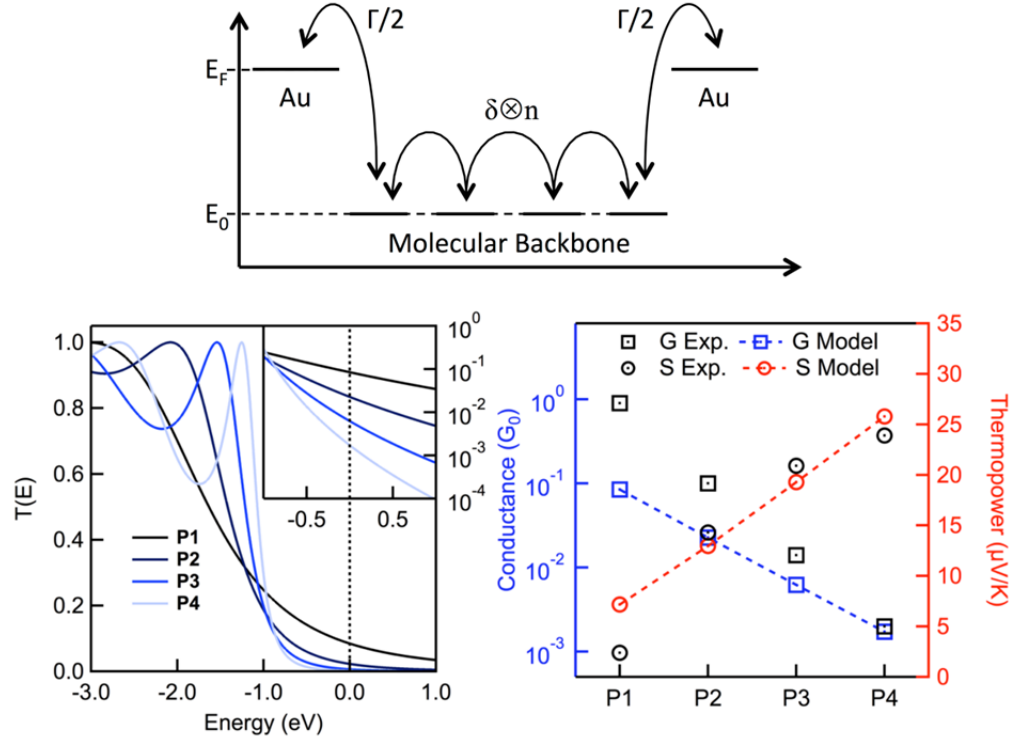


Figure A.17: Transmission functions determined by solving the Hamiltonian that treats each individual phenyl as a separate state, but does not include the gateway state. The parameters used are: $E_0 = -3.87$, $\Gamma = 2.74$, $\delta = -1.6$. A comparison of the model with experiment is also shown.

strictly linear increase in thermopower and underestimates the molecular conductance, and therefore does not fit the experimental data well.

Model 2: This model introduces two gateway states at an energy ε that are tunnel coupled to each other through a length dependent parameter $\delta_n = \delta_0 e^{-\beta n/2}$. They also interact with the electrodes through an imaginary energy independent self-energy term $-i\Gamma/2$. The parameter β describes the long molecule limit of the decay of transmission. The Hamiltonian for this model is given below:

$$H = \begin{pmatrix} \varepsilon - i\Gamma/2 & \delta_n \\ \delta_n & \varepsilon - i\Gamma/2 \end{pmatrix}$$

The transmission function calculated from this Hamiltonian is:

$$T_n(E) = \frac{\Gamma^2 \delta_n^2}{|(E - \varepsilon + i\Gamma/2)^2 - \delta_n^2|^2} \xrightarrow{\text{large } n} \frac{\Gamma^2 \delta_n^2}{((E - \varepsilon)^2 + \Gamma^2/4)^2}$$

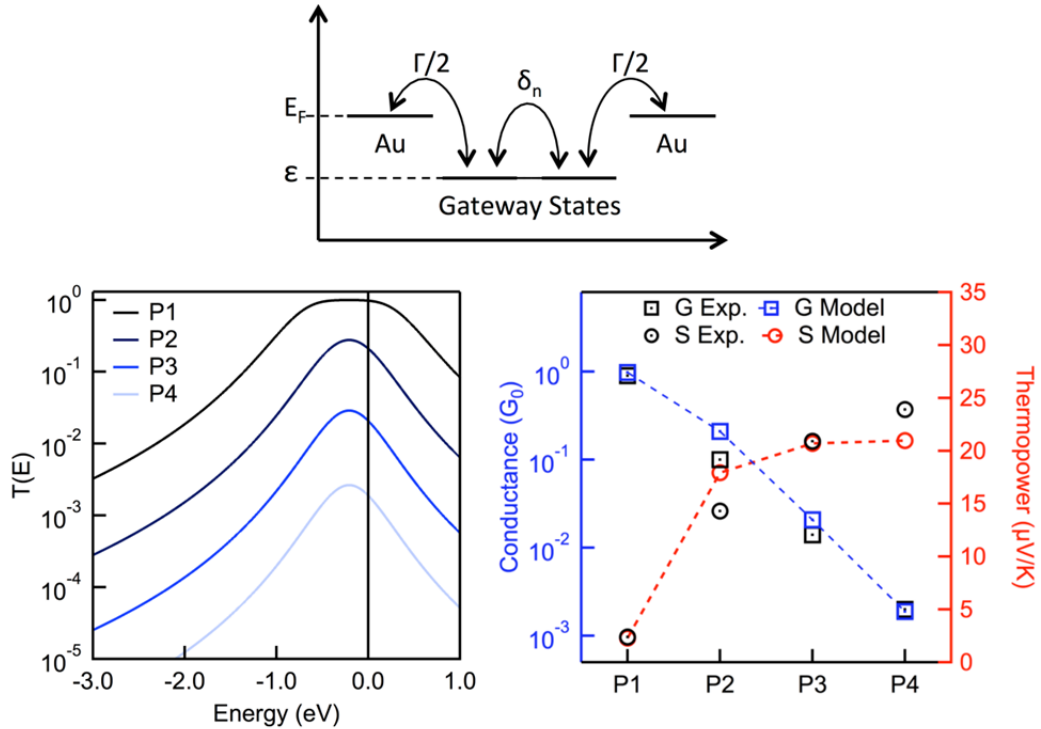


Figure A.18: Transmission functions determined for all oligophenyls following the equations given above using the parameters: $\epsilon = -0.21$, $\Gamma = 0.97$, $\delta_0 = -0.45$ and $\beta = 2.4$. A comparison of the model with experiment is shown in the bottom right panel.

The thermopower can then be approximated as where we β is taken to be energy dependent:

$$S \approx -\frac{\pi^2 k_B^2 T}{3e} \frac{1}{T} \frac{dT}{dE} \approx \frac{-\pi^2 k_B^2 T}{3e} \left(\frac{(\epsilon - E)}{4(\epsilon - E)^2 + \Gamma^2} - n \frac{d\beta}{dE} \right)$$

Results from solving this transmission with the parameters that minimize the error are shown in Figure A.18.

Alkanes DFT Results Compared with Experiments:

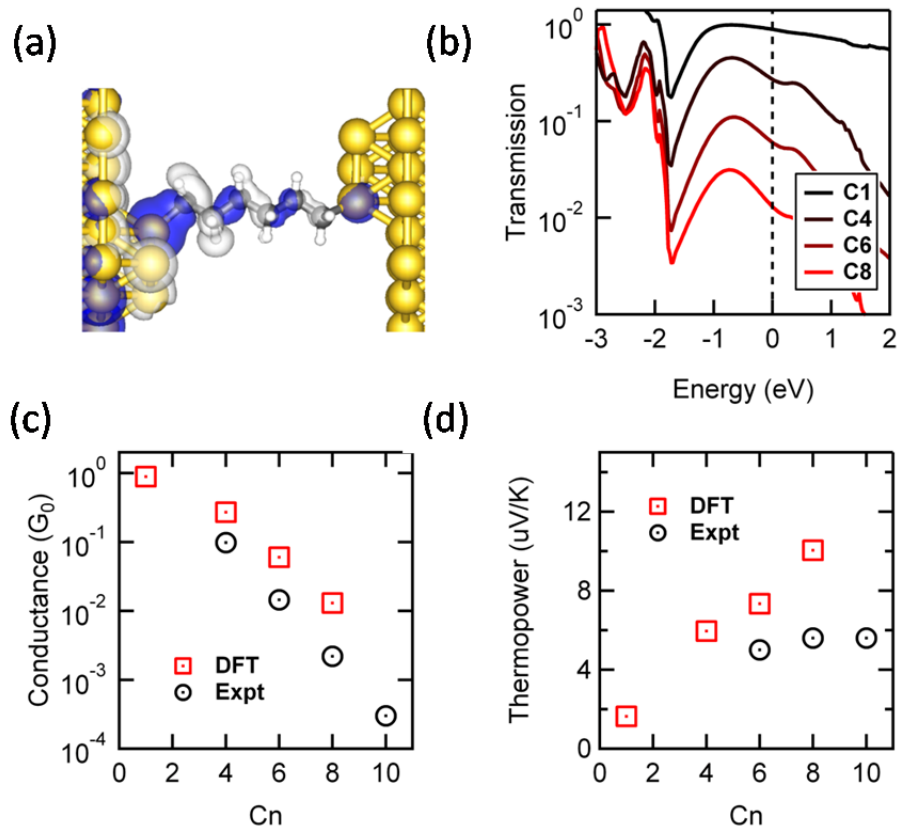


Figure A.19: (a) The optimized geometry of a **C6** junction with an isosurface plot of the scattering state at the Fermi energy. (b) Transmission curves calculated using DFT shown on a log scale for **C1**, **C4**, **C6**, and **C8**. (c) Conductance and (d) thermopower given as a function of molecular length for both experiment and DFT.

A.6 References

1. Chen, W., J.R. Widawsky, H. Vázquez, S.T. Schneebeli, M.S. Hybertsen, R. Breslow, and L. Venkataraman, *Highly Conducting π-Conjugated Molecular Junctions Covalently Bonded to Gold Electrodes*. Journal of the American Chemical Society, 2011. **133**(43): p. 17160-17163.
2. Cheng, Z.L., R. Skouta, H. Vazquez, J.R. Widawsky, S. Schneebeli, W. Chen, M.S. Hybertsen, R. Breslow, and L. Venkataraman, *In situ formation of highly conducting covalent Au-C contacts for single-molecule junctions*. Nature Nanotechnology, 2011. **6**(6): p. 353-357.
3. Xu, B.Q. and N.J. Tao, *Measurement of single-molecule resistance by repeated formation of molecular junctions*. Science, 2003. **301**(5637): p. 1221-1223.
4. Venkataraman, L., J.E. Klare, C. Nuckolls, M.S. Hybertsen, and M.L. Steigerwald, *Dependence of single-molecule junction conductance on molecular conformation*. Nature, 2006. **442**(7105): p. 904-907.
5. Widawsky, J.R., P. Darancet, J.B. Neaton, and L. Venkataraman, *Simultaneous Determination of Conductance and Thermopower of Single Molecule Junctions*. Nano Letters, 2012. **12**(1): p. 354-358.
6. Malen, J.A., P. Doak, K. Baheti, T.D. Tilley, R.A. Segalman, and A. Majumdar, *Identifying the Length Dependence of Orbital Alignment and Contact Coupling in Molecular Heterojunctions*. Nano Letters, 2009. **9**(3): p. 1164-1169.
7. Datta, S., *Electronic Transport in Mesoscopic Systems*. 1995: Cambridge University Press.